

UCSF

UC San Francisco Electronic Theses and Dissertations

Title

Functional genomic interrogation of inflammatory astrocyte reactivity

Permalink

<https://escholarship.org/uc/item/928256mq>

Author

Leng, Kun

Publication Date

2021

Peer reviewed|Thesis/dissertation

Functional genomic interrogation of inflammatory astrocyte reactivity

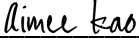
by
Kun Leng

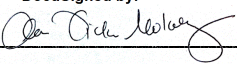
DISSERTATION
Submitted in partial satisfaction of the requirements for degree of
DOCTOR OF PHILOSOPHY

in
Biomedical Sciences

in the
GRADUATE DIVISION
of the
UNIVERSITY OF CALIFORNIA, SAN FRANCISCO

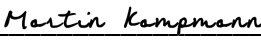
Approved:

DocuSigned by:

745CF57D40DB494... Aimee Kao
Chair

DocuSigned by:

DocuSigned by: 3A... Anna Molofsky

DocuSigned by:

DocuSigned by: 3A... Michael Oldham

DocuSigned by:

03BA4012CC044AF... Martin Kampmann

Committee Members

Copyright 2021

By

Kun Leng

Dedicated to my parents, Dr. Gexin Wang and Han Leng

ACKNOWLEDGEMENTS

First, I thank my PhD advisor, Dr. Martin Kampmann, for his unwavering support, tireless dedication to his lab, and steadfast commitment to mentorship. Martin gave me the freedom to pursue my ideas, guided me through my failures, pushed me beyond my comfort zone, and supported me in every which way. I could not have been more fortunate to have Martin as my mentor, and I cannot thank him enough.

In addition to Martin, I also thank all the people who have been a part of the Kampmann lab over the years, for making the lab such a great place to be in. The lab is like a family to me, and I treasure all the moments I have been able spend with my labmates.

I thank my thesis committee, Dr. Anna Molofsky, Dr. Aimee Kao, and Dr. Michael Oldham, for their guidance and support. Every committee meeting felt like it flew by, and there was always so much more to talk about.

I thank my undergraduate advisor, Dr. John Hunt, and my postdoc mentor during that time, Dr. Jinrang Kim, for setting me on the right path and nurturing me as a budding scientist. I also thank Dr. Amina Woods, my advisor at the National Institute on Drug Abuse, for giving me a chance and taking me on as a summer student when I had nothing except curiosity and excitement.

I thank my MSTP classmates, Paul and Ian, for being the best roommates and friends, and also my entire MSTP class, for their company and friendship during our journey.

I thank my wife, Jenna, for supporting me every step of the way and pushing me to do my best.

Finally, I thank my parents, who overcame countless obstacles to start a new life in the United States. Their sacrifices drive me to cherish every opportunity. Their example reminds me that no obstacle is too great.

CONTRIBUTIONS TO PRESENTED WORK

All work in this dissertation was done under the direct supervision and guidance of Dr. Martin Kampmann. Funding for this research was acquired by Dr. Kampmann and supported by the NIH F30 fellowship (AG066418) except where stated in the acknowledgement section of each chapter. Additional contributions are described below.

Chapter 2 is reproduced in its entirety from the following publication:

Leng, K.*, Li, E.*, Eser, R., Piergies, A., Sit, R., Tan, M., Neff N., Li S.H., Rodriguez R.D., Suemoto C.K., Leite R.E.P., Ehrenberg A.J., Pasqualucci C.A., Seeley W.W., Spina S., Heinsen H., Grinberg L.T. & Kampmann, M. (2021). Molecular characterization of selectively vulnerable neurons in Alzheimer's disease. *Nature Neuroscience*, 24(2), 276-287. <https://doi.org/10.1038/s41593-020-00764-7>.

*Co-first authorship

K.L., E.L., L.T.G. and M.K. conceptualized and led the overall project. K.L., L.T.G. and M.K. wrote the manuscript, with input from all co-authors. K.L. analyzed snRNA-Seq data and visualized results. E.L. generated snRNA-Seq data, with support from R.S., M.T., and N.N. R.D.R., C.K.S., R.E.P.L., A.E., C.A.P. W.W.S., and S.S. contributed to neuropathological data generation and analysis, R.E., A.P. and H.H. contributed to neuropathological data analysis, and S.H.L. contributed to neuropathological method development.

Chapter 3 is reproduced in its entirety from the following preprint:

Leng, K., Rooney, B., Kim, H., Xia, W., Koontz, M., Krawczyk, M., Zhang Y., Ullian E.M., Fancy S.P.J., Schrag M.S., Lippman E.S. & Kampmann, M. (2021). CRISPRi screens in human astrocytes elucidate regulators of distinct inflammatory reactive states. *bioRxiv*. <https://doi.org/10.1101/2021.08.23.457400>

KL and M. Kampmann. conceptualized and led the overall project, and wrote the manuscript with input from all co-authors. KL performed the majority of experiments with support from BR and performed all data analysis. HK performed immunostaining of AD tissues provided by MSS and co-culture experiments with guidance from ESL, and WX performed immunostaining of HIE

tissue with guidance from SF. M. Koontz generated hiPSC-derived astrocytes using the methods of Krencik *et al.* and Li *et al.* with guidance from EMU. M. Krawczyk and YZ supplied unpublished human astrocyte RNA-seq data for master regulator analysis.

Chapter 4 is reproduced in its entirety from the following preprint:

Rooney B. *, **Leng K.** *, McCarthy F., Rose I.L.V., Herrington K.A., Bax S., Chin M.Y., Fathi S., Leonetti M., Kao A.W., Elias J.E. & Kampmann M. mTOR controls neurotoxic lysosome exocytosis in inflammatory reactive astrocytes. *bioRxiv*. <https://doi.org/10.1101/2021.09.11.459904>.

*Co-first authorship

B.R., K.L., and M.K. conceptualized and led the overall project, and wrote the manuscript with input from all co-authors. B.R. performed the majority of experiments and data analysis. K.L. developed the iAstrocyte platform, performed preliminary studies, and conducted the RNA-seq experiments. In consultation with J.E., F.M. aided with sample preparation for whole-cell and lysosome-specific proteomics experiments, and performed mass spectrometry and preliminary computational analysis. I.V.L.R. performed sample prep for the cell-surface LAMP1 CRISPRi screens. K.A.H. guided TIRF experiments. M.L. and S.B. aided with design and sample preparation for whole-cell and lysosome-specific proteomics experiments, respectively. M.Y.C. and A.W.K. provided FIRE-pHly reagents and guidance on lysosome pH experiments. S.F. conducted LAMP2 immunofluorescence experiments and data analysis.

ABSTRACT

Functional genomic interrogation of inflammatory astrocyte reactivity

Kun Leng

Astrocytes perform critical homeostatic functions in the central nervous system (CNS). In CNS injury or disease, astrocytes respond to pathophysiological perturbations by becoming “reactive”, which is defined as the adoption of context-specific cell states and associated alterations in morphology and function. Frequently, inflammatory processes play an important role in the pathophysiology of CNS injuries and diseases. As an immunocompetent CNS cell type, astrocytes actively participate in inflammatory signaling cascades involving interaction with both microglia as well as infiltrating peripheral immune cells. Proinflammatory cytokines, such as IL-1 α , TNF, and C1q, induce inflammatory reactive astrocytes that lose homeostatic functions while concurrently releasing factors that are potentially harmful in specific contexts. Given that inflammatory astrocyte reactivity has been implicated in numerous neurodegenerative and neuroinflammatory diseases, in addition to being associated with normal aging, it is an attractive target for therapeutic development. However, the cellular pathways that control inflammatory astrocyte reactivity are still not fully understood.

In Chapter 1 of this dissertation, we broadly introduce astrocyte reactivity as a concept and the existing literature on inflammatory astrocyte reactivity.

In Chapter 2, we set out to characterize astrocyte reactivity in the context of Alzheimer’s disease (AD) using single-nucleus RNA-sequencing of post-mortem AD brain tissue. In addition to discovering that reactive astrocytes in AD downregulated homeostatic pathways, we also found that a specific subpopulation of excitatory neurons were selective vulnerable in AD, which we were able to validate using immunostaining in an independent cohort of cases and controls.

In Chapter 3, we developed a scalable method to generate hiPSC-derived astrocytes that allowed us to harness the power of pooled CRISPRi screening to systematically identify

cellular pathways controlling inflammatory astrocyte reactivity. Following up on the top hits from CRISPRi screens with single-cell transcriptomics, we found that autocrine-paracrine IL-6 and interferon signaling drove two distinct inflammatory reactive states that were promoted by and inhibited by STAT3, respectively. Furthermore, we found that the inflammatory reactive states we identified corresponded to those observed in other experimental contexts, both *in vitro* and *in vivo*. Lastly, we also performed immunostaining supporting the existence of these inflammatory reactive states in human brains in the context of Alzheimer's disease and hypoxic-ischemic encephalopathy.

In Chapter 4, we focused on how autophagic pathways are rewired in inflammatory reactive astrocytes and how this contributes to the neurotoxic activity of inflammatory reactive astrocytes. We found that lysosomes are remodeled and alkalinized in inflammatory reactive astrocytes, and that lysosome exocytosis drives astrocyte-mediated neurotoxicity. Through CRISPRi screening, we uncovered mTOR as a regulator of neurotoxic lysosome exocytosis. These results pinpoint lysosome remodeling and exocytosis in inflammatory reactive astrocytes as a potential therapeutic target.

We believe these studies contribute to our understanding of inflammatory astrocyte reactivity and may inform the development of therapeutics that modulate specific aspects of astrocyte reactivity for the treatment of neurodegenerative and neuroinflammatory diseases.

TABLE OF CONTENTS

CHAPTER 1	1
Introduction	1
REFERENCES	4
CHAPTER 2	6
Molecular characterization of selectively vulnerable neurons in Alzheimer’s disease	6
ABSTRACT	7
INTRODUCTION	7
RESULTS	8
DISCUSSION	18
DATA AVAILABILITY	22
CODE AVAILABILITY	22
ACCESSION CODES	22
ACKNOWLEDGEMENTS	22
AUTHOR CONTRIBUTIONS	23
COMPETING INTERESTS	23
ETHICS DECLARATIONS	23
METHODS	51
REFERENCES	63
CHAPTER 3	73
CRISPRi screens in human astrocytes elucidate regulators of distinct inflammatory reactive states	73
ABSTRACT	74
INTRODUCTION	74
RESULTS	76
DISCUSSION	89

ACKNOWLEDGEMENTS	90
AUTHOR CONTRIBUTIONS	91
COMPETING INTERESTS STATEMENT	91
DATA AVAILABILITY STATEMENT	92
CODE AVAILABILITY STATEMENT	92
METHODS	113
REFERENCES	137
CHAPTER 4	144
mTOR controls neurotoxic lysosome exocytosis in inflammatory reactive astrocytes	144
ABSTRACT	145
MAIN	145
ACKNOWLEDGEMENTS	152
AUTHOR CONTRIBUTIONS	152
COMPETING INTERESTS STATEMENT	153
DATA AVAILABILITY STATEMENT	153
CODE AVAILABILITY STATEMENT	153
METHODS	163
REFERENCES	177

LIST OF FIGURES

CHAPTER 2	6
Molecular characterization of selectively vulnerable neurons in Alzheimer's disease	6
Fig. 2.1 AD progression differentially affects the cell-type composition of the EC and SFG	24
Fig. 2.2 RORB-expressing excitatory neuron subpopulations in the EC are selectively vulnerable	26
Fig. 2.3 Immunofluorescence of the EC validates selective vulnerability of RORB-expressing excitatory neurons	29
Fig. 2.4 Inhibitory neuron subpopulations do not consistently show differences in resilience or vulnerability to AD progression	30
Fig. 2.5 GFAP ^{high} astrocytes show signs of dysfunction in glutamate homeostasis and synaptic support	32
Fig. S2.1 Data quality and initial clustering without cross-sample alignment	35
Fig. S2.2 Expression of selected EC excitatory neuron subpopulation markers and pathway enrichment analysis of differentially expressed genes in selectively vulnerable EC excitatory neuron subpopulations	37
Fig. S2.3 Differential expression analysis across Braak stages for EC excitatory neuron subpopulations	38
Fig. S2.4 Alignment of EC and SFG maps homologous excitatory neuron subpopulations	40
Fig. S2.5 Cross-sample alignment of excitatory neurons from Mathys <i>et al.</i> recapitulates selective vulnerability in a RORB-expressing subpopulation	41
Fig. S2.6 Delineation of the EC for each case used in immunofluorescence validation	43
Fig. S2.7 Inhibitory neurons from Mathys <i>et al.</i> also do not show differences in resilience or vulnerability to AD	44
Fig. S2.8 Subclustering of microglia does not sufficiently resolve disease associated microglia signature	46
Fig. S2.9 Subclustering of oligodendrocytes identifies subpopulations with higher expression of AD-associated oligodendrocyte markers from Mathys <i>et al.</i>	47

Fig. S2.10 Astrocyte subpopulations with high GFAP expression from Mathys et al. are highly similar to those from the EC and SFG	49
CHAPTER 3	73
CRISPRi screens in human astrocytes elucidate regulators of distinct inflammatory reactive states	73
Fig. 3.1 iPSC-derived astrocytes (iAstrocytes) perform canonical astrocyte functions and recapitulate key aspects of inflammatory reactivity upon treatment with IL-1 α +TNF+C1q	94
Fig. 3.2 CRISPR interference (CRISPRi) platform in iAstrocytes	95
Fig. 3.3 CRISPRi screening and master regulator analysis uncover regulators of inflammatory reactivity	97
Fig. 3.4 CROP-seq of iAstrocytes reveals two distinct inflammatory reactive states dependent on the canonical NF-kB pathway	99
Fig. 3.5 IL-6 and interferons act in an autocrine-paracrine manner to drive distinct inflammatory reactive states	101
Fig. 3.6 Integration of iAstrocyte single-cell data with published single-cell datasets shows conservation of distinct inflammatory reactive states across species in diverse disease contexts	103
Fig. S3.2 iAstrocytes respond to IL-1 α +TNF+C1q in a highly similar manner as iPSC-derived astrocytes generated using different protocols and primary mouse astrocytes	106
Fig. S3.3 Validation of hits from CRISPRi screens and master regulator analysis	107
Fig. S3.4 Additional analyses of CROP-seq data	109
Fig. S3.5 Enrichment analysis of CROP-seq knockdown-associated gene modules	110
Fig. S3.6 Overlap analysis of IRAS1 and IRAS2 markers with external datasets	111
CHAPTER 4	144
mTOR controls neurotoxic lysosome exocytosis in inflammatory reactive astrocytes	144
Fig. 4.1 Lysosomes are remodelled in inflammatory reactive astrocytes	154

Fig. 4.2 Lysosome exocytosis controls neurotoxicity of inflammatory reactive astrocytes	156
Fig. 4.3 CRISPRi screens uncover mTOR as a regulator of lysosome exocytosis and inflammatory reactive astrocyte-mediated neurotoxicity	159
Fig. S4.1 Further characterization of lysosome remodeling in inflammatory reactive astrocytes	160
Fig. S4.2 Further characterization of the lysosome alkalization-exocytosis-neurotoxicity axis in iAstrocytes	161
Fig. S4.3 LysoTracker and LAMP1 CRISPRi screening results	162

LIST OF TABLES

CHAPTER 2	6
Molecular characterization of selectively vulnerable neurons in Alzheimer's disease	6
Table 2.1 Description of post-mortem cohort.	33

CHAPTER 1

Introduction

Astrocytes perform critical homeostatic functions in the central nervous system (CNS), such as providing trophic support for neurons, regulating the formation and function of synapses, and maintaining the blood–brain barrier¹. In CNS injury or disease, astrocytes respond to pathophysiological perturbations by becoming “reactive”, which is defined as the adoption of context-specific cell states and associated alterations in morphology and function²⁻⁴. This definition improves upon the historical definition of reactive astrocytes based upon GFAP upregulation and morphological hypertrophy, and reflects our current understanding of astrocyte reactivity as not a monolithic process or cellular state, but as an umbrella term covering the complex and heterogeneous responses of astrocytes to deleterious perturbations of CNS homeostasis².

Given the above paradigm of astrocyte reactivity, it follows that different kinds of insults to the CNS result in different kinds of reactive astrocytes. For example, astrocytes exhibit divergent transcriptomic profiles in the context peripheral LPS-induced neuroinflammation vs. ischemic injury induced by middle cerebral artery occlusion⁵. However, the same insult can also result in different reactive states dependent on proximity to the insult or anatomical location. For example, mechanical injuries from stab wound models induce “scar-forming” reactive astrocytes that proliferate, migrate, and surround the point of injury, disrupting the normal “tiling” of astrocyte domains⁶. Further away from the point of injury can be found reactive astrocytes with morphological hypertrophy and GFAP upregulation, but no proliferation or disruption of astrocyte domain tiling³. As another example, a recent study leveraging single-cell RNA-sequencing profiled astrocytes in the context of neuroinflammation induced by peripheral LPS injection and uncovered a multitude of reactive states with different cytokine response signatures⁷. Interestingly, one particular reactive state defined by an interferon-response

signature was shown to correspond to astrocytes localized near vasculature or brain ventricles, likely reflecting interaction with peripheral sources of interferon.

Having introduced the general concept of astrocyte reactivity as the adoption of context-specific cell states and associated alterations in morphology and function, we will now focus on reactive astrocytes induced by inflammatory insults. Frequently, inflammatory processes play an important, if not central, role in the pathophysiology of CNS injuries, as seen in stroke⁸ and trauma⁹, and diseases such as multiple sclerosis¹⁰ and Alzheimer's disease¹¹. As an immunocompetent CNS cell type, astrocytes actively participate in inflammatory signaling cascades and interact with both microglia, the CNS resident immune cells, as well as infiltrating immune cells from the periphery^{12,13}. Proinflammatory cytokines, such as IL-1 α , TNF, and C1q, induce reactive astrocytes that lose homeostatic functions while concurrently releasing factors that are potentially harmful in specific contexts¹⁴⁻¹⁶. From here on, we will refer to this form of astrocyte reactivity as "inflammatory reactivity".

Given that inflammatory astrocyte reactivity has been implicated in numerous neurodegenerative and neuroinflammatory diseases^{14,17}, in addition to being associated with normal aging¹⁸, it is an attractive target for therapeutic development. However, the cellular pathways that control inflammatory astrocyte reactivity are still not fully understood, partly due to limitations in experimental scalability. On the one hand, animal models have provided key insights into genes required for astrocyte reactivity^{15,19,20}, but the throughput to test genetic perturbations *in vivo* is extremely limited. On the other hand, *in vitro* astrocyte culture is a powerful alternative, but the scalability of experiments is still limited by the necessity to isolate primary astrocytes or the long duration of the differentiation process (up to 6 months) required to generate mature, non-reactive human iPSC (hiPSC)-derived astrocytes²¹. Lastly, even though "omics" assays such as RNA-seq have been used extensively to identify cellular pathways altered in inflammatory reactive astrocytes^{5,15}, these assays by themselves can only provide correlative information and cannot uncover causal pathways controlling inflammatory reactivity.

Thus, in the following chapters, we address the above issues by first profiling astrocytes in the context of Alzheimer's disease to further characterize how reactive astrocytes behave in the context of neurodegeneration in Chapter 2. Next, in Chapter 3, we develop a scalable iPSC-derived astrocyte platform and leverage CRISPR-based functional genomics to identify cellular pathways controlling inflammatory astrocyte reactivity. And finally, in Chapter 4, we focus on how autophagic pathways are rewired in inflammatory reactive astrocytes and how this contributes to their neurotoxic capacity.

REFERENCES

1. Sofroniew, M. V. & Vinters, H. V. Astrocytes: biology and pathology. *Acta Neuropathol* **119**, 7-35, doi:10.1007/s00401-009-0619-8 (2010).
2. Escartin, C. *et al.* Reactive astrocyte nomenclature, definitions, and future directions. *Nat Neurosci* **24**, 312-325, doi:10.1038/s41593-020-00783-4 (2021).
3. Sofroniew, M. V. Astrocyte Reactivity: Subtypes, States, and Functions in CNS Innate Immunity. *Trends in Immunology* **41**, 758-770, doi:10.1016/j.it.2020.07.004 (2020).
4. Liddelow, S. A. a. B. B. A. Reactive Astrocytes: Production, Function, and Therapeutic Potential. **46**, 957--967, doi:10.1016/j.immuni.2017.06.006 (2017).
5. Zamanian, J. L. *et al.* Genomic analysis of reactive astrogliosis. *J Neurosci* **32**, 6391-6410, doi:10.1523/JNEUROSCI.6221-11.2012 (2012).
6. Anderson, M. A. *et al.* Astrocyte scar formation aids central nervous system axon regeneration. *Nature* **532**, 195-200, doi:10.1038/nature17623 (2016).
7. Hasel, P., Rose, I. V. L., Sadick, J. S., Kim, R. D. & Liddelow, S. A. Neuroinflammatory astrocyte subtypes in the mouse brain. *Nat Neurosci* **24**, 1475-1487, doi:10.1038/s41593-021-00905-6 (2021).
8. Wang, Q., Tang, X. N. & Yenari, M. A. The inflammatory response in stroke. *J Neuroimmunol* **184**, 53-68, doi:10.1016/j.jneuroim.2006.11.014 (2007).
9. Hausmann, O. N. Post-traumatic inflammation following spinal cord injury. *Spinal Cord* **41**, 369-378, doi:10.1038/sj.sc.3101483 (2003).
10. Ponath, G., Park, C. & Pitt, D. The Role of Astrocytes in Multiple Sclerosis. *Front Immunol* **9**, 217, doi:10.3389/fimmu.2018.00217 (2018).
11. Heneka, M. T. *et al.* Neuroinflammation in Alzheimer's disease. *Lancet Neurol* **14**, 388-405, doi:10.1016/S1474-4422(15)70016-5 (2015).
12. Xie, L. & Yang, S. H. Interaction of astrocytes and T cells in physiological and pathological conditions. *Brain Res* **1623**, 63-73, doi:10.1016/j.brainres.2015.03.026 (2015).

13. Han, R. T., Kim, R. D., Molofsky, A. V. & Liddelow, S. A. Astrocyte-immune cell interactions in physiology and pathology. *Immunity* **54**, 211-224, doi:10.1016/j.immuni.2021.01.013 (2021).
14. Liddelow, S. A. *et al.* Neurotoxic reactive astrocytes are induced by activated microglia. *Nature* **541**, 481-487, doi:10.1038/nature21029 (2017).
15. Guttenplan, K. A. *et al.* Knockout of reactive astrocyte activating factors slows disease progression in an ALS mouse model. *Nat Commun* **11**, 3753, doi:10.1038/s41467-020-17514-9 (2020).
16. Guttenplan, K. A. *et al.* Neurotoxic Reactive Astrocytes Drive Neuronal Death after Retinal Injury. *Cell Rep* **31**, 107776, doi:10.1016/j.celrep.2020.107776 (2020).
17. Yun, S. P. *et al.* Block of A1 astrocyte conversion by microglia is neuroprotective in models of Parkinson's disease. *Nat Med* **24**, 931-938, doi:10.1038/s41591-018-0051-5 (2018).
18. Clarke, L. E. *et al.* Normal aging induces A1-like astrocyte reactivity. *Proc Natl Acad Sci U S A* **115**, E1896-E1905, doi:10.1073/pnas.1800165115 (2018).
19. Herrmann, J. E. *et al.* STAT3 is a critical regulator of astrogliosis and scar formation after spinal cord injury. *J Neurosci* **28**, 7231-7243, doi:10.1523/JNEUROSCI.1709-08.2008 (2008).
20. Liu, Z. *et al.* Beneficial effects of gfap/vimentin reactive astrocytes for axonal remodeling and motor behavioral recovery in mice after stroke. *Glia* **62**, 2022-2033, doi:10.1002/glia.22723 (2014).
21. Krencik, R. & Zhang, S. C. Directed differentiation of functional astroglial subtypes from human pluripotent stem cells. *Nat Protoc* **6**, 1710-1717, doi:10.1038/nprot.2011.405 (2011).

CHAPTER 2

Molecular characterization of selectively vulnerable neurons in Alzheimer's disease

This chapter was published as:

Leng, K.*, Li, E.*, Eser, R., Piergies, A., Sit, R., Tan, M., Neff N., Li S.H., Rodriguez R.D., Suemoto C.K., Leite R.E.P., Ehrenberg A.J., Pasqualucci C.A., Seeley W.W., Spina S., Heinsen H., Grinberg L.T. & Kampmann, M. (2021). Molecular characterization of selectively vulnerable neurons in Alzheimer's disease. *Nature Neuroscience*, 24(2), 276-287. <https://doi.org/10.1038/s41593-020-00764-7>.

*Co-first authorship

ABSTRACT

Alzheimer's disease (AD) is characterized by the selective vulnerability of specific neuronal populations, the molecular signatures of which are largely unknown. To identify and characterize selectively vulnerable neuronal populations, we used single-nucleus RNA sequencing to profile the caudal entorhinal cortex and the superior frontal gyrus – brain regions where neurofibrillary inclusions and neuronal loss occur early and late in AD, respectively – from postmortem brains spanning the progression of AD-type tau neurofibrillary pathology. We identified RORB as a marker of selectively vulnerable excitatory neurons in the entorhinal cortex, and subsequently validated their depletion and selective susceptibility to neurofibrillary inclusions during disease progression using quantitative neuropathological methods. We also discovered an astrocyte subpopulation, likely representing reactive astrocytes, characterized by decreased expression of genes involved in homeostatic functions. Our characterization of selectively vulnerable neurons in AD paves the way for future mechanistic studies of selective vulnerability and potential therapeutic strategies for enhancing neuronal resilience.

INTRODUCTION

Selective vulnerability is a fundamental feature of neurodegenerative diseases, in which different neuronal populations show a gradient of susceptibility to degeneration. Selective vulnerability at the network level has been extensively explored in Alzheimer's disease (AD)¹⁻³. However, little is known about the mechanisms underlying selective vulnerability at the cellular level in AD, which could provide insight into disease mechanisms and lead to therapeutic strategies.

The entorhinal cortex (EC) is one of the first cortical brain regions to exhibit neuronal loss in AD⁴. Neurons in the external EC layers, especially in layer II, accumulate tau-positive neurofibrillary inclusions and die early in the course of AD⁵⁻¹⁰. However, these selectively

vulnerable neurons have yet to be characterized at the molecular level. Furthermore, it is unknown whether there are differences in vulnerability among subpopulations of these neurons. Although rodent models of AD have offered important insights, the available models fail to simultaneously capture some critical disease processes, such as the accumulation of neurofibrillary inclusions and neuronal loss¹¹, limiting the extrapolation of findings from rodent models to address selective vulnerability.

More recently, single-nucleus RNA-sequencing (snRNA-seq) has enabled large-scale characterization of transcriptomic profiles of individual cells from post-mortem human brain tissue^{12, 13}. However, snRNA-seq studies of AD published to date have focused on cell-type specific differential gene expression between AD cases and healthy controls^{14, 15}, without explicitly addressing selective vulnerability.

Here, we performed snRNA-seq on post-mortem brain tissue from a cohort of cases spanning the progression of AD-type tau neurofibrillary pathology to characterize changes in the relative abundance of cell types and cell type subpopulations. We discovered a selectively vulnerable subpopulation of excitatory neurons in the EC and validated the selective depletion of this subpopulation during AD progression with quantitative histopathology, using multiplex immunofluorescence in EC regions delineated by rigorous cytoarchitectonic criteria. Furthermore, we uncovered an astrocyte subpopulation likely corresponding to reactive astrocytes that showed downregulation of genes involved in homeostatic function.

RESULTS

Cohort selection and cross-sample alignment

We performed snRNA-seq on cell nuclei extracted from postmortem brain tissue (see Methods) from the EC at the level of the mid-uncus and from the superior frontal gyrus (SFG) at the level of the anterior commissure (Brodmann area 8), from 10 male *APOE* $\epsilon 3/\epsilon 3$ individuals

representing the cortical-free, early and late stages of AD-type tau neurofibrillary pathology (Braak stages¹ 0, 2 and 6; **Fig. 2.1a, Table 2.1**). The neuropathological hallmarks of AD are amyloid plaques and neurofibrillary inclusions. Since the accumulation of neurofibrillary inclusions measured by the Braak staging system is the best correlate of clinical cognitive decline, after neuronal loss¹⁶, we reasoned that profiling matched EC and SFG samples across different Braak stages would allow us to isolate the effect of disease progression on cell types and cell type subpopulations.

A challenge in characterizing the impact of disease progression on different cell type subpopulations is that these subpopulations need to be defined in a way that is independent from the effect of disease progression. Typically, cell type subpopulations are defined by subgrouping cells of the same cell type through cluster analysis (i.e. clustering), followed by examination of marker gene expression in the resulting clusters. To remove the effect of disease progression on clustering, we performed, prior to clustering, cross-sample alignment of the data from each brain region using scAlign (see Methods). Importantly, after identifying clusters in the alignment space, we used the original data for subsequent analyses involving examination of gene expression, such as identifying differentially expressed genes between clusters.

Changes in broad cell type composition with neuropathological AD progression

After quality control (see Methods), we recovered 42,528 cells from the EC and 63,608 cells from the SFG. Examination of the average number of genes and unique molecular identifiers (UMIs) detected per cell showed similar or superior transcript coverage compared to previously published AD snRNA-seq datasets^{14, 15} (**Fig. S2.1a,b**).

After cross-sample alignment, we performed clustering and recovered clusters that demonstrated spatial grouping in t-stochastic neighborhood embedding (tSNE) largely uncorrelated with the individual of origin (**Fig. 2.1b,c**). Furthermore, the clusters showed specific

expression of cell type markers and grouped in a manner consistent with their expression of cell type markers in hierarchical clustering (**Fig. 2.1d,e**, see Methods). For comparison, we also performed clustering without cross-sample alignment, which resulted in many clusters that were defined by individual of origin in addition to cell type (**Fig. S2.1c-f**). Having confirmed the effectiveness of cross-sample alignment in removing the effect of technical and experimental factors on clustering, we then assigned clusters to broad cell types (i.e. excitatory neurons, inhibitory neurons, astrocytes, oligodendrocytes, oligodendrocyte precursor cells, microglia, and endothelial cells) based on their expression of cell type markers (**Fig. 2.1d,e**, see Methods).

Next, to assess whether the proportions of broad cell types change with disease progression, we aggregated clusters assigned to the same cell type for each individual and then computed the relative abundance of each cell type in each individual. We tested for statistical significance using beta regression and corrected for multiple testing using Holm's method (see Methods). While there were not many statistically significant changes in the relative abundance of cell types, we observed a downward trend in the relative abundance of EC excitatory neurons in Braak stages 2 ($P_{\text{unadjusted}} = 0.18$) and 6 ($P_{\text{unadjusted}} = 0.02$), and of SFG excitatory neurons only in Braak stage 6 ($P_{\text{unadjusted}} = 0.05$), consistent with early involvement of the EC and sparing of the SFG until late Braak stages, and the previously described greater vulnerability of excitatory neurons relative to inhibitory neurons in AD^{17, 18}.

Selective vulnerability of excitatory neuron subpopulations

Based on these observations, we next asked whether specific subpopulations of excitatory neuron show a decline in their relative abundance with disease progression, by performing subclustering of excitatory neurons in the EC and SFG after cross-sample alignment (see Methods). The EC, a relatively phylogenetically conserved brain structure in mammals, is among the first cortical fields to accumulate tau-positive neurofibrillary inclusions followed by neuronal loss in AD¹. The EC is a heterogeneous structure and cytoarchitectonic considerations

matter when analyzing and sampling this region to avoid biased observations¹⁹. During evolution, the position of the EC changed, and the mouse medial EC (the source of our layer-specific marker genes) is generally regarded as the equivalent of the caudal EC in humans (our sampling location)^{20, 21}.

In the EC, we discerned nine excitatory neuron subpopulations (**Fig. 2.2a-d**). These subpopulations exhibited distinct expression of EC layer-specific genes identified in the mouse medial EC²². Notably, subpopulation EC:Exc.s2 showed a striking ~50% decrease in its relative abundance in Braak stage 2 compared to Braak stage 0, with no further decrease in Braak stage 6 (**Fig. 2.2c**), suggesting depletion early in disease. EC:Exc.s1 and EC:Exc.s4 similarly exhibited a ~50-60% reduction in their relative abundance in Braak stage 2. EC:Exc.s1, EC:Exc.s2, and EC:Exc.s4 expressed genes associated with mouse EC layer II (**Fig. 2.2c**), consistent with the fact that tau neurofibrillary inclusions are known to accumulate preferentially in human EC layer II early in AD⁵⁻⁸. However, not all subpopulations expressing genes associated with mouse EC layer II showed similar levels of early vulnerability. For example, EC:Exc.s6 and EC:Exc.s8 did not demonstrate statistically significant changes in their relative abundance across disease progression. We failed to find evidence of selective vulnerability in neuronal subpopulations expressing genes associated with mouse EC layer III (EC:Exc.s0) or V/VI (EC:Exc.7, EC:Exc.s5, EC:Exc.s3). In fact, EC:Exc.s5 exhibited a statistically significant increase in its relative abundance in Braak stage 2. Since neurons are post-mitotic, this increase is likely due to the selective earlier depletion of more vulnerable excitatory neuron subpopulations, followed by later depletion of EC:Exc.s5.

To identify molecular markers of selectively vulnerable excitatory neuron subpopulations in the EC (EC:Exc.s2, EC:Exc.s4, EC:Exc.s1), we inspected transcript levels of genes differentially expressed between pairs of subpopulations and curated a set of genes which were specifically expressed by no more than four subpopulations (**Fig. S2.2a**), which we decided was a reasonable threshold for a positive marker to be useful. We found that EC:Exc.s2 and

EC:Exc.s4 specifically expressed *RORB*, *CTC-340A15.2* and *CTC-535M15.2* (**Fig. 2.2c**). *RORB* (RAR-related Orphan Receptor B) encodes a transcription factor known as a marker and developmental driver of layer IV neurons in the neocortex²³⁻²⁵, but is also expressed by neurons in other layers¹³. Little is known about the non-coding transcripts *CTC-340A15.2* and *CTC-535M15.2* in the context of neuronal identity and function. We also found that EC:Exc.s1 was marked by high expression of *CDH9* (**Fig. 2.2c**), which encodes a cadherin with neuron-specific expression. However, *CDH9* was also expressed by other excitatory neuron subpopulations in the EC, and we could not find markers that were specifically expressed only in EC:Exc.s1. Therefore, we chose to focus our analysis on EC:Exc.s2 and EC:Exc.s4.

In addition to identifying molecular markers of the selectively vulnerable EC:Exc.s2 and EC:Exc.s4 neurons, we also enumerated genes that were differentially expressed in EC:Exc.s2 and EC:Exc.s4 compared to all other excitatory neurons in the EC, controlling for differences across individuals (see Methods). We found that genes with higher expression in EC:Exc.s2 and EC:Exc.s4 were enriched for axon-localized proteins and voltage-gated potassium channels, whereas genes with lower expression in EC:Exc.s2 and EC:Exc.s4 were enriched for synapse- and dendrite-localized proteins and pathways involving G-protein mediated signaling, ion transport, and neurotransmitter receptor signaling (**Fig. S2.2b-e**).

We also performed differential gene expression analysis across Braak stages for EC excitatory neuron subpopulations (see Methods), comparing Braak stage 6 vs. 0, which yielded the largest number of differentially expressed genes. We found a broad decrease in expression of genes encoding pre- and post-synaptic proteins in Braak stage 6 vs. 0 for many EC excitatory neuron subpopulations (**Fig. S2.3b,d,f**). Furthermore, we observed that the selectively vulnerable subpopulation EC:Exc.s2 had the largest number of downwardly differentially expressed genes and the strongest enrichments for pre- and post-synaptic proteins in these genes (**Fig. S2.3b,d**). Overall, the downregulation of synapse-related genes we have observed mirrors the findings from a recent preprint by Marinaro *et al.*²⁶, which examined the frontal cortex

in familial monogenic AD using snRNA-seq, and is consistent with a previous study of gene expression changes in AD in the entorhinal cortex and other brain regions employing laser capture microdissection of neurons followed by DNA microarray analysis²⁷.

We next examined excitatory neuron subpopulations in the SFG. Similar to previous studies^{12, 13}, we found that excitatory neuron subpopulations in the SFG (11 in total) expressed distinct sets of neocortical layer-specific genes (**Fig. 2.2b,d**), recapitulating the laminar organization of the neocortex. Interestingly, SFG:Exc.s4 and SFG:Exc.s2, which were marked by the vulnerability markers we identified in the EC (*RORB*, *CTC-340A15.2* and *CTC-535M15.2*), trended towards decreased relative abundance only in Braak stage 6 (**Fig. 2.2d**), consistent with the late appearance of neurofibrillary inclusions in the SFG starting at Braak stage 5. Although SFG:Exc.s7, which also expressed the EC vulnerability markers, exhibited a statistically significant decrease in relative abundance in Braak stage 2 but not 6, the magnitude of change was negligibly small.

Given that SFG:Exc.s4 and SFG:Exc.s2 expressed similar markers as EC:Exc.s4 and EC:Exc.s2, we wondered if SFG:Exc.s4 and SFG:Exc.s2 may resemble EC:Exc.s4 and EC:Exc.s2 more broadly at the transcriptome level. SFG:Exc.s4 and SFG:Exc.s2 were indeed most similar to EC:Exc.s4 and EC:Exc.s2 based on the Pearson correlation coefficient between the expression profiles of SFG and EC subpopulations (**Fig. 2.2e**). We observed the same pattern when we mapped subpopulations in the EC to those in the SFG by performing cross-sample alignment for both brain regions jointly (**Fig. S2.4**). This similarity is consistent with the reported similarity between deep layer neocortical excitatory neurons and EC excitatory neurons in general²⁸. The similarity in transcriptomes of vulnerable excitatory neurons in different brain regions is intriguing and suggests similar mechanisms of selective vulnerability in different brain regions.

Although the decrease in the relative abundance of SFG:Exc.s2 and SFG:Exc.s4 in Braak stage 6 was not statistically significant after correction for multiple testing, we asked if we

could detect signs of selective vulnerability in neocortical *RORB*-expressing excitatory neurons in an independent dataset with a larger sample size. To this end, we reanalyzed data from Mathys *et al.*¹⁴, which profiled the prefrontal cortex from 24 AD cases and 24 healthy controls, with our cross-sample alignment pipeline and performed subclustering of excitatory neurons. In the Mathys *et al.* dataset¹⁴, we discerned 10 excitatory neuron subpopulations, each of which expressed distinct sets of neocortical layer-specific genes (**Fig. S2.5a,b**) similar to Lake *et al.*¹² and our dataset. Of these 10 subpopulations, Mathys:Exc.s4, Mathys:Exc.s5, and Mathys:Exc.s1 expressed *RORB* at high levels (*CTC-340A15.2* and *CTC-535M15.2* were not available in the pre-processed Mathys *et al.*¹⁴ data). Importantly, we observed a statistically significant decrease in the relative abundance of Mathys:Exc.s4 in male AD cases vs. controls (**Fig. S2.5b**), recapitulating the selective vulnerability observed in our dataset, which consists only of male individuals. Furthermore, gene expression correlation analysis showed that Mathys:Exc.s4 was the most similar to EC:Exc.s2 and EC:Exc.s4 (**Fig. S2.5c**), again demonstrating similarity between selectively vulnerable excitatory neurons in the neocortex and those in the EC.

Although we did not detect any statistically significant changes in the relative abundance of *RORB*-expressing subpopulations in female individuals in Mathys *et al.*¹⁴, Mathys:Exc.s1 trended towards decreased relative abundance in female AD cases ($P_{\text{unadjusted}} = 0.17$) and mapped to EC:Exc.s2 by gene expression correlation (**Fig. S2.5b,c**). Furthermore, Marinaro *et al.*²⁶ included both male and female cases of monogenic AD and also reported the selective vulnerability of two out of four *RORB*-expressing excitatory neuron subpopulations in the prefrontal cortex (ExcB1 and ExcB4)²⁶, providing further evidence that subsets of *RORB*-expressing excitatory neurons in the neocortex are selectively vulnerable.

Considering the Mathys *et al.*¹⁴ and the Marinaro *et al.*²⁶ datasets together with our dataset, it appears that while not all *RORB*-expressing excitatory neuron subpopulations in the

neocortex showed signs of selective vulnerability, those that did were the most similar to *RORB*-expressing excitatory neurons in the EC, all of which showed signs of selective vulnerability.

Validation of the selective vulnerability of *RORB*-expressing excitatory neurons

To validate our finding that *RORB*-expressing excitatory neurons in the EC were highly vulnerable in AD, we performed multiplex immunofluorescence on postmortem brains of 26 individuals spanning Braak stages 0 to 6, who were devoid of non-AD neuropathological changes (**Table 2.1**). Specifically, we quantified the proportion of excitatory neurons and *RORB*-positive excitatory neurons in the EC superficial layers (i.e. above layer IV, which we also refer to as dissecans-1¹⁹ in **Fig. 2.3b**). Given EC heterogeneity, we used rigorous cytoarchitectonic parameters to delineate the caudal EC and minimize artifactual results (**Fig. 2.3a-c**, **Fig. S2.6**, see Methods). We used multiplex immunofluorescence²⁹ to label nuclei (DAPI), excitatory neurons (TBR1), *RORB*+ neurons, and phospho-tau neuronal inclusions (CP-13, Ser 202). We observed a substantial reduction in the proportion of *RORB*+ neurons among excitatory neurons in Braak stages 2-4 and 5-6 compared to Braak stages 0-1 (**Fig. 2.3d,e**). Furthermore, by analyzing a subset of cases, we detected phospho-tau (CP-13) preferentially in *RORB*+ compared to *RORB*- excitatory neurons (**Fig. 2.3f-g**). Thus, our results substantiate that *RORB*-expressing excitatory neurons are highly vulnerable in AD and support a model in which their depletion is a consequence of accumulating tau neurofibrillary changes.

Given that large multipolar neurons of “stellate” morphology in EC layer II are particularly vulnerable in AD⁵⁻⁸, we examined the morphological features of layer II’s *RORB*+ excitatory by overlaying immunofluorescence with Nissl staining. We found that *RORB*+ excitatory neurons adopted various shapes, including pyramidal and multipolar morphologies (**Fig. 2.3h**). Conversely, some large multipolar neurons are *RORB*-negative (**Fig. 2.3h**). Our results are consistent with the known vulnerability of large multipolar EC layer II neurons and demonstrate

that molecular characterization of vulnerable neurons refines the results of morphological studies.

Lack of differences in vulnerability of inhibitory neuron subpopulations

We next examined inhibitory neurons, which are more resistant to tau pathology than excitatory neurons in AD^{17, 18}. In both brain regions, inhibitory neuron subpopulations expressed distinct sets of inhibitory neuron subtype markers (**Fig. 2.4a-d**), consistent with previous studies^{12, 13}. We did not detect statistically significant changes in the relative abundance of inhibitory neuron subpopulations in the EC or SFG (**Fig. 2.4c-d**), or in the prefrontal cortex in Mathys *et al.*¹⁴ (**Fig. S2.7**). Although Marinaro *et al.* reported broad depletion of inhibitory neuron subpopulations in familial monogenic AD, there was no strong evidence of *selective* vulnerability in particular inhibitory neuron subpopulations relative to other inhibitory neuron subpopulations in Marinaro *et al.*

Analysis of glial subpopulations

Glial cells have emerged as important players in AD. We found a trend towards increased relative abundance of microglia in the EC in with AD progression (**Fig. 2.1f**), consistent with microgliosis. Next, we asked whether a specific transcriptional state of microglia is associated with AD in our dataset. Recent single-cell profiling of microglia from mouse models of AD identified disease-associated microglia³⁰ (DAM), the transcriptional signature of which overlap only partially with that of human microglia found in AD³¹. Considering the possibility that DAMs may cluster separately from homeostatic microglia after cross-sample alignment, we performed subclustering of microglia in our dataset, discerning 4 subpopulations in the EC and 5 subpopulations in the SFG (**Fig. S8a-b**). However, similar to Thrupp *et al.*³², we were unable to detect the expression of the majority of homeostatic microglia markers and DAM markers in our dataset or in Mathys *et al.*¹⁴ (**Fig. S2.8d-f**), which may be due to the relatively low number of

genes captured in microglia compared to other cell types (**Fig. 2.1h-i**) and the depletion of many DAM markers in nuclei compared to whole cells³².

We next examined oligodendrocytes, which were shown by Mathys *et al.*¹⁴ to exhibit a strong transcriptional response in AD. Subclustering of oligodendrocytes in the EC and SFG revealed subpopulations (EC:Oligo.s0 and EC:Oligo.s4, SFG:Oligo.s1 and SFG:Oligo.s2) which exhibited higher expression of AD-associated oligodendrocyte genes from Mathys *et al.*¹⁴, i.e. genes with higher expression in the AD-associated subpopulation Oli0 in Mathys *et al.*¹⁴ (**Fig. S2.9d-e**). Although the function of these genes in the context of AD is largely unknown, a spatial transcriptomics study of AD³³ has recently implicated a subset of these genes in the response of oligodendrocytes to amyloid plaques (e.g. *CRYAB*, *QDPR*).

Finally, we turned our attention to astrocytes. While reactive astrocytes are ubiquitously associated with AD pathology³⁴, only few studies to date have directly profiled reactive astrocytes due to the difficulty of specifically isolating reactive astrocytes^{35, 36}. Similarly to our interrogation of microglia, we asked if reactive astrocytes would cluster separately from non-reactive astrocytes after cross-sample alignment. After subclustering of astrocytes in our dataset, we discerned 4 subpopulations in the EC and 6 subpopulations in the SFG (**Fig. 2.5a-d**). In each brain region, there was at least one subpopulation (EC:Astro.3, SFG:Astro.s4 and SFG:Astro.s5) that expressed dramatically higher levels of *GFAP*, which we will refer to as *GFAP*_{high} astrocytes (**Fig. 2.5c,d**). In the EC, *GFAP*_{high} astrocytes also expressed *CD44* and *HSPB1*, markers of pan-reactive astrocytes³⁷; *TNC*, which is upregulated in stab-wound reactive astrocytes³⁸; and *HSP90AA1*, which is upregulated in reactive astrocytes associated with middle cerebral artery occlusion³⁹ (**Fig. 2.5c,d**). Interestingly, in the SFG, *GFAP*_{high} astrocytes consisted of two subpopulations, one marked by higher expression of *CD44* and *TNC*, both of which are involved in interactions with the extracellular matrix, and the other marked by higher expression of *HSPB1* and *HSP90AA1*, both of which are chaperones involved in proteostasis. In terms of downregulated genes, *GFAP*_{high} astrocytes consistently expressed lower levels of genes

associated with glutamate/GABA homeostasis (*SLC1A2*, *SLC1A3*, *GLUL*, *SLC6A11*) and synaptic adhesion/maintenance (*NRXN1*, *CADM2*, *PTN*, *GPC5*), suggesting a loss of homeostatic function.

Examination of all differentially expressed genes in *GFAP*_{high} astrocytes showed significant overlap with differentially expressed genes from reactive astrocytes in a mouse model of spinal cord injury⁴⁰ (**Fig. 2.5e**). Overlapping downregulated genes included the previously noted genes associated with glutamate homeostasis and synaptic adhesion/maintenance and also genes related to lipid metabolism, cytoskeleton and extracellular matrix, and transporters (**Fig. 2.5f-g**).

Finally, to confirm the presence of *GFAP*_{high} astrocytes in an independent dataset, we performed subclustering of astrocytes from Mathys et al.¹⁴ after cross-sample alignment, which yielded 3 subpopulations (**Fig. S2.10a,b**). Indeed, we found that Mathys:Astro.s2 behaved identically compared to *GFAP*_{high} astrocytes in our dataset in terms of upregulating reactive astrocyte markers and downregulating genes associated with glutamate/GABA homeostasis and synaptic adhesion (**Fig. S2.10b**). Furthermore, the differentially expressed genes in Mathys:Astro.s3 overlapped highly with those in *GFAP*_{high} astrocytes in our dataset (**Fig. S2.10c**).

DISCUSSION

Selective vulnerability is a fundamental feature of neurodegenerative diseases, including AD. Past studies have characterized the most vulnerable neurons in AD based on topography and morphology. For instance, EC layer II neurons are more vulnerable than EC layer III pyramidal neurons⁸⁻¹⁰. However, the molecular signature of selectively vulnerable neurons in AD is largely unknown.

Using a combination of snRNA-seq and quantitative neuropathology in postmortem human brains, we discovered that in the caudal EC, specific excitatory neuron subpopulations defined by snRNA-seq were selectively vulnerable in AD. These neurons expressed genes associated with layer II of the mouse medial EC, consistent with the known vulnerability of neurons in superficial layers of the human EC in AD⁵⁻⁸. We identified and validated *RORB* as a marker of these selectively vulnerable excitatory neuron subpopulations. Selectively vulnerable *RORB*+ excitatory neurons included both large multipolar neurons and pyramidal neurons. Our findings demonstrates that morphology alone is insufficient to determine selective vulnerability.

We also found that tau neuronal inclusions, a chief AD neuropathological hallmark, preferentially accumulated in *RORB*+ excitatory neurons in the EC. To uncover potential cell biological mechanisms underlying the vulnerability of EC *RORB*+ excitatory neurons, we compared the gene expression profiles of EC *RORB*-expressing excitatory neurons against all other EC excitatory neurons, which revealed differences in the expression of genes encoding synapse- vs. axon-localized proteins, potassium channel subunits, G-protein signaling molecules, and neurotransmitter receptor signaling molecules. Future studies utilizing *in vitro* and animal models of AD together with techniques for manipulating gene expression such as CRISPR inhibition and activation⁴¹⁻⁴³ will make it possible to address these potential mechanistic connections among *RORB*-expression, phospho-tau accumulation, and vulnerability.

In neocortical areas, layers III and V are the first to accumulate tau neurofibrillary inclusions in AD^{1, 44, 45}. Our dataset, together with our re-analysis of datasets from Mathys *et al.*¹⁴ and Marinaro *et al.*²⁶ suggests that in the neocortex, vulnerable excitatory neuron subpopulations express *RORB* and have a similar transcriptional profile as selectively vulnerable neurons in the EC, although not all neocortical *RORB*+ neurons are vulnerable. Given that *RORB* is known to function as a developmental driver of neuronal subtype identity in the neocortex²³⁻²⁵, we hypothesize that the vulnerability of *RORB*-expressing excitatory neuron subpopulations in different brain regions may be caused by gene expression programs driven

by RORB and potentially other subtype-determining transcription factors. Further mechanistic studies involving the perturbation of *RORB* expression in cell-based or animal models of AD are necessary to test this hypothesis.

A previous study suggested changes in the number of neurons expressing calbindin and parvalbumin, which tend to mark inhibitory neurons, in EC layer II in AD⁴⁶. Here, we found no evidence of selective vulnerability in inhibitory neurons subpopulations in EC layer II or any other layer. Inhibitory neurons in EC superficial layers show a gradient of abundance in the various EC regions²⁰, which could confound the results. But, given that we used strict cytoarchitectonic criteria to sample the EC, it is unlikely that our results reflect comparisons of different EC areas across the cases. Evidence suggests that these inhibitory neurons undergo changes in morphology and function, rather than loss in sporadic AD⁴⁶. Thus, our results do not preclude the possibility that inhibitory neuron subpopulations may be differentially affected by AD progression at the morphological and functional level, even if neuronal loss is not apparent.

Accumulating evidence is highlighting the importance of glial changes in AD . We discovered an astrocyte subpopulation expressing high levels of *GFAP*, which we termed *GFAP*_{high} astrocytes, in both EC and SFG, and in prefrontal cortex from Mathys *et al.*¹⁴ We found that *GFAP*_{high} astrocytes expressed higher levels of other genes associated with reactive astrocytes, and lower levels of genes involved in astrocyte homeostatic functions. Furthermore, we found a high degree of overlap between genes differentially expressed in *GFAP*_{high} astrocytes and genes differentially expressed in reactive astrocytes from a mouse model of spinal injury⁴⁰. Thus, we believe that *GFAP*_{high} astrocytes correspond to reactive astrocytes in AD, which may have compromised homeostatic function.

Our study has several methodological strengths. First, the postmortem cohort used for snRNA-seq and histopathological validation consists of well-characterized cases, devoid of non-AD pathology. To minimize confounders in the snRNA-seq results, we selected only male cases with an *APOE* ϵ 3/ ϵ 3 genotype. Second, we sequenced a very large number of nuclei from

each case (~10,000 nuclei per case, compared to ~1,700 nuclei per case in Mathys *et al.*¹⁴) from two brain regions per individual (~4,000 nuclei from the EC and ~6,000 nuclei from the SFG). Third, we used strict cytoarchitectonic criteria to sample brain regions for snRNA-seq and histopathological validation, instead of broadly defined sampling areas used by previous studies. Fourth, our focus was on defining cell type subpopulations that showed changes in relative abundance between disease stages, which can reflect important disease processes such as neuronal loss, and to define the genes characteristic of these subpopulations. By defining cell type subpopulations independently of disease progression, we could compare gene expression between subpopulations within individuals while controlling for differences among individuals; this is more robust than comparing gene expression in a given subpopulation across groups of individuals, which can be influenced by differences in confounding factors between the groups. Lastly, by validating our findings using a novel multiplex immunofluorescence approach²⁹, we could quantify the relative abundance of excitatory neurons and RORB+ neurons and also demonstrate that RORB+ excitatory neurons were preferentially affected by neurofibrillary inclusions.

A limitation of our study is that we only included male *APOE* ϵ 3/ ϵ 3 individuals in the snRNA-seq analysis. We included females and individuals carrying the *APOE* ϵ 4 allele associated with AD risk in our histopathological validation, but caution should be taken before generalizing our results to these groups. Future studies will provide a systematic analysis of the impact of sex and *APOE* status on selective vulnerability in AD.

In conclusion, our study contributes a pioneering characterization of selectively vulnerable neuronal populations in AD using snRNA-seq profiling of paired brain regions from the same individuals, which were all carefully curated AD cases and controls. These results will inform future studies of the mechanistic basis of selective vulnerability in both animal and *in vitro* models, such as human iPSC-derived neurons, in which the deployment of CRISPR inhibition

and activation technology enables elucidation of the functional consequences of transcriptomic changes^{41, 47}.

DATA AVAILABILITY

The raw snRNA-seq sequencing data and unfiltered UMI count matrices are available on the Gene Expression Omnibus (GEO) under the accession GSE147528 (<https://www.ncbi.nlm.nih.gov/geo/query/acc.cgi?acc=GSE147528>). Single-cell data after quality control is available for download in synapse.org at under the Synapse ID syn21788402 (<https://www.synapse.org/#!/Synapse:syn21788402>). Post- quality control data can also be explored interactively through the CellXGene platform at <https://kampmannlab.ucsf.edu/ad-brain>. Data from Mathys *et al.*¹⁴ was downloaded from Synapse under Synapse ID syn18485175 (<https://www.synapse.org/#!/Synapse:syn18485175>).

CODE AVAILABILITY

We provide the full bioinformatics pipeline for the analysis of snRNA-seq data in this paper at <https://kampmannlab.ucsf.edu/ad-brain-analysis>.

ACCESSION CODES

Gene Expression Omnibus (GEO): GSE147528. Synapse: syn21788402, syn18485175.

ACKNOWLEDGEMENTS

We thank Angela Pisco, Ashley Maynard, Spyros Darmanis and MACA team at the Chan Zuckerberg Biohub for advice on analysis 10X library preparation and reagents. We thank members of the Kampmann lab (Avi Samelson, Xiaoyan Guo, Ruilin Tian, Brendan Rooney) for feedback on the manuscript. This work was supported by NIH awards F30 AG066418 (K.L.),

K08 AG052648 (S.S.), R56 AG057528 (M.K., L.T.G.), K24 AG053435 (L.T.G), U54 NS100717 (L.T.G, M.K.), an NDSEG fellowship (E.L.), Alzheimer's Association fellowship AARF 18-566005 (R.D.R.), FAPESP/CAPES (2016/24326-0) (R.D.R.) and a Chan Zuckerberg Biohub Investigator Award (M.K.). The UCSF Neurodegenerative Disease Brain Bank is supported by NIH grants AG023501 and AG019724, the Tau Consortium, and the Bluefield Project to Cure FTD.

AUTHOR CONTRIBUTIONS

K.L., E.L., L.T.G. and M.K. conceptualized and led the overall project. K.L., L.T.G. and M.K. wrote the manuscript, with input from all co-authors. K.L. analyzed snRNA-Seq data and visualized results. E.L. generated snRNA-Seq data, with support from R.S., M.T., and N.N. R.D.R., C.K.S., R.E.P.L., C.P. W.W.S., and S.S. contributed to neuropathological data generation and analysis, R.E., A.P. and H.H. contributed to neuropathological data analysis, and S.H.L. contributed to neuropathological method development.

COMPETING INTERESTS

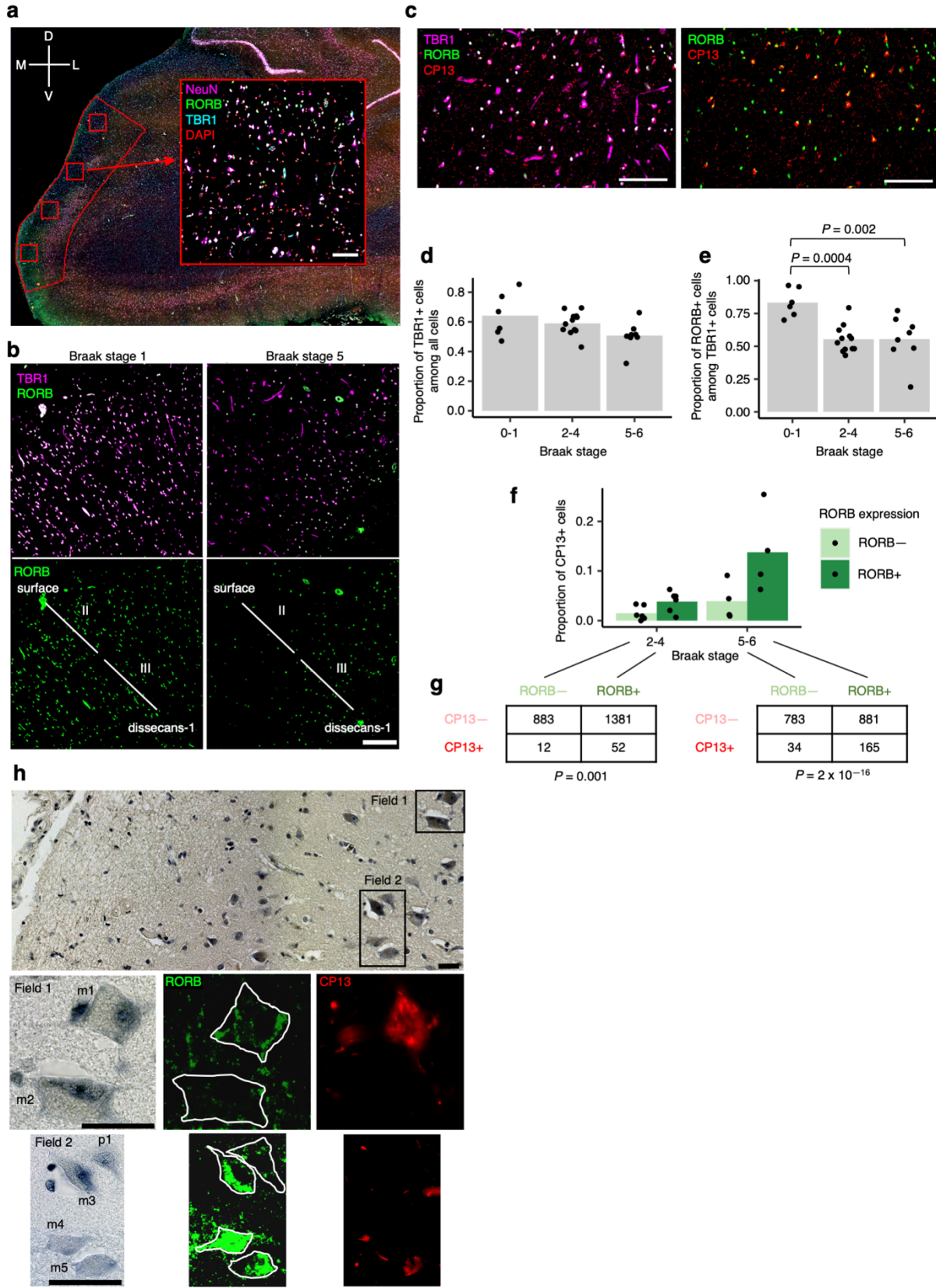
The authors declare no competing interests.

ETHICS DECLARATIONS

This project was approved the the ethical committee of the University of Sao Paulo (for tissue transfer) and deemed non-human subject research by UCSF.

the number of individuals sampled) was determined by beta regression and adjusted for multiple comparisons (see Methods). Cell type abbreviations: Exc – excitatory neurons, Oligo – oligodendrocytes, Astro – astrocytes, Inh – inhibitory neurons, OPC – oligodendrocyte precursor cells, Micro – microglia, Endo – endothelial cells.

average expression, respectively (see Methods). Relative abundance of subpopulations across Braak stages (second subpanel); for each brain region, statistical significance of differences in relative abundance across Braak stages (Braak 0 n=3, Braak 2 n=4, Braak 6 n=3, where n is the number of individuals sampled) was determined by beta regression and adjusted for multiple comparisons (see Methods). Expression heatmap of EC layer-specific genes identified from Ramsden *et al.*²² (**c**, third subpanel). Expression heatmap of neocortical layer-specific genes from Lake *et al.*¹² (**d**, third subpanel). Expression of selectively vulnerable subpopulation markers identified in the EC (bottom subpanel). **e**, Heatmap of Pearson correlation between the gene expression profiles of EC and SFG subpopulations.



(Legend overleaf)

Fig. 2.3 | Immunofluorescence of the EC validates selective vulnerability of RORB-expressing excitatory neurons. **a**, The method for extracting regions of interest (ROI) is illustrated using a representative brain slice used for immunofluorescence with the EC delineated in red. Four ROIs (drawn in red squares) were randomly distributed along the superficial layers of the EC and extracted for quantification after masking neurons (see Methods). A representative ROI image with DAPI, NeuN, TBR1, and RORB staining is shown. The anatomical orientation of the slice is provided in the top left corner (D – dorsal, V – ventral, M – medial, L – lateral). **b**, Representative RORB staining in a Braak stage 1 sample (left) vs. a Braak stage 5 sample (right), shown with (top) and without (bottom) excitatory neurons marked by TBR1 staining. The EC layers captured in the image are demarcated in the bottom subpanels (see Methods and Fig. S6). **c**, Representative CP13 staining in a Braak stage 6 sample, shown together with TBR1 and RORB staining (left) or only with RORB staining (right). **d-e**, Proportion of TBR1+ cells among all cells (**d**) or proportion of RORB+ cells among TBR1+ cells (**e**) averaged across ROIs for each individual across groups of Braak stages; statistical significance of differences in the above proportions across groups of Braak stages (Braak 0-1 n=6, Braak 2-4 n=12, Braak 5-6 n=8, where n is the number of individuals sampled) was determined by beta regression without adjustment for multiple comparisons. **f**, Proportion of CP13+ cells in RORB- or RORB+ excitatory neurons (i.e. TBR1+ cells) averaged across ROIs for each individual across groups of Braak stages. **g**, Contingency tables of raw counts of TBR1+ cells based on their RORB or CP13 staining status summed across ROIs and individuals for each group of Braak stages (Braak 2-4 n=6, Braak 5-6 n=4, where n is the number of individuals sampled); the Fisher's Exact Test p-value (two-sided) is shown below each table. **h**, Representative image of EC layer II neurons stained with gallocyanin (top subpanel) with the corresponding RORB and CP13 immunofluorescence signal shown in selected fields (Field 1 – middle subpanels, Field 2 – bottom subpanels). RORB+ neurons include both large multipolar neurons (m1, m3, m4, m5) and pyramidal neurons (p1). One large multipolar neuron (m2) is RORB-. The neuronal somas are outlined manually in white in the RORB immunofluorescence images to aid interpretation. Scale bars shown in **a-c** correspond to 100 microns; scale bars shown in **h** correspond to 15 microns. For all data shown in this figure, the experiment was performed once.

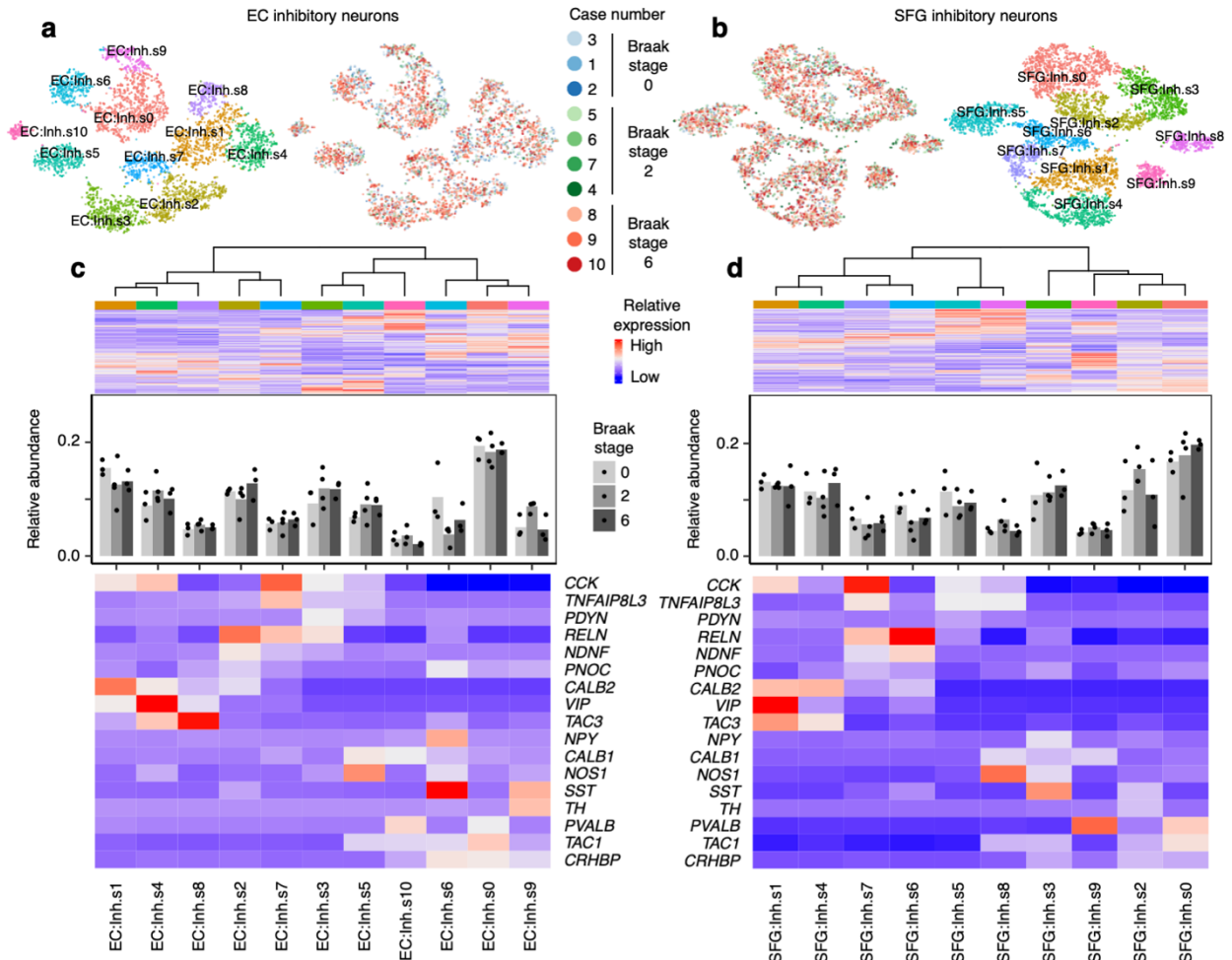
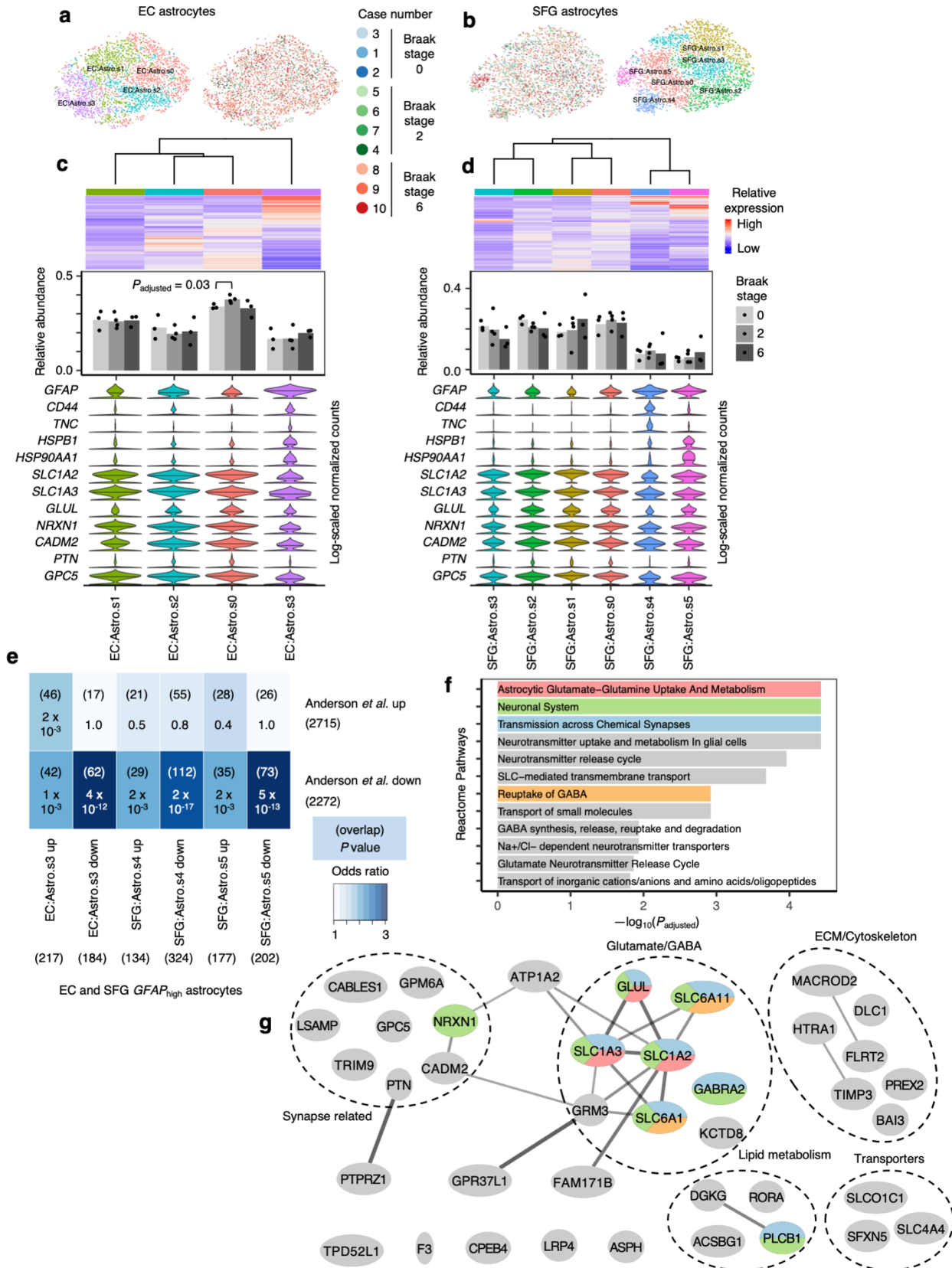


Fig. 2.4 | Inhibitory neuron subpopulations do not consistently show differences in resilience or vulnerability to AD progression. **a-b**, tSNE projection of inhibitory neurons from the EC (**a**) and SFG (**b**) in their respective alignment spaces, colored by individual of origin (center) or subpopulation identity (outer). **c-d**, Heatmap and hierarchical clustering of subpopulations and subpopulation marker expression (top subpanel); “High” and “Low” relative expression reflect above- and below-average expression, respectively (see Methods). Relative abundance of subpopulations across Braak stages (middle subpanel); for each brain region, statistical significance of differences in relative abundance across Braak stages (Braak 0 n=3, Braak 2 n=4, Braak 6 n=3, where n is the number of individuals sampled) was determined by beta regression and adjusted for multiple comparisons (see Methods). Expression heatmap of inhibitory neuron molecular subtype markers from Lake *et al.*¹² (bottom subpanel).



(Legend overleaf)

Fig. 2.5 | GFAP_{high} astrocytes show signs of dysfunction in glutamate homeostasis and synaptic support. **a-b**, tSNE projection of astrocytes from the EC (**a**) and SFG (**b**) in their respective alignment spaces, colored by individual of origin (center) or subpopulation identity (outer). **c-d**, Heatmap and hierarchical clustering of subpopulations and subpopulation marker expression (top subpanel); “High” and “Low” relative expression reflect above- and below-average expression, respectively (see Methods). Relative abundance of subpopulations across Braak stages (middle subpanel); for each brain region, statistical significance of differences in relative abundance across Braak stages (Braak 0 n=3, Braak 2 n=4, Braak 6 n=3, where n is the number of individuals sampled) was determined by beta regression and adjusted for multiple comparisons (see Methods). Expression of genes associated with reactive astrocytes, with median expression level marked by line (bottom subpanel). **e**, Enrichment analysis of overlap between differentially expressed genes in GFAP_{high} astrocytes vs. differentially expressed genes in reactive astrocytes from Anderson *et al.*⁴⁰ The number of genes in each gene set and the number of overlapping genes are shown in parentheses, and the hypergeometric test p-values (one-sided, corrected for multiple testing using the Benjamini-Hochberg procedure) are shown without parentheses. **f**, Enrichment of Reactome pathways in downregulated genes in GFAP_{high} astrocytes, with selected terms highlighted in color. **g**, Functional association network (see Methods) of downregulated genes shared between EC and SFG GFAP_{high} astrocytes that overlap with those in Anderson *et al.*⁴⁰ Genes with stronger associations are connected by thicker lines. Genes that belong to selected gene sets in **k** are highlighted in color.

Table 2.1 | Description of post-mortem cohort.

Asterisks denote cases used both for snRNA-seq and immunofluorescence validation. The AD neuropathological change (ADNC) score incorporates assessment of amyloid-beta deposits (“A”), staging of neurofibrillary tangles (“B”), and scoring of neuritic plaques (“C”) ⁴⁸. The Clinical Dementia Rating (CDR) reflects the degree of cognitive impairment ⁴⁹.

Cases used for snRNA-seq

Case #	Braak stage	Sex	Age at death (years)	Post-mortem interval (hours)	ADNC score	CDR before death	APOE genotype	Source
1	0	M	50	13	A0,B0,C0	0	E3/E3	BBAS
2	0	M	60	12	A0,B0,C0	0.5	E3/E3	BBAS
3	0	M	71	12	A1,B0,C0	0	E3/E3	BBAS
4	2	M	72	15	A1,B1,C0	0	E3/E3	BBAS
5*	2	M	77	4.9	A2,B1,C1	0.5	E3/E3	UCSF
6*	2	M	87	30	A2,B1,C2	2	E3/E3	UCSF
7*	2	M	91	50	A1,B1,C1	0	E3/E3	UCSF
8*	6	M	72	6.9	A3,B3,C3	3	E3/E3	UCSF
9*	6	M	82	6.7	A3,B3,C3	3	E3/E3	UCSF
10	6	M	82	9	A3,B3,C3	3	E3/E3	UCSF

Cases used for immunofluorescence validation

Case #	Braak stage	Sex	Age at death	Post-mortem interval (hours)	ADNC score	CDR before death	APOE genotype	Source
5*	2	M	77	4.9	A2,B1,C1	0.5	E3/E3	UCSF
6*	2	M	87	30	A2,B1,C2	2	E3/E3	UCSF
7*	2	M	91	50	A1,B1,C1	0	E3/E3	UCSF
8*	6	M	72	6.9	A3,B3,C3	3	E3/E3	UCSF
9*	6	M	82	6.7	A3,B3,C3	3	E3/E3	UCSF
11	0	F	62	10.1	A1,B0,C0	0	NA	BBAS
12	0	M	64	12	A0,B0,C0	0	E3/E3	BBAS
13	1	M	60	19	A0,B1,C0	0	NA	BBAS
14	1	F	64	13	A1,B1,C0	0	E3/E3	BBAS
15	1	M	70	11	A1,B1,C0	0	E3/E3	BBAS
16	1	F	82	9.6	A1,B1,C0	0	NA	BBAS
17	2	F	79	18	A1,B1,C1	0	E3/E3	BBAS
18	2	F	81	30.3	A1,B1,C0	NA	E3/E3	UCSF
19	3	M	81	8.3	A2,B2,C3	1	NA	UCSF
20	3	M	84	28	A3,B2,C2	1	NA	UCSF
21	3	F	88	9.8	A3,B2,C2	0.5	E3/E3	UCSF
22	3	M	89	9.1	A3,B2,C2	1	E3/E3	UCSF

Case #	Braak stage	Sex	Age at death	Post-mortem interval (hours)	ADNC score	CDR before death	APOE genotype	Source
23	4	F	87	9.5	A1,B2,C3	2	E3/E3	UCSF
24	4	M	91	11.2	A3,B2,C2	0.5	E3/E3	UCSF
25	4	M	103	7.8	A1,B2,C2	NA	E3/E3	UCSF
26	5	M	77	8.4	A3,B3,C3	0.5	E4/E4	UCSF
27	5	M	85	11.2	A3,B3,C3	1	E3/E3	UCSF
28	5	M	86	8.6	A3,B3,C3	2	E3/E4	UCSF
29	5	F	87	17	A3,B3,C2	3	E3/E3	BBAS
30	6	F	64	7.3	A3,B3,C3	3	E3/E4	UCSF
31	6	F	67	9.7	A3,B3,C3	3	E4/E4	UCSF

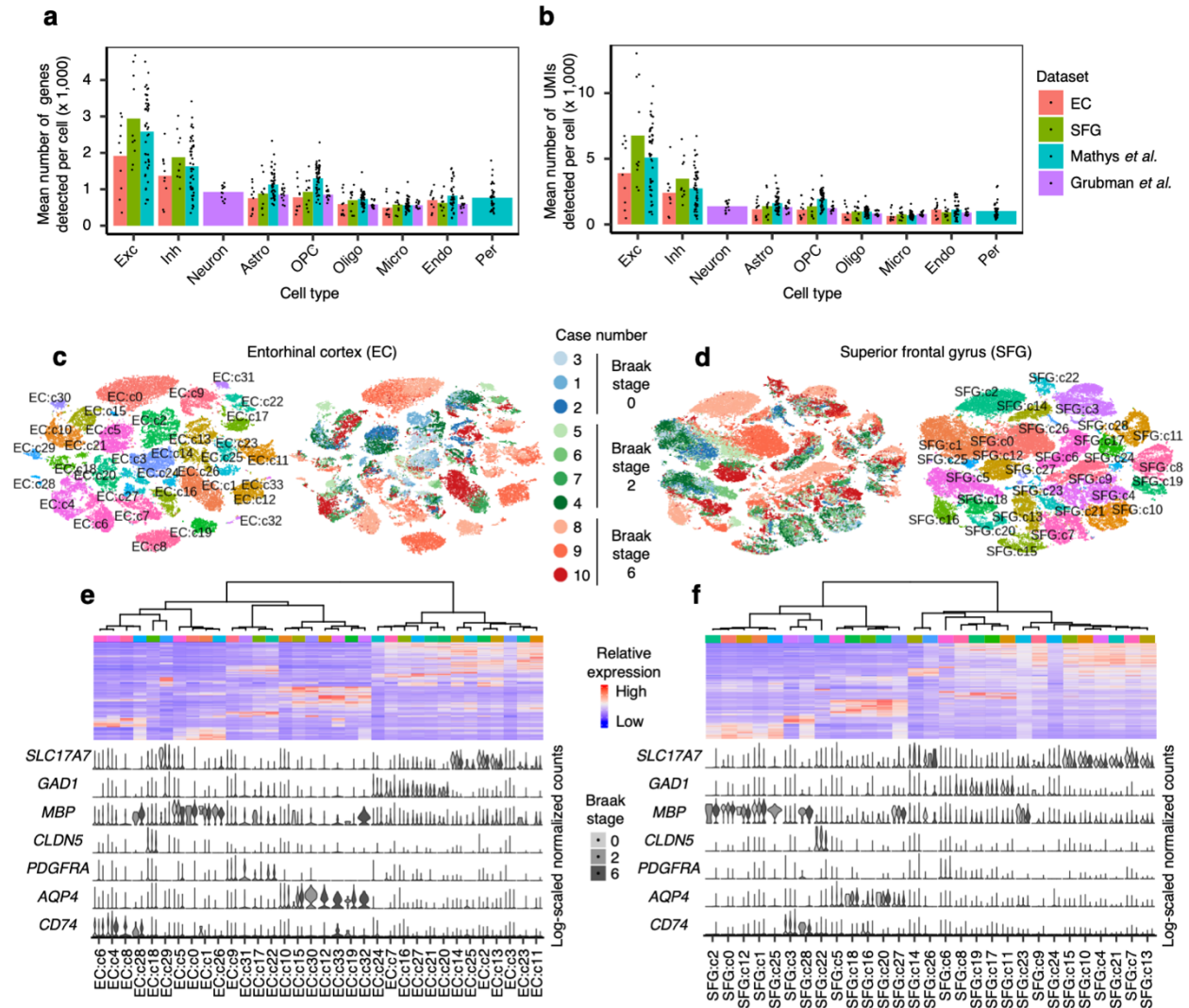


Fig. S2.1 | Data quality and initial clustering without cross-sample alignment. **a-b**, Mean number of genes (**a**) or UMIs (**b**) detected per cell across individual samples for major cell types identified in each dataset. Grubman *et al.*¹⁵ did not resolve excitatory neurons from inhibitory neurons. Pericytes were identified only in Mathys *et al.*¹⁴ Cell type abbreviations: Exc – excitatory neurons, Oligo – oligodendrocytes, Astro – astrocytes, Inh – inhibitory neurons, OPC – oligodendrocyte precursor cells, Micro – microglia, Endo – endothelial cells, Per – pericytes. **c-d**, tSNE projection of cells from the EC (**c**) and SFG (**d**) clustered without first performing cross-sample alignment, colored by individual of origin (center) or cluster assignment (outer). **e-f**, Heatmap and hierarchical clustering of clusters and cluster marker expression (top subpanels); “High” and “Low” relative expression reflect above- and below-average expression, respectively (see Methods). Expression of cell type markers (bottom subpanels).

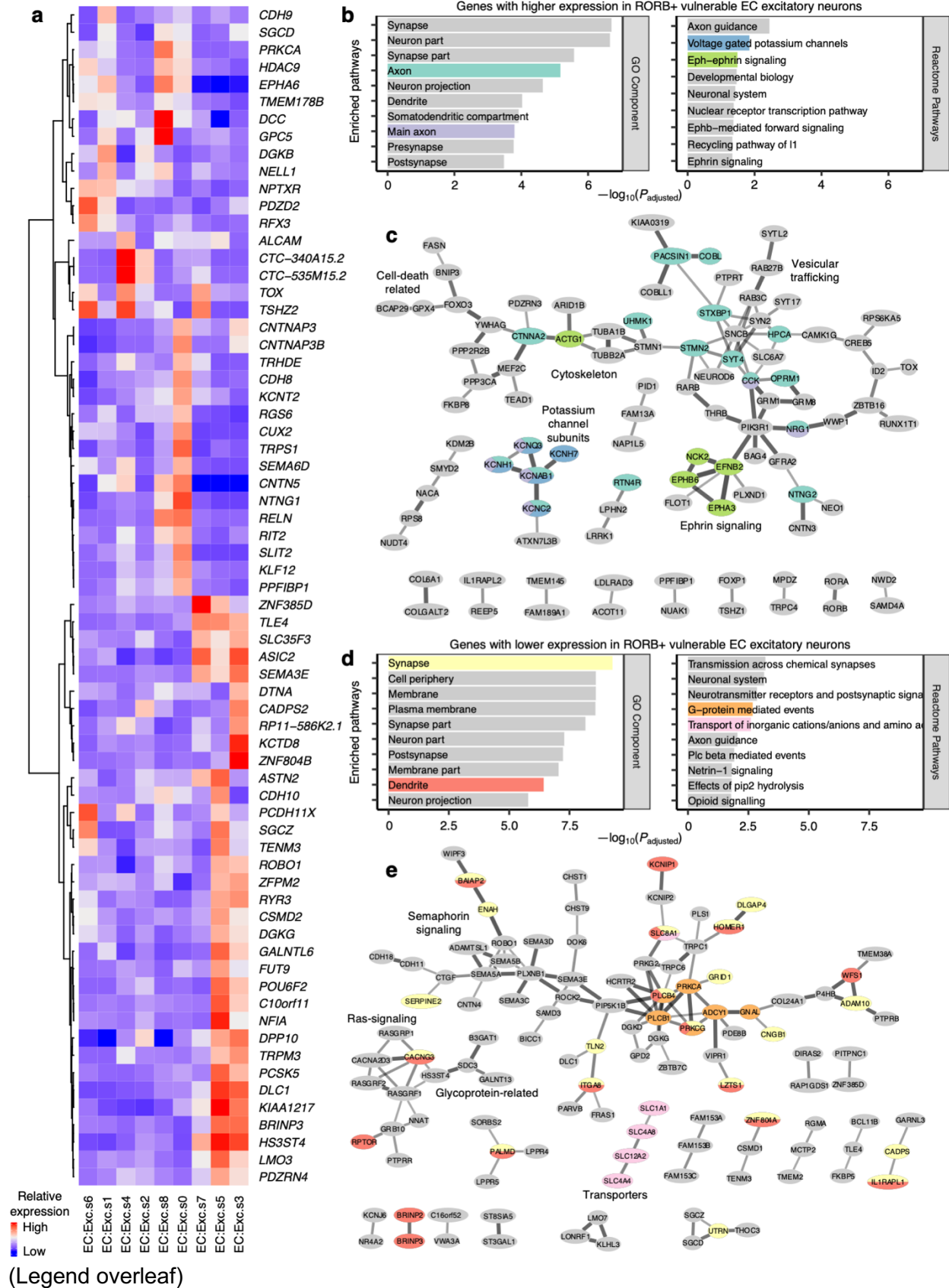


Fig. S2.2 | Expression of selected EC excitatory neuron subpopulation markers and pathway enrichment analysis of differentially expressed genes in selectively vulnerable EC excitatory neuron subpopulations. **a**, Expression heatmap of genes that are specifically expressed by four or fewer EC excitatory neuron subpopulations; “High” and “Low” relative expression reflect above- and below-average expression, respectively (see Methods). **b-d**, Enrichment analysis against Gene Ontology Cellular Component terms or Reactome Pathways (**b,d**) and functional association network analysis (**c,e**; see Methods) of genes with higher (**b-c**) or lower expression (**d-e**) in RORB+ vulnerable EC excitatory neurons, with selected terms highlighted by color. In panels **c** and **e**, genes with stronger associations are connected by thicker lines, and genes without known associations are not shown.

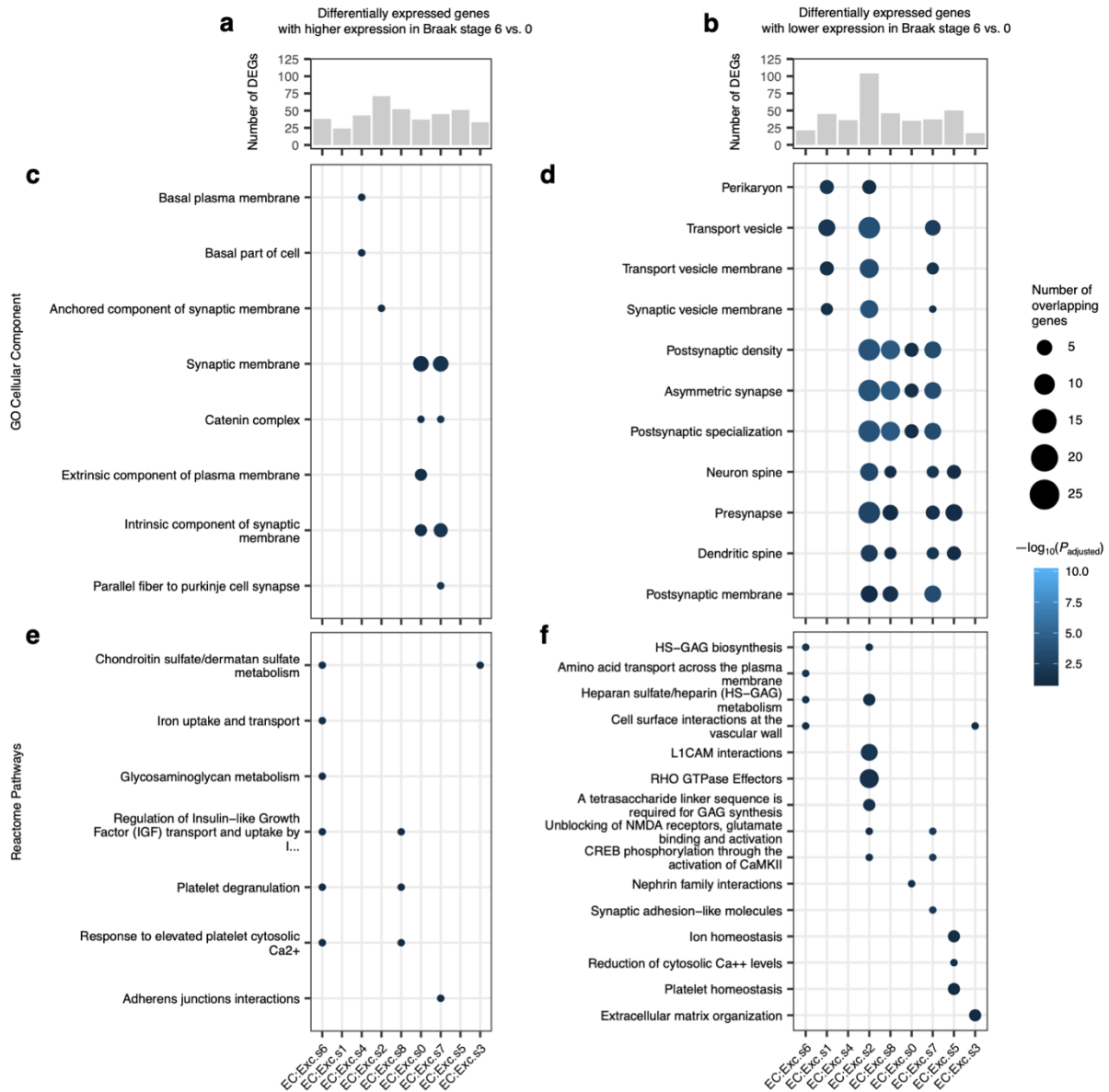
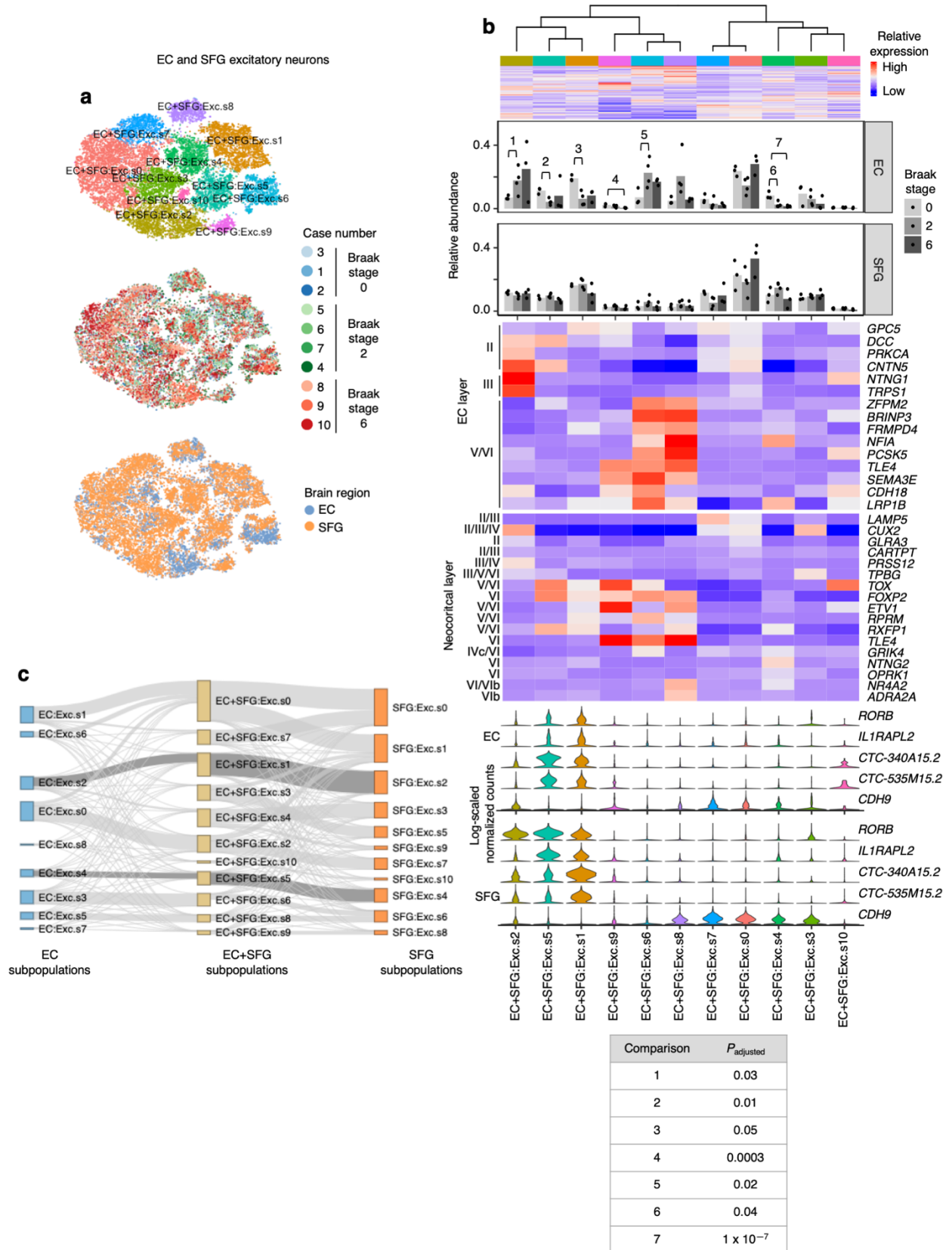


Fig. S2.3 | Differential expression analysis across Braak stages for EC excitatory neuron subpopulations. a-b, Number of differentially expressed genes in EC excitatory neuron subpopulations with higher (**a**) or lower (**b**) expression in Braak stage 6 vs. Braak stage 0. **c-f**, Enrichment analysis against Gene Ontology Cellular Component terms (**c-d**) or Reactome Pathways (**e-f**) of differentially expressed genes in EC excitatory neuron subpopulations with higher (**c,e**) or lower (**d,f**) expression in Braak stage 6 vs. Braak stage 0.



(Legend overleaf)

Fig. S2.4 | Alignment of EC and SFG maps homologous excitatory neuron subpopulations. **a**, tSNE projection of excitatory neurons from the EC and SFG in the joint alignment space, colored by subpopulation identity (top), individual of origin (middle), or brain region (bottom). **b**, Heatmap and hierarchical clustering of subpopulations and subpopulation marker expression (top subpanel); “High” and “Low” relative expression reflect above- and below-average expression, respectively (see Methods). Relative abundance of subpopulations across Braak stages (second and third subpanels); for each brain region, statistical significance of differences in relative abundance across Braak stages (Braak 0 n=3, Braak 2 n=4, Braak 6 n=3, where n is the number of individuals sampled) was determined by beta regression and adjusted for multiple comparisons (see Methods). Expression heatmap of EC layer-specific genes identified from Ramsden *et al.*²² (fourth subpanel). Expression heatmap of neocortical layer-specific genes from Lake *et al.*¹² (fifth subpanel). Expression of selectively vulnerable EC excitatory neuron subpopulation markers by excitatory neurons in the EC (sixth subpanel) or SFG (bottom subpanel). Significant beta regression *P* values (adjusted for multiple testing) are shown in a table at the bottom of the panel. **c**, Sankey diagram connecting subpopulation identity of excitatory neurons in the EC alignment space and the SFG alignment space to subpopulation identity in the EC+SFG alignment space. The links connecting EC:Exc.s2 and EC:Exc.s4 to SFG:Exc.s2 and SFG:Exc.s4, respectively, are highlighted.

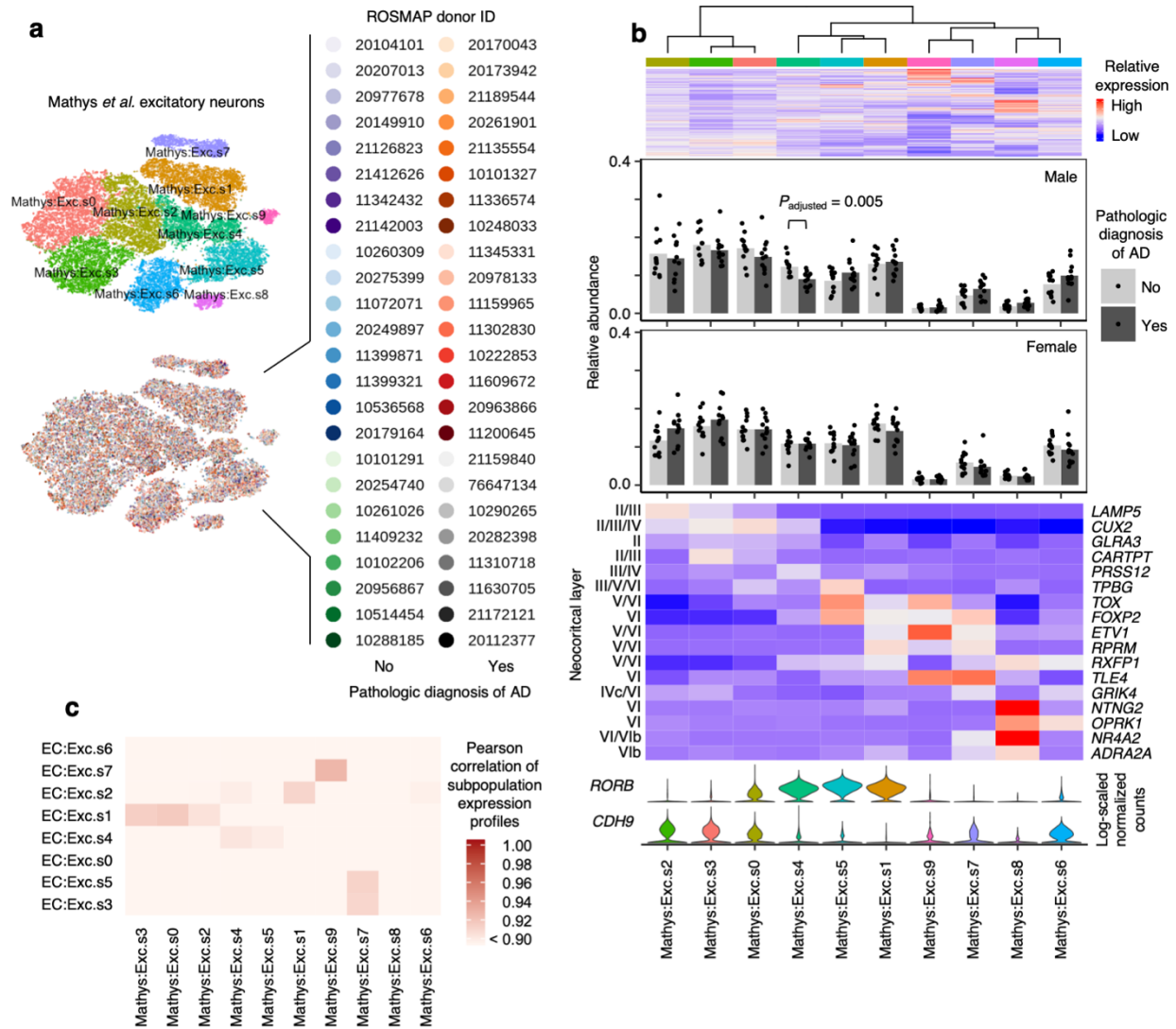
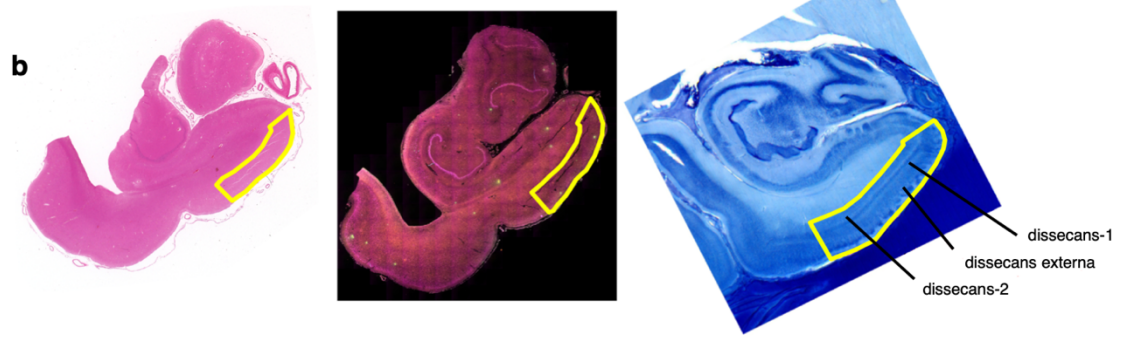
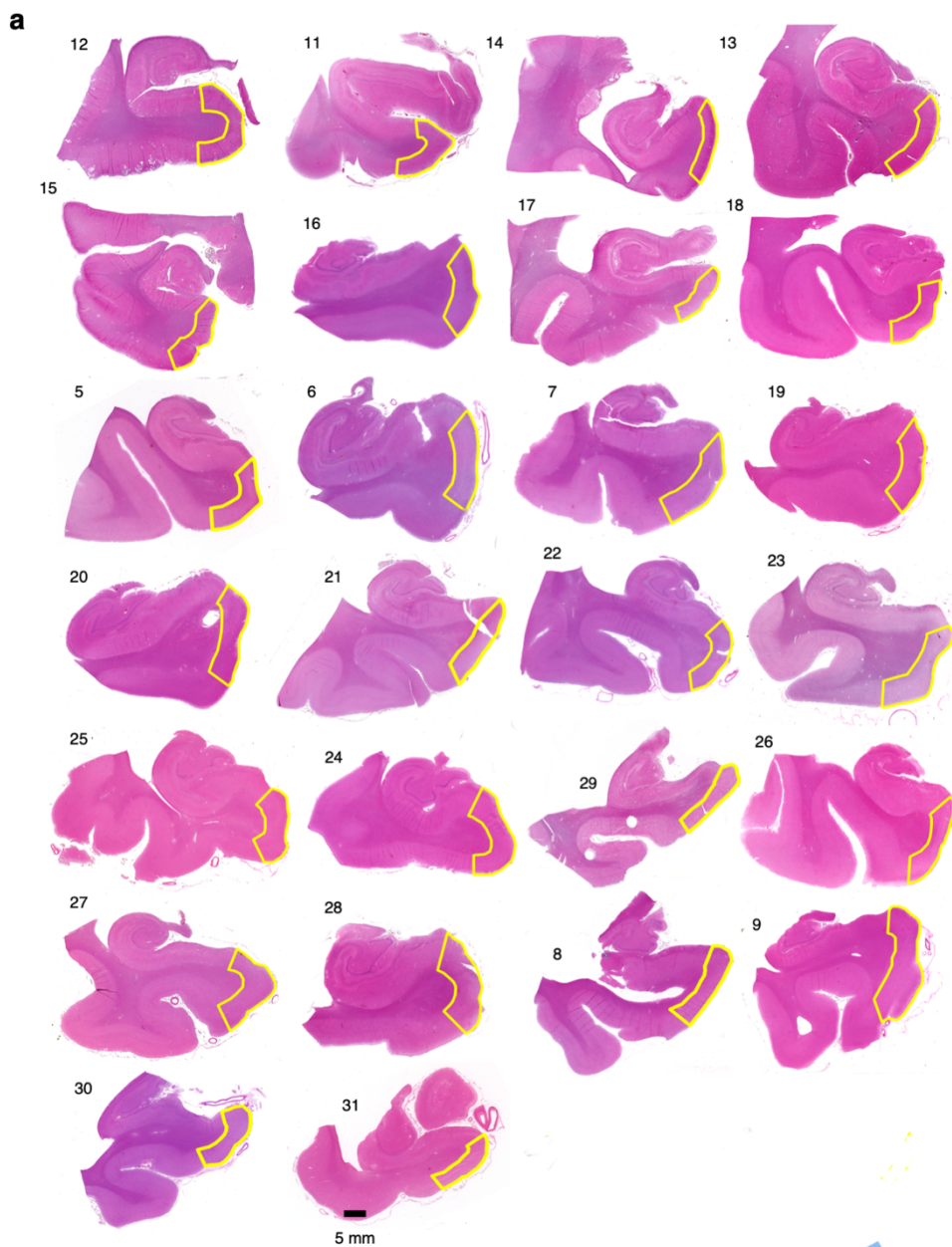


Fig. S2.5 | Cross-sample alignment of excitatory neurons from Mathys *et al.* recapitulates selective vulnerability in a RORB-expressing subpopulation. **a**, tSNE projection of excitatory neurons from Mathys *et al.*¹⁴ in the alignment space, colored by subpopulation identity (top) or individual of origin (bottom). **b**, Heatmap and hierarchical clustering of subpopulations and subpopulation marker expression (top subpanel); “High” and “Low” relative expression reflect above- and below-average expression, respectively (see Methods). Relative abundance of subpopulations in AD cases vs. controls, separated by sex (second and third subpanels); for each sex, statistical significance of differences in relative abundance between AD cases vs. controls (cases $n=12$, controls $n=12$, where n is the number of individuals sampled) was determined by beta regression and adjusted for multiple comparisons (see Methods). Expression heatmap of neocortical layer-specific genes from Lake *et al.*¹² (fourth subpanel). Expression of selectively vulnerable EC excitatory neuron subpopulation markers (bottom subpanel). **c**, Heatmap of Pearson correlation between the gene expression profiles of excitatory neuron subpopulations from the EC vs. those from the prefrontal cortex in Mathys *et al.*¹⁴



(Legend overleaf)

Fig. S2.6 | Delineation of the EC for each case used in immunofluorescence validation. a, The borders of the caudal EC delineated on sections stained with hematoxylin and eosin (H&E) for all 26 cases used in immunofluorescence validation (Table 2.1). **b,** Borders of the EC were determined with the aid of 400 um thick serial coronal sections of whole-brain hemispheres stained with gallocyanin (see Methods). Each H&E section (left) along with its corresponding immunofluorescence image (middle) was aligned to the most approximate gallocyanin section (right), in which the the dissecans layers (diss-1, diss-2, and diss-ext) characteristic of the caudal EC were easier to visualize. This was then used to guide delineation of the EC on the H&E and immunofluorescence sections. For more details on the cytoarchitectonic definitions used to define the caudal EC, please consult Heinsen *et al.*¹⁹.

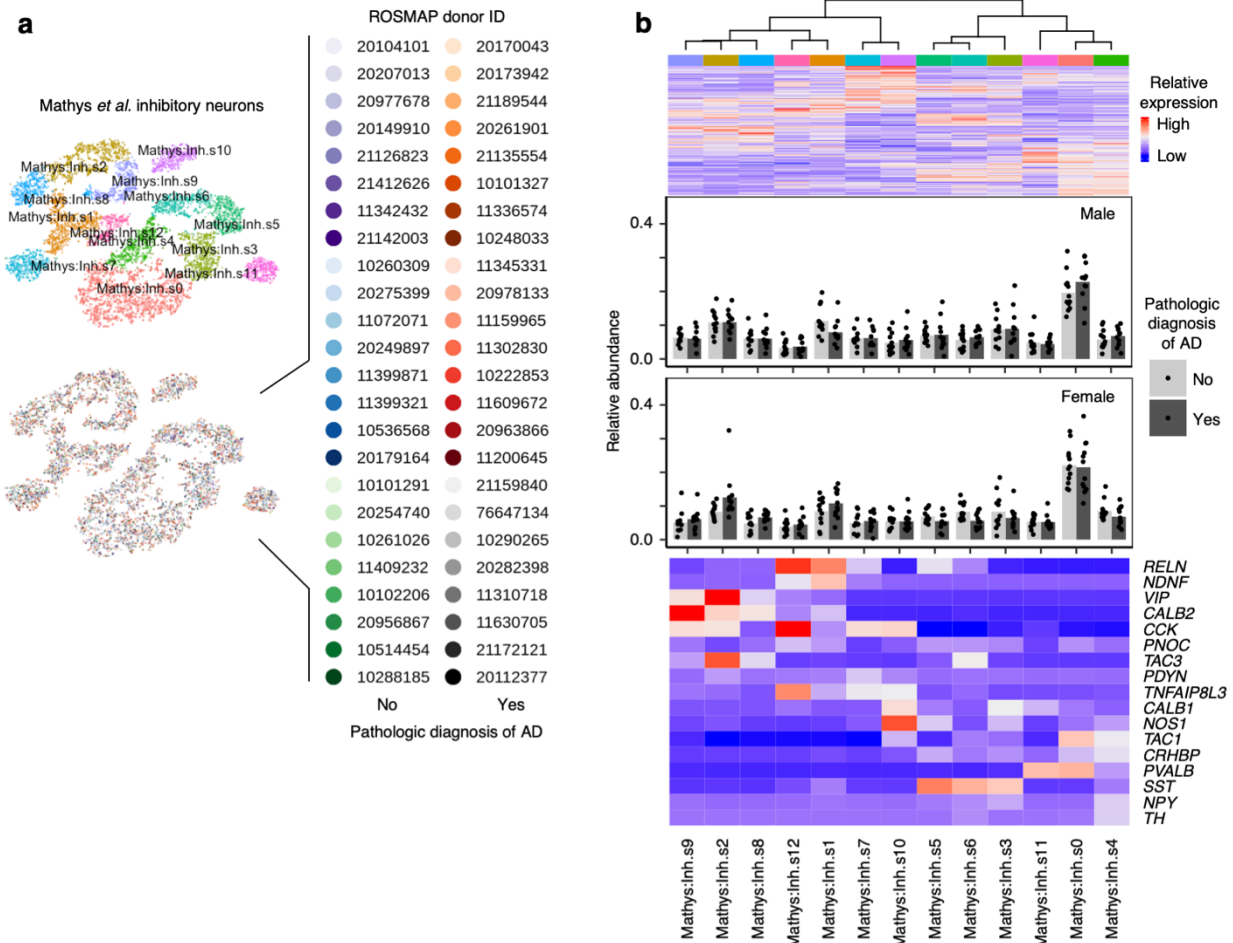
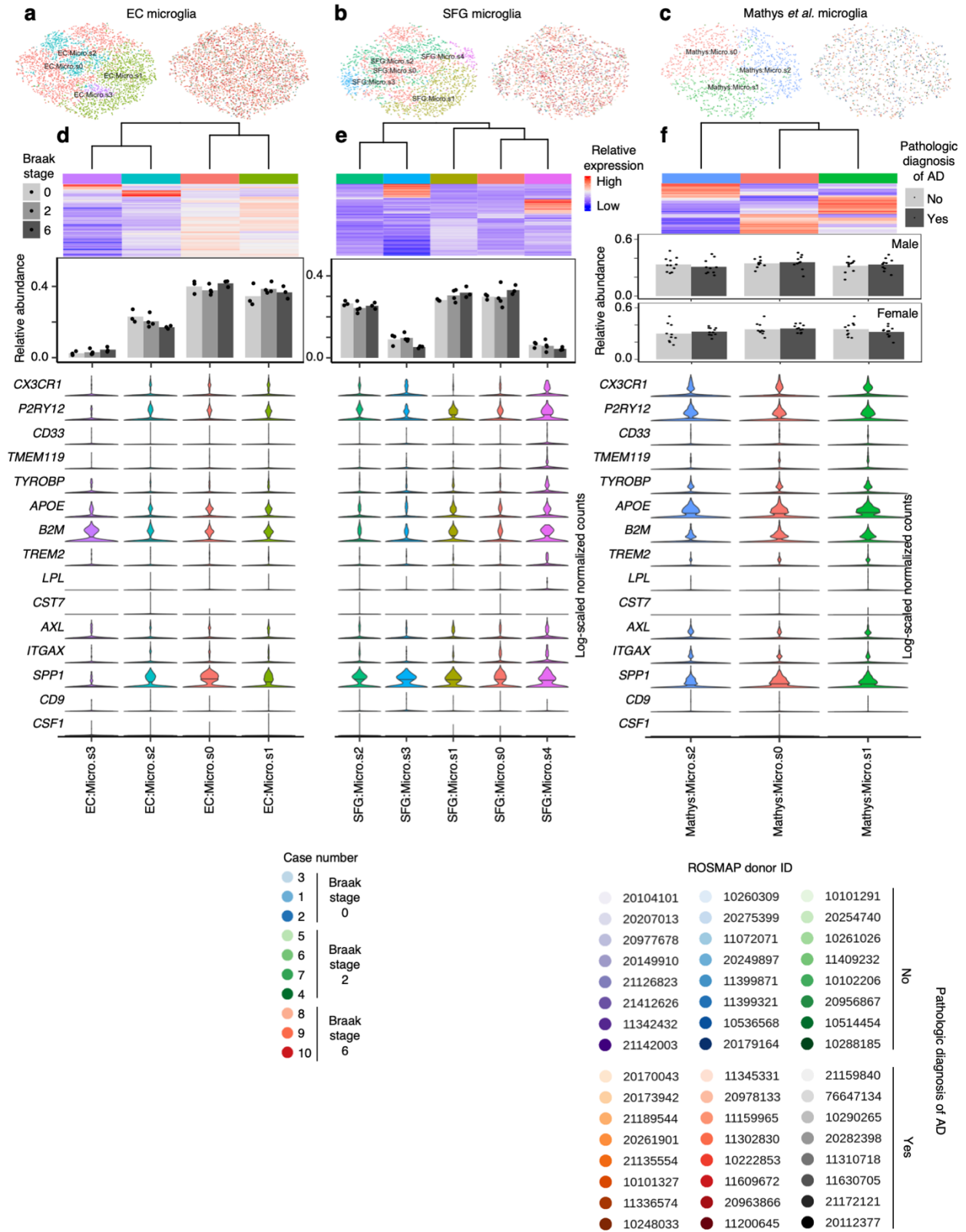


Fig. S2.7 | Inhibitory neurons from Mathys *et al.* also do not show differences in resilience or vulnerability to AD. **a**, tSNE projection of inhibitory neurons from Mathys *et al.*¹⁴ in the alignment space, colored by subpopulation identity (top) or individual of origin (bottom). **b**, Heatmap and hierarchical clustering of subpopulations and subpopulation markers (top subpanel); “High” and “Low” relative expression reflect above- and below-average expression, respectively (see Methods). Relative abundance of subpopulations in AD cases vs. controls, separated by sex (second and third subpanels); for each sex, statistical significance of differences in relative abundance between AD cases vs. controls (cases $n=12$, controls $n=12$, where n is the number of individuals sampled) was determined by beta regression and adjusted for multiple comparisons (see Methods). Expression heatmap of inhibitory neuron subtype markers from Lake *et al.*¹² (bottom subpanel).



(Legend overleaf)

Fig. S2.8 | Subclustering of microglia does not sufficiently resolve disease associated microglia signature. **a-c**, tSNE projection of astrocytes from the EC (**a**), SFG (**b**), and Mathys *et al.*¹⁴ (**c**) in their respective alignment spaces, colored by subpopulation identity (left) or individual of origin (right). **d-f**, Heatmap and hierarchical clustering of subpopulations and subpopulation marker expression (top subpanels); “High” and “Low” relative expression reflect above- and below-average expression, respectively (see Methods). Relative abundance of subpopulations (middle subpanels) across Braak stages in the EC and SFG (for each brain region, Braak 0 n=3, Braak 2 n=4, Braak 6 n=3, where n is the number of individuals sampled) or between AD cases vs. controls in Mathys *et al.*¹⁴ (for each sex, cases n =12, controls n = 12, where n is the number of individuals sampled); statistical significance of differences in relative abundance was determined by beta regression and adjusted for multiple comparisons (see Methods). Expression of disease associated microglia markers, with median expression level marked by line (bottom subpanels).

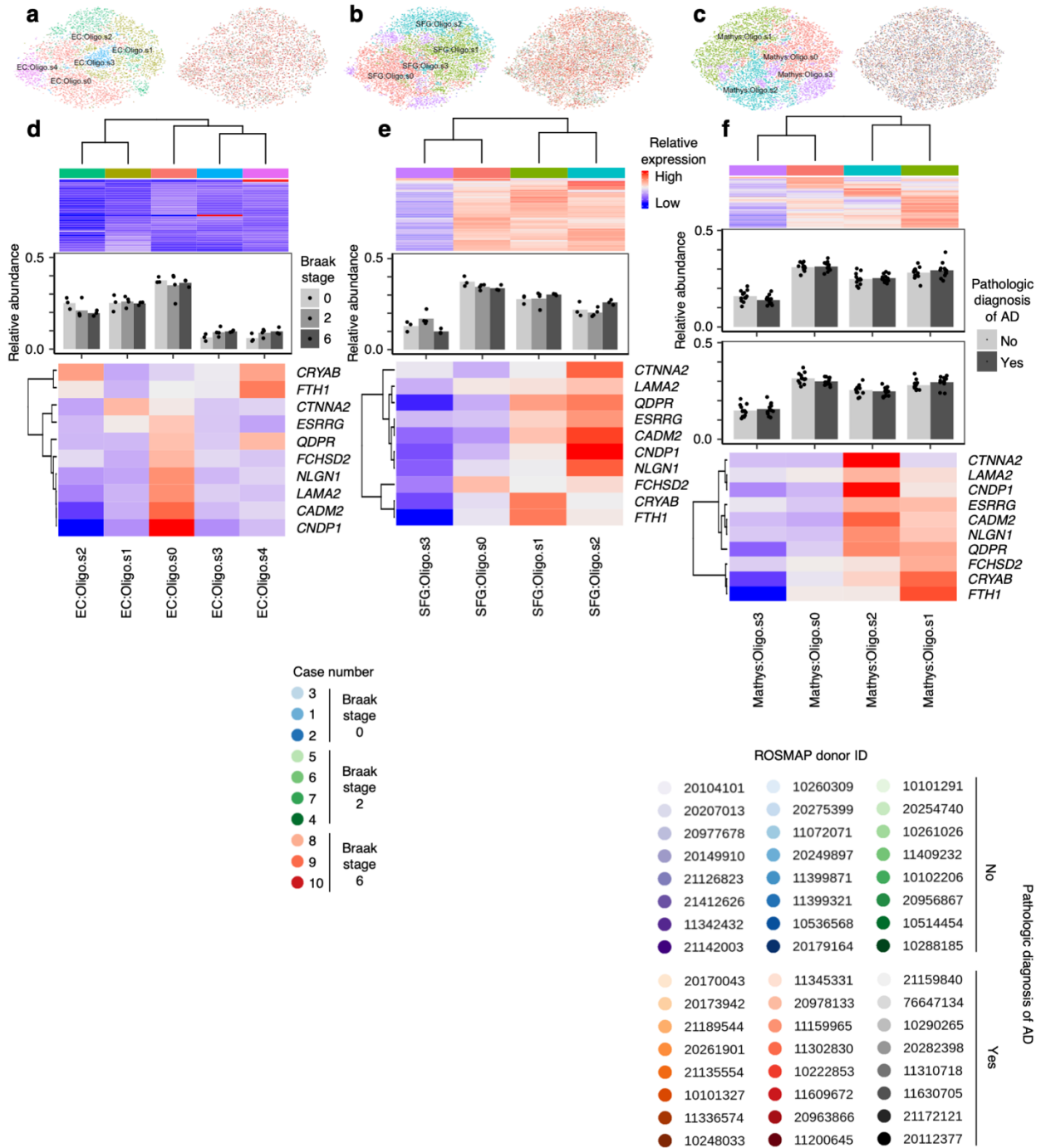


Fig. S2.9 | Subclustering of oligodendrocytes identifies subpopulations with higher expression of AD-associated oligodendrocyte markers from Mathys *et al.* a-c, tSNE projection of oligodendrocytes from the EC (a), SFG (b), and Mathys *et al.*¹⁴ (c) in their respective alignment spaces, colored by subpopulation identity (left) or individual of origin (right). d-f, Heatmap and hierarchical clustering of subpopulations and subpopulation marker expression (top subpanels); “High” and “Low” relative expression reflect above- and below-average expression, respectively (see Methods). Relative abundance of subpopulations (middle subpanels) across Braak stages in the EC and SFG (for each brain region, Braak 0 n=3, Braak 2 n=4, Braak 6 n=3, where n is the number of individuals sampled) or between AD cases vs.

controls in Mathys *et al.*¹⁴ (for each sex, cases n =12, controls n = 12, where n is the number of individuals sampled); statistical significance of differences in relative abundance was determined by beta regression and adjusted for multiple comparisons (see Methods). Relative expression of AD-associated oligodendrocyte subpopulation markers from Mathys *et al.*¹⁴ (bottom subpanels).

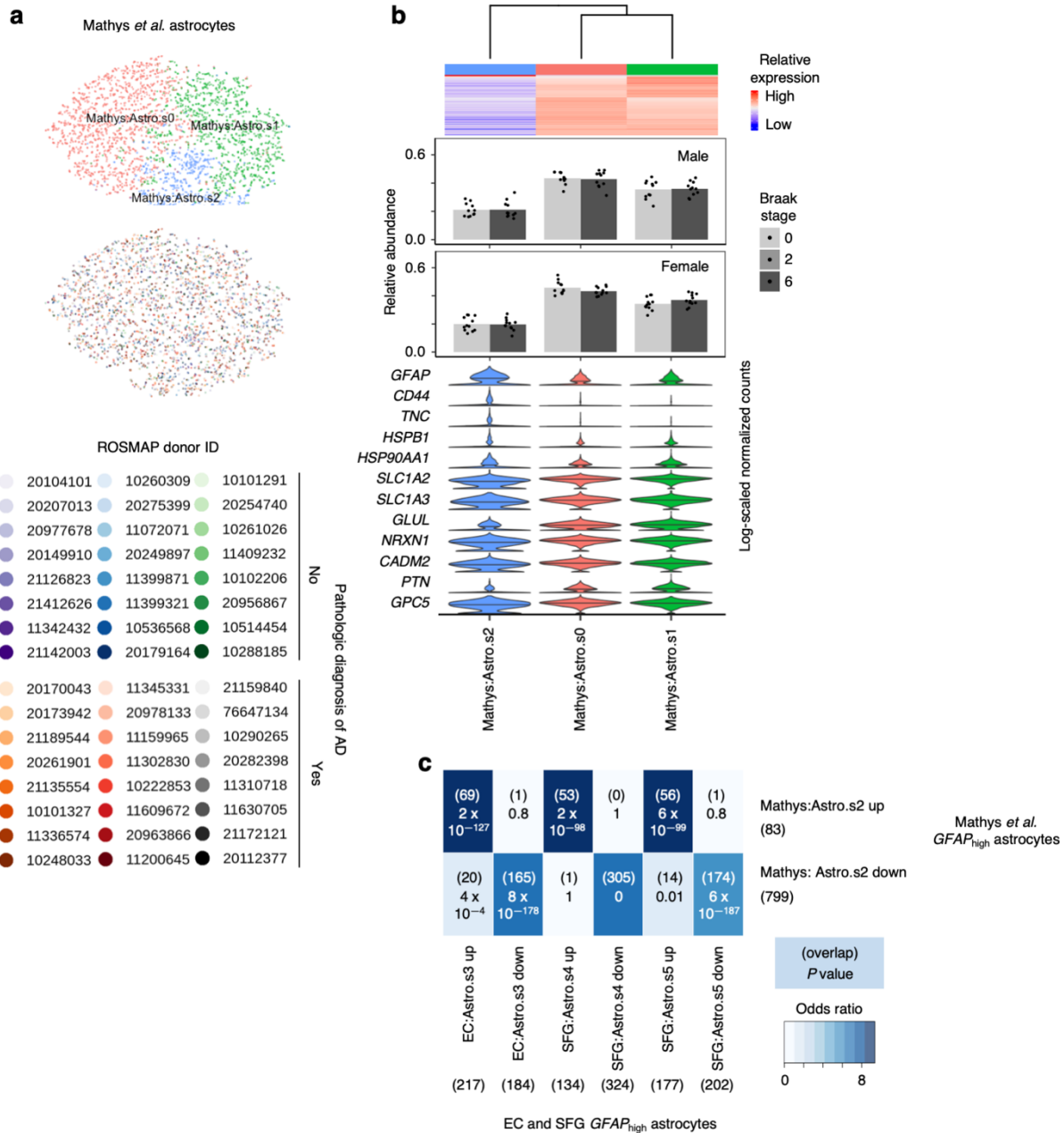


Fig. S2.10 | Astrocyte subpopulations with high GFAP expression from Mathys *et al.* are highly similar to those from the EC and SFG. **a**, tSNE projection of astrocytes from Mathys *et al.*¹⁴ in the alignment subspace, colored by subpopulation identity (top) or individual of origin (bottom). **b**, Heatmap and hierarchical clustering of subpopulations and subpopulation marker expression (top subpanel); “High” and “Low” relative expression reflect above- and below-average expression, respectively (see Methods). Relative abundance of subpopulations in AD cases vs. controls, separated by sex (middle subpanels); for each sex, statistical significance of differences in relative abundance between AD cases vs. controls (cases n=12, controls n=12, where n is the number of individuals sampled) was determined by beta regression and adjusted for multiple comparisons (see Methods). Expression of genes associated with reactive astrocytes, with median expression level marked by line (bottom subpanel). **c**, Enrichment analysis of overlap between differentially expressed genes in astrocytes with high GFAP

expression from Mathys *et al.*¹⁴ vs. differentially expressed genes in astrocytes with high GFAP expression from the EC and SFG; the number of genes in each gene set and the number of overlapping genes are shown in parentheses, and the hypergeometric test p-values are shown without parentheses.

METHODS

Post-mortem cohort

This study was approved by and University of Sao Paulo institutional review board and deemed non-human subject research by the University of California, San Francisco (UCSF). De-identified human postmortem brain tissue was supplied by the Neurodegenerative Disease Brain Bank (NDBB) at UCSF, and the Brazilian BioBank for Aging Studies (BBAS) from the University of Sao Paulo⁵⁰. The NDBB receives brain donations from patients enrolled in the UCSF Memory and Aging Center research programs. The BBAS is population-based and houses a high percentage of pathologically and clinically normal control subjects who are not available in the NDBB. Neuropathological assessments were performed using standardized protocols and followed internationally accepted criteria for neurodegenerative diseases⁵¹⁻⁵³. The brain samples used in this study contained a broad burden of AD-type pathology and were selected to be free from non-AD pathology including Lewy body disease, TDP-43 proteinopathies, primary tauopathies, and cerebrovascular changes. Argyrophilic grain disease (AGD) was not an exclusion criterion based on its high prevalence and lack of correlation with significant clinical symptoms⁵⁴⁻⁵⁶. In total, the cohort included 10 cases who underwent snRNA-seq, representing Braak stages 0, 2 and 6, all ApoE 3/3, and 26 cases who underwent neuroanatomical analysis, representing Braak stages 0-6^{1,57}, ranging from 2-5 individuals per Braak stage. Table 2.1 depicts the characteristics of the 31 cases.

Isolation of nuclei from frozen post-mortem human brain tissue

Isolation of nuclei was performed similarly as previously described⁵⁸. Briefly, frozen brain tissue was dounce homogenized in 5 ml of lysis buffer (0.25 M sucrose, 25 mM KCl, 5 mM MgCl₂, 20 mM Tricine-KOH, pH 7.8, 1 mM DTT, 0.15mM spermine, 0.5 mM spermidine, 1X protease inhibitor (Sigma, 4693159001), and RNase Inhibitor (Promega, N2615)). Following initial dounce homogenization, IGEPAL-630 was added to a final concentration of 0.3% and the

sample was homogenized with 5 more strokes. The solution was then filtered through a 40 um cell filter and mixed with Optiprep (Sigma, D1556-250ML) to create a 25% Optiprep solution. This solution was then layered onto a 30%/40% Optiprep gradient and centrifuged at 10,000g for 18 minutes using the SW41-Ti rotor. The nuclei were collected at the 30%/40% Optiprep interface.

Droplet-based single-nucleus RNA-sequencing

Droplet-based single-nucleus RNA-sequencing (snRNA-seq) was performed using the Chromium Single Cell 3' Reagent Kits v2 from 10X Genomics. Nuclei were resuspended to a concentration of 1000 nuclei/uL in 30% Optiprep solution before loading according to manufacturer's protocol, with 10,000 nuclei recovered per sample as the target. cDNA fragment analysis was performed using the Agilent 4200 TapeStation System. Sequencing parameters and quality control were performed as described by The Tabula Muris Consortium⁵⁹.

Pre-processing of snRNA-seq data

Sequencing data generated from snRNA-seq libraries were demultiplexed using *Cellranger* (version 2.1.0) *cellranger mkfastq*. To align reads, we first generated our own pre-mRNA GRCh38 reference genome using *cellranger mkref* in order to account for introns that may be eliminated using the default GRCh38 reference genome. Alignment and gene expression quantification was then performed using *cellranger count* with default settings.

Exploratory analysis of EC and SFG data

For each sample, the raw gene-barcode matrix outputted by *Cellranger* was converted into a *SingleCellExperiment* (SCE) object in R (version 3.5.1) using the *read10xCounts* function from the *DropletUtils* package⁶⁰ (version 1.2.2). Droplets containing nuclei were then distinguished from empty droplets using *DropletUtils::emptyDrops* with the parameter *FDR* =

0.01, and then nuclei (hereon also referred to as “cells”) with less than 200 UMIs were discarded. Afterwards, SCE objects corresponding to each sample were merged into a single SCE object for downstream processing and analyses.

For normalization of raw counts, to avoid artifacts caused by data sparsity, the approach of Lun *et al.*⁶¹ was adopted: For each sample, cells were first clustered using a graph-based method followed by pooling counts across cells in each cluster to obtain pool-based size factors, which were then deconvoluted to yield cell-based size factors. Clustering was performed using the *quickCluster* function from the *scran* package⁶² (version 1.10.2) with the parameters *method = 'igraph'*, *min.mean = 0.1*, *irlba.args = list(maxit = 1000)*, and the *block* parameter set to a character vector containing the sample identity of each cell. Size factors were computed using *scran::computeSumFactors* with the parameter *min.mean = 0.1* and the *cluster* parameter set to a character vector containing the cluster identity of each cell; cells with negative size factors were removed. Normalization followed by log-transformation was then performed using the *normalize* function from the *scater* package⁶³ (version 1.10.1).

Prior to dimensionality reduction, highly variable genes were identified for each sample separately using the approach of Lun *et al.*⁶²: Each gene’s variance was decomposed into a technical and biological component. Technical variance was assumed as Poisson and modeled using *scran::makeTechTrend*. The mean-variance trend across genes was fitted using *scran::trendVar* with parameters *use.spikes = FALSE* and *loess.args = list(span = 0.05)*; and the *trend* slot of the resulting fit object was then set to the output of *scran::makeTechTrend*. Biological variance was extracted from the total variance using *scran::decomposeVar* with the above fit object as the input. Finally, highly variable genes that were preserved across samples were identified by combining the variance decompositions with *scran::combineVar*, using Stouffer’s z-score method for meta-analysis (*method = 'z'*), which assigns more weight to samples with more cells.

For initial data exploration, genes with combined biological variance greater than 0 were used as the feature set for dimensionality reduction by principal component analysis using *scrani::parallelPCA*, which uses Horn's parallel analysis to decide how many principal components to retain, with parameter *approx = TRUE*. Clustering was then performed on the retained principal components using the *FindClusters* function from the *Seurat* package⁶⁴ (version 2.3.4) with parameter *resolution = 0.8*, which required conversion of SCE objects to Seurat objects using *Seurat::Convert*. To visualize the clusters, t-stochastic neighborhood embedding (tSNE) was performed on the retained principal components using *scater::runTSNE* with parameters *perplexity = 30* and *rand_seed = 100*.

Cross-sample alignment of SFG and EC data

Initial data exploration revealed that clustering was driven by individual of origin in addition to cell type identity, which makes it difficult to analyze changes in the relative abundance or gene expression of a given cell type across disease progression or brain regions. To recover clusters defined by mainly by cell type identity, data was aligned across samples from each brain region using with *scAlign*⁶⁵ (version 1.0.0), which leverages a neural network to learn a low-dimensional alignment space in which cells from different datasets group by biological function independent of technical and experimental factors. As noted by Johansen & Quon⁶⁵, *scAlign* converges faster with little loss of performance when the input data is represented by principal components or canonical correlation vectors. Therefore, prior to running *scAlign*, the top 2000 genes with the highest combined biological variance were used as the feature set for canonical correlation analysis (CCA), which was implemented using *Seurat::RunMultiCCA* with parameter *num.cc = 15*. The number of canonical coordinates to use for *scAlign* was determined by the elbow method using *Seurat::MetageneBicorPlot*. *scAlign* was then run on the cell loadings along the top 10 canonical correlation vectors with the parameters *options = scAlignOptions(steps = 10000, log.every = 5000, architecture = 'large', num.dim = 64)*,

encoder.data = 'cca', supervised = 'none', run.encoder = TRUE, run.decoder = FALSE, log.results = TRUE, and device = 'CPU'. Clustering was then performed on the full dimensionality of the output from *scAlign* using *Seurat::FindClusters* with parameter *resolution = 0.8* for the SFG and *resolution = 0.6* for the EC. Clusters were visualized with tSNE using *Seurat::RunTSNE* on the full dimensionality of the output from *scAlign* with parameter *do.fast = TRUE*. Alignment using *scAlign* followed by clustering was also performed for all samples from both brain regions jointly.

To assign clusters identified in the aligned subspace generated by *scAlign* to major brain cell types, the following marker genes were used: *SLC17A7* and *CAMK2A* for excitatory neurons, *GAD1* and *GAD2* for inhibitory neurons, *SLC1A2* and *AQP4* for astrocytes, *MBP* and *MOG* for oligodendrocytes, *PDGFRA* and *SOX10* for oligodendrocyte precursor cells (OPCs), *CD74* and *CX3CR1* for microglia/myeloid cells, and *CLDN5* and *FLT1* for endothelial cells. Clusters expressing markers for more than one cell type, most likely reflecting doublets, were removed from downstream analyses.

Cell type-specific subclustering (subpopulation) analysis

To identify cell type subpopulations, cells from all samples belonging to a given major cell type were extracted for sample-level re-computation of size factors and highly variable genes. CCA was then performed using the top 1000 genes with the highest combined biological variance as the feature set, followed by alignment of the first 10 to 12 canonical coordinates with *scAlign*, with *steps = 2500*. The full dimensionality of the output from *scAlign* was used for subclustering (using *resolution = 0.4*) and tSNE. Analyzing cells from each brain region separately, marker genes for subpopulations were identified using *scrn::findMarkers* with parameters *direction = 'up', pval.type = 'any', lfc = 0.58*, and the *block* parameter set to a character vector corresponding to each cell's sample identity. Subpopulations that expressed markers for more than one cell type were removed from downstream analyses.

Identification of differentially expressed genes in cell type subpopulations

To identify genes differentially expressed by a cell type subpopulation compared to all other subpopulations in a way that accounts for true biological replication (i.e. at the level of individuals), UMI counts of cells from the same individual belonging to the subpopulation of interest or all other subpopulations were summed to obtain “pseudo-bulk” samples, which were then analyzed using *edgeR*⁶⁶ (version 3.24.3) following the approach recommended by Amezcua *et al.*⁶⁷ A false-discovery rate cutoff of 0.1 was used.

Heatmap visualization of relative gene expression across cell types or cell type subpopulations

For heatmaps of relative gene expression across cell types or cell type subpopulations shown in the figures, log-scaled normalized counts of each gene were z-score transformed across all cells and then averaged across cells in each cluster to enhance visualization of differences among clusters. Thus genes with “high” relative expression have above-average expression (positive z-scores) and genes with “low” relative expression have below-average expression (negative z-scores).

Functional association network analysis and pathway enrichment analysis of differentially expressed genes

Differentially expressed genes were visualized as a functional association network using String-db⁶⁸ (v11), a protein-protein association network based on known physical interactions, functional associations, coexpression, and other metrics, and Cytoscape⁶⁹ (version 3.7.2), a network visualization software. When generating the networks, the String-db association confidence score cutoff set to 0.5, and the network layout was optimized for visualization using the yFiles Organic Layout. For pathway enrichment analysis, enrichments for Gene Ontology

terms and Reactome Pathways were also obtained through String-db, using a false-discovery rate cutoff of 0.05.

Entorhinal cortex layer-specific genes

Due to the lack of published data on layer-specific genes for the human EC, layer-specific genes in the mouse medial entorhinal cortex (MEC) were obtained from Ramsden *et al.*²². (The MEC is the most phylogenetically similar to the human caudal EC^{20, 21} used in this study.) Specifically, genes with expression specific for layer II, III, and V/VI of the mouse MEC according to the S4 Dataset excel spreadsheet in the supplemental information of Ramsden *et al.*²² were mapped to human genes, and cross-referenced against genes differentially expressed across EC excitatory neuron subclusters (obtained using *scran::findMarkers* without setting *direction = 'up'*).

Re-analysis of the Mathys *et al.* dataset

To re-analyze the data from Mathys *et al.*¹⁴ using our cross-sample alignment approach, the filtered matrix of UMI counts (“Data/Gene Expression (RNA-seq)/Processed/filtered_count_matrix.mtx”) and associated row and column metadata (“filtered_gene_row_names.txt” and “filtered_column_metadata.txt”) were downloaded from the AMP-AD Knowledge Portal (Synapse ID: syn18485175). The experimental and clinical metadata files were downloaded from “Data/Metadata”. The filtered UMI counts matrix and the associated row and column metadata were then converted to a *SingleCellExperiment* object for analysis, and the relevant experimental and clinical metadata (e.g. “Pathologic diagnosis of AD”) were merged with the *SingleCellExperiment* object. The cell type assignments from Mathys *et al.*¹⁴ provided in the column metadata were used for subclustering.

Functional annotation of differentially expressed genes in *GFAP*_{high} astrocytes

We obtained the functional annotation for differentially expressed genes from the GeneCards website⁷⁰ and verified the primary literature references for glutamate/GABA-related genes⁷¹⁻⁷⁶ and synaptic adhesion/maintenance-related genes⁷⁷⁻⁸⁰.

Quantitative histopathological assessment using multiplex immunofluorescence

Delineation of the caudal EC. We used archival paraffin blocks from the UCSF/NBDD and BBAS (Table 2.1). First, we collected blocks sampling the hippocampal formation anterior to the lateral genicular body from the 10 cases used for the snRNAseq and another 30 cases spanning all Braak stages¹. To determine if the caudal EC region was present, 8µm thick sections of each block underwent hematoxylin and eosin staining (Fig. S8A). We took digital images of the stained sections and aligned each one to the most approximate section from a large collection of 400 µm thick serial coronal sections of whole-brain hemispheres stained for gallocyanin provided by co-author Heinsen^{19, 81} (Extended Fig Data 8B). We eliminated blocks from five cases used for snRNA-seq and four of the extra cases for lack of caudal EC. Next, again with the aid of the paired gallocyanin sections, we delineated the borders of the caudal EC in each case (Fig. S8A).

The EC is considered a peri- or allocortex, depending on the author⁹. EC parcellation and cytoarchitectonic definitions have been a matter of debate, and here, we are adopting the cytoarchitectonic definitions proposed by Heinsen and colleagues¹⁹, which is based on the examination of thick histological preparations and considered the definitions proposed by Insausti and Amaral (6 layers)⁸² and Braak and Braak (3 layers)⁹. In thick histological sections, the caudal entorhinal region features well-delineated clusters of stellate or principal cells in layer II (pre-alpha clusters) and three lamina dissecans¹⁹. The external dissecans (dissecans-ext) divides layers II and III is particularly prominent in the caudal EC. Dissecans-1 (diss-1) corresponds to layer IV of Insausti⁸³ and the lamina dissecans of Braak and Braak⁹ and Rose⁸⁴. The most internal dissecans

(dissecans-2, or diss-2) is hardly appreciated in thin sections but easy to visualize in thick sections. It roughly corresponds to layer Vc of the caudal subregions of Insausti⁸³.

Multiplex immunofluorescence. Next, for each case, an 8µm thick, formalin-fixed and paraffin-embedded coronal section underwent immunofluorescence against TBR1, RORB and phospho-tau(CP-13) as described below. TBR1, or T-box, brain, 1 is a transcription factor protein that has a role in differentiation of glutamatergic neurons and is a marker for excitatory neurons, including EC excitatory neurons^{85, 86}. In summary, sections were deparaffinized and incubated in 3.0% hydrogen peroxide (Fisher, H325-500) in methanol to inactivate endogenous peroxidase. Antigen retrieval was performed in 1X Tris-EDTA HIER solution (TES500) PBS with 0.05% Tween 20 (PBS-T) at pH9 in an autoclave at 121 °C for five minutes. To reduce nonspecific background staining, sections were blocked with 5% Milk/PBS-T. To avoid cross-reactions between primary antibodies that were raised against the same species, an antibody stripping step using 0.80% β-mercaptoethanol/10% sodium dodecyl sulfate in 12.5% Tris-HCL was performed after the tyramide-signal amplification (TSA) development for RORB.

Sections were first incubated overnight in primary antibody against RORB (1:400, rabbit, HPA008393, Millipore Sigma), which was later developed in goat anti-rabbit HRP (1:400, R-05072-500, Advansta) with Alexa Fluor 488 TSA (1:100, B40953, Thermo Fisher). Next, sections were stripped of RORB primary antibody and then were incubated overnight in a cocktail of primary antibodies against TBR1 (1:100, Rabbit, ab31940, Abcam) and CP13 (1:800, mouse, phospho-tau serine 202, gift of Peter Davies, NY), all of which were later developed with secondary antibodies and fluorophores: for TBR1, Alexa Fluor 546 conjugated anti-rabbit secondary (1:200, A-11010, Thermo Fisher) was used, and for CP13, biotinylated anti-mouse (1:400, BA-2000, Vector Laboratory) with streptavidin Alexa Fluor 790 (1:250, S11378, Thermo Fisher) was used. Sections were then counterstained with DAPI diluted in PBS (1:5000, D1306, Invitrogen). Finally, sections were then incubated in Sudan Black B (199664-25g, Sigma) to

reduce autofluorescence and coverslipped using Prolong antifade mounting media (P36980, Invitrogen). A quality control slide was used to verify the efficacy of the antibody stripping process. A detailed description of the method is provided in Ehrenberg et al.²⁹ Sections were scanned using a Zeiss AxioScan Slide Scanner.

For generating the images shown in Fig. 2.3h, a section from case #6 (Braak stage 2, see Table 2.1) was stained with galloycyanin-chrome alum following standard methods¹⁹. The section was placed on a cover slip and scanned using a Zeiss AxioScan Slide Scanner. Next, the section was removed from the cover slip and underwent immunofluorescence for RORB and CP13 as described above. Then, the section was placed on a cover slip and scanned once more.

Neuronal quantification. The caudal EC delineations carried out in the hematoxylin and eosin-stained slides were then transferred to the immunostained images. Within these borders, we randomly placed four 500x500 µm regions of interest (ROI) overlaying the EC external layers (I to III), which we identified as being external to dissecans-1. We then extracted the ROIs for quantification in ImageJ (Fig. 2.3). The number of excitatory neurons was quantified by segmenting the TBR1 signal, using a threshold to create a mask and the segmentation editor plugin to manually remove all non-neuronal artifacts and vessels. The number of RORB+ excitatory neurons was then counted using the mask of excitatory (TBR1+) neurons in the segmentation editor and manually removing all neurons not expressing RORB. All segmentations were manually verified for quality control. Quantification was done blinded to the neuropathological diagnosis. We quantified phospho-tau (CP-13) staining in two ROIs in a subset of the cases, using the same FIJI protocol.

Statistical analysis

Beta regression. For each brain region, the relative abundance of a given cell cluster or cell type, which ranges from 0 to 1, was computed for each sample, treated as an independent measurement, and assumed to follow a beta distribution (although this was not formally tested). To determine the statistical significance of changes in the relative abundance of a given cluster or cell type across Braak stages, beta regression⁸⁷ was performed using the *betareg* package (version 3.1-1), using the formula *relative.abundance ~ braak.stage* for both the mean and precision models, and the bias-corrected maximum likelihood estimator (*type = 'BC'*). The statistical significance of changes in the proportion of TBR1+ cells and RORB+ cells among TBR1+ cells obtained from immunofluorescence validation were assessed similarly as above using beta regression. To correct for multiple hypothesis testing for each family of tests (e.g. testing all cell type subpopulations for a brain region), Holm's method was used to adjust *P* values obtained from beta regression to control the family-wise type I error rate at 0.05.

Fisher's exact test. For Fig. 2.3g, the two-sided Fisher's Exact Test was used to calculate the statistical significance of the observed enrichment of CP13 staining in RORB+ excitatory neurons. The test was performed in R using *fisher.test* with *alternative='two-sided'*.

Hypergeometric test. For Fig. 2.5e and Fig. S2.10c, the one-sided hypergeometric test (implemented in R with the package *GeneOverlap*, version 1.18.0) was used to calculate the statistical significance of the observed gene overlaps. The *P* values were adjusted for multiple testing using the Benjamini-Hochberg method.

Randomization. Data collection for the snRNA-seq or immunostaining validation was not randomized or blocked.

Sample sizes. No statistical methods were used to pre-determine sample sizes but our sample sizes are comparable to those reported in previous publications^{14, 15}.

REFERENCES

1. Braak, H. & Braak, E. Neuropathological staging of Alzheimer-related changes. *Acta Neuropathol* **82**, 239-259 (1991).
2. Scholl, M., *et al.* PET Imaging of Tau Deposition in the Aging Human Brain. *Neuron* **89**, 971-982 (2016).
3. Seeley, W.W., Crawford, R.K., Zhou, J., Miller, B.L. & Greicius, M.D. Neurodegenerative diseases target large-scale human brain networks. *Neuron* **62**, 42-52 (2009).
4. Braak, H. & Braak, E. Staging of Alzheimer's disease-related neurofibrillary changes. *Neurobiol Aging* **16**, 271-278; discussion 278-284 (1995).
5. Price, J.L., *et al.* Neuron number in the entorhinal cortex and CA1 in preclinical Alzheimer disease. *Arch Neurol* **58**, 1395-1402 (2001).
6. Stranahan, A.M. & Mattson, M.P. Selective vulnerability of neurons in layer II of the entorhinal cortex during aging and Alzheimer's disease. *Neural Plast* **2010**, 108190 (2010).
7. Van Hoesen, G.W., Hyman, B.T. & Damasio, A.R. Entorhinal cortex pathology in Alzheimer's disease. *Hippocampus* **1**, 1-8 (1991).
8. Gomez-Isla, T., *et al.* Profound loss of layer II entorhinal cortex neurons occurs in very mild Alzheimer's disease. *J Neurosci* **16**, 4491-4500 (1996).
9. Braak, H. & Braak, E. The human entorhinal cortex: normal morphology and lamina-specific pathology in various diseases. *Neurosci Res* **15**, 6-31 (1992).
10. Kordower, J.H., *et al.* Loss and atrophy of layer II entorhinal cortex neurons in elderly people with mild cognitive impairment. *Ann Neurol* **49**, 202-213 (2001).

11. Drummond, E. & Wisniewski, T. Alzheimer's disease: experimental models and reality. *Acta Neuropathol* **133**, 155-175 (2017).
12. Lake, B.B., *et al.* Neuronal subtypes and diversity revealed by single-nucleus RNA sequencing of the human brain. *Science* **352**, 1586-1590 (2016).
13. Hodge, R.D., *et al.* Conserved cell types with divergent features in human versus mouse cortex. *Nature* **573**, 61-68 (2019).
14. Mathys, H., *et al.* Single-cell transcriptomic analysis of Alzheimer's disease. *Nature* **570**, 332-337 (2019).
15. Grubman, A., *et al.* A single-cell atlas of entorhinal cortex from individuals with Alzheimer's disease reveals cell-type-specific gene expression regulation. *Nature neuroscience* **22**, 2087-2097 (2019).
16. Nelson, P.T., *et al.* Correlation of Alzheimer disease neuropathologic changes with cognitive status: a review of the literature. *J Neuropathol Exp Neurol* **71**, 362-381 (2012).
17. Hof, P.R., *et al.* Parvalbumin-immunoreactive neurons in the neocortex are resistant to degeneration in Alzheimer's disease. *J Neuropathol Exp Neurol* **50**, 451-462 (1991).
18. Fu, H., *et al.* A tau homeostasis signature is linked with the cellular and regional vulnerability of excitatory neurons to tau pathology. *Nature neuroscience* **22**, 47-56 (2019).
19. Heinsen, H., *et al.* Quantitative investigations on the human entorhinal area: left-right asymmetry and age-related changes. *Anat Embryol (Berl)* **190**, 181-194 (1994).
20. Kobre-Flatmoen, A. & Witter, M.P. Neuronal chemo-architecture of the entorhinal cortex: A comparative review. *Eur J Neurosci* **50**, 3627-3662 (2019).

21. Naumann, R.K., *et al.* Conserved size and periodicity of pyramidal patches in layer 2 of medial/caudal entorhinal cortex. *J Comp Neurol* **524**, 783-806 (2016).
22. Ramsden, H.L., Surmeli, G., McDonagh, S.G. & Nolan, M.F. Laminar and dorsoventral molecular organization of the medial entorhinal cortex revealed by large-scale anatomical analysis of gene expression. *PLoS Comput Biol* **11**, e1004032 (2015).
23. Jabaudon, D., Shnyder, S.J., Tischfield, D.J., Galazo, M.J. & Macklis, J.D. RORbeta induces barrel-like neuronal clusters in the developing neocortex. *Cereb Cortex* **22**, 996-1006 (2012).
24. Oishi, K., Aramaki, M. & Nakajima, K. Mutually repressive interaction between Brn1/2 and Rorb contributes to the establishment of neocortical layer 2/3 and layer 4. *Proceedings of the National Academy of Sciences of the United States of America* **113**, 3371-3376 (2016).
25. Nakagawa, Y. & O'Leary, D.D. Dynamic patterned expression of orphan nuclear receptor genes RORalpha and RORbeta in developing mouse forebrain. *Dev Neurosci* **25**, 234-244 (2003).
26. Marinaro, F., *et al.* Molecular and cellular pathology of monogenic Alzheimer's disease at single cell resolution. *bioRxiv*, 2020.2007.2014.202317 (2020).
27. Liang, W.S., *et al.* Altered neuronal gene expression in brain regions differentially affected by Alzheimer's disease: a reference data set. *Physiol Genomics* **33**, 240-256 (2008).
28. Franjic, D., *et al.* Molecular Diversity Among Adult Human Hippocampal and Entorhinal Cells. *bioRxiv* doi: <https://doi.org/10.1101/2019.12.31.889139> (2019).

29. Ehrenberg, A.J., *et al.* A manual multiplex immunofluorescence method for investigating neurodegenerative diseases. *Journal of Neuroscience Methods* **In press**, <https://doi.org/10.1016/j.jneumeth.2020.108708>. (2020).
30. Keren-Shaul, H., *et al.* A Unique Microglia Type Associated with Restricting Development of Alzheimer's Disease. *Cell* **169**, 1276-1290 e1217 (2017).
31. Srinivasan, K., *et al.* Alzheimer's patient brain myeloid cells exhibit enhanced aging and unique transcriptional activation. *bioRxiv* doi: <https://doi.org/10.1101/610345> (2019).
32. Thrupp, N., *et al.* Single nucleus sequencing fails to detect microglial activation in human tissue. *bioRxiv*, 2020.2004.2013.035386 (2020).
33. Chen, W.T., *et al.* Spatial Transcriptomics and In Situ Sequencing to Study Alzheimer's Disease. *Cell* (2020).
34. Perez-Nievas, B.G. & Serrano-Pozo, A. Deciphering the Astrocyte Reaction in Alzheimer's Disease. *Front Aging Neurosci* **10**, 114 (2018).
35. Simpson, J.E., *et al.* Microarray analysis of the astrocyte transcriptome in the aging brain: relationship to Alzheimer's pathology and APOE genotype. *Neurobiol Aging* **32**, 1795-1807 (2011).
36. Sekar, S., *et al.* Alzheimer's disease is associated with altered expression of genes involved in immune response and mitochondrial processes in astrocytes. *Neurobiol Aging* **36**, 583-591 (2015).
37. Liddel, S.A., *et al.* Neurotoxic reactive astrocytes are induced by activated microglia. *Nature* **541**, 481-487 (2017).

38. Laywell, E.D., *et al.* Enhanced expression of the developmentally regulated extracellular matrix molecule tenascin following adult brain injury. *Proceedings of the National Academy of Sciences of the United States of America* **89**, 2634-2638 (1992).
39. Zamanian, J.L., *et al.* Genomic analysis of reactive astrogliosis. *J Neurosci* **32**, 6391-6410 (2012).
40. Anderson, M.A., *et al.* Astrocyte scar formation aids central nervous system axon regeneration. *Nature* **532**, 195-200 (2016).
41. Kampmann, M. A CRISPR Approach to Neurodegenerative Diseases. *Trends in molecular medicine* **23**, 483-485 (2017).
42. Kampmann, M. CRISPR-based functional genomics for neurological disease. *Nat Rev Neurol* (2020).
43. Tian, R., *et al.* CRISPR Interference-Based Platform for Multimodal Genetic Screens in Human iPSC-Derived Neurons. *Neuron* **104**, 239-255 e212 (2019).
44. Hof, P.R. & Morrison, J.H. Neocortical neuronal subpopulations labeled by a monoclonal antibody to calbindin exhibit differential vulnerability in Alzheimer's disease. *Exp Neurol* **111**, 293-301 (1991).
45. Hof, P.R., Cox, K. & Morrison, J.H. Quantitative analysis of a vulnerable subset of pyramidal neurons in Alzheimer's disease: I. Superior frontal and inferior temporal cortex. *J Comp Neurol* **301**, 44-54 (1990).
46. Mikkonen, M., Alafuzoff, I., Tapiola, T., Soininen, H. & Miettinen, R. Subfield- and layer-specific changes in parvalbumin, calretinin and calbindin-D28K immunoreactivity in the entorhinal cortex in Alzheimer's disease. *Neuroscience* **92**, 515-532 (1999).

47. Tian, R., *et al.* CRISPR Interference-Based Platform for Multimodal Genetic Screens in Human iPSC-Derived Neurons. *Neuron* **104**, 239–255 (2019).
48. Montine, T.J., *et al.* National Institute on Aging-Alzheimer's Association guidelines for the neuropathologic assessment of Alzheimer's disease: a practical approach. *Acta Neuropathol* **123**, 1-11 (2012).
49. Hughes, C.P., Berg, L., Danziger, W.L., Coben, L.A. & Martin, R.L. A new clinical scale for the staging of dementia. *Br J Psychiatry* **140**, 566-572 (1982).
50. Grinberg, L.T., *et al.* Brain bank of the Brazilian aging brain study group - a milestone reached and more than 1,600 collected brains. *Cell Tissue Bank* **8**, 151-162 (2007).
51. Hyman, B.T., *et al.* National Institute on Aging-Alzheimer's Association guidelines for the neuropathologic assessment of Alzheimer's disease. *Alzheimers Dement* **8**, 1-13 (2012).
52. Suemoto, C.K., *et al.* Neuropathological diagnoses and clinical correlates in older adults in Brazil: A cross-sectional study. *PLoS Med* **14**, e1002267 (2017).
53. Cairns, N.J., *et al.* Neuropathologic diagnostic and nosologic criteria for frontotemporal lobar degeneration: consensus of the Consortium for Frontotemporal Lobar Degeneration. *Acta Neuropathol* **114**, 5-22 (2007).
54. Ferrer, I., Santpere, G. & van Leeuwen, F.W. Argyrophilic grain disease. *Brain* **131**, 1416-1432 (2008).
55. Rodriguez, R.D. & Grinberg, L.T. Argyrophilic grain disease: An underestimated tauopathy. *Dement Neuropsychol* **9**, 2-8 (2015).

56. Rodriguez, R.D., *et al.* Argrophilic Grain Disease: Demographics, Clinical, and Neuropathological Features From a Large Autopsy Study. *J Neuropathol Exp Neurol* **75**, 628-635 (2016).
57. Braak, H., Thal, D.R., Ghebremedhin, E. & Del Tredici, K. Stages of the pathologic process in Alzheimer disease: age categories from 1 to 100 years. *J Neuropathol Exp Neurol* **70**, 960-969 (2011).
58. Mo, A., *et al.* Epigenomic Signatures of Neuronal Diversity in the Mammalian Brain. *Neuron* **86**, 1369-1384 (2015).
59. Tabula Muris, C., *et al.* Single-cell transcriptomics of 20 mouse organs creates a Tabula Muris. *Nature* **562**, 367-372 (2018).
60. Lun, A.T.L., *et al.* EmptyDrops: distinguishing cells from empty droplets in droplet-based single-cell RNA sequencing data. *Genome biology* **20**, 63 (2019).
61. Lun, A.T., Bach, K. & Marioni, J.C. Pooling across cells to normalize single-cell RNA sequencing data with many zero counts. *Genome biology* **17**, 75 (2016).
62. Lun, A.T., McCarthy, D.J. & Marioni, J.C. A step-by-step workflow for low-level analysis of single-cell RNA-seq data with Bioconductor. *F1000Res* **5**, 2122 (2016).
63. McCarthy, D.J., Campbell, K.R., Lun, A.T. & Wills, Q.F. Scater: pre-processing, quality control, normalization and visualization of single-cell RNA-seq data in R. *Bioinformatics* **33**, 1179-1186 (2017).
64. Stuart, T., *et al.* Comprehensive Integration of Single-Cell Data. *Cell* **177**, 1888-1902 e1821 (2019).

65. Johansen, N. & Quon, G. scAlign: a tool for alignment, integration, and rare cell identification from scRNA-seq data. *Genome biology* **20**, 166 (2019).
66. Robinson, M.D., McCarthy, D.J. & Smyth, G.K. edgeR: a Bioconductor package for differential expression analysis of digital gene expression data. *Bioinformatics* **26**, 139-140 (2010).
67. Amezquita, R.A., *et al.* Orchestrating single-cell analysis with Bioconductor. *Nat Methods* **17**, 137-145 (2020).
68. Szklarczyk, D., *et al.* STRING v11: protein-protein association networks with increased coverage, supporting functional discovery in genome-wide experimental datasets. *Nucleic acids research* **47**, D607-D613 (2019).
69. Shannon, P., *et al.* Cytoscape: a software environment for integrated models of biomolecular interaction networks. *Genome Res* **13**, 2498-2504 (2003).
70. Stelzer, G., *et al.* The GeneCards Suite: From Gene Data Mining to Disease Genome Sequence Analyses. *Curr Protoc Bioinformatics* **54**, 1 30 31-31 30 33 (2016).
71. Arriza, J.L., *et al.* Functional comparisons of three glutamate transporter subtypes cloned from human motor cortex. *J Neurosci* **14**, 5559-5569 (1994).
72. Borden, L.A., *et al.* Cloning of the human homologue of the GABA transporter GAT-3 and identification of a novel inhibitor with selectivity for this site. *Receptors Channels* **2**, 207-213 (1994).
73. Gendreau, S., *et al.* A trimeric quaternary structure is conserved in bacterial and human glutamate transporters. *J Biol Chem* **279**, 39505-39512 (2004).

74. Häberle, J., *et al.* Congenital glutamine deficiency with glutamine synthetase mutations. *N Engl J Med* **353**, 1926-1933 (2005).
75. Kawakami, H., Tanaka, K., Nakayama, T., Inoue, K. & Nakamura, S. Cloning and expression of a human glutamate transporter. *Biochem Biophys Res Commun* **199**, 171-176 (1994).
76. Melzer, N., Biela, A. & Fahlke, C. Glutamate modifies ion conduction and voltage-dependent gating of excitatory amino acid transporter-associated anion channels. *J Biol Chem* **278**, 50112-50119 (2003).
77. Südhof, T.C. Synaptic Neurexin Complexes: A Molecular Code for the Logic of Neural Circuits. *Cell* **171**, 745-769 (2017).
78. Pellissier, F., Gerber, A., Bauer, C., Ballivet, M. & Ossipow, V. The adhesion molecule Necl-3/SynCAM-2 localizes to myelinated axons, binds to oligodendrocytes and promotes cell adhesion. *BMC Neurosci* **8**, 90 (2007).
79. González-Castillo, C., Ortuño-Sahagún, D., Guzmán-Brambila, C., Pallàs, M. & Rojas-Mayorquín, A.E. Pleiotrophin as a central nervous system neuromodulator, evidences from the hippocampus. *Front Cell Neurosci* **8**, 443 (2014).
80. Siddiqui, T.J., *et al.* An LRRTM4-HSPG complex mediates excitatory synapse development on dentate gyrus granule cells. *Neuron* **79**, 680-695 (2013).
81. Heinsen, H., Arzberger, T. & Schmitz, C. Celloidin mounting (embedding without infiltration) - a new, simple and reliable method for producing serial sections of high thickness through complete human brains and its application to stereological and immunohistochemical investigations. *J Chem Neuroanat* **20**, 49-59 (2000).

82. Insausti, R. & Amaral, D.G. Entorhinal cortex of the monkey: IV. Topographical and laminar organization of cortical afferents. *J Comp Neurol* **509**, 608-641 (2008).
83. Insausti, R., Munoz-Lopez, M., Insausti, A.M. & Artacho-Perula, E. The Human Periallocortex: Layer Pattern in Presubiculum, Parasubiculum and Entorhinal Cortex. A Review. *Front Neuroanat* **11**, 84 (2017).
84. Rose, S. Vergleichende Messungen im Allocortex bei Tier und Mensch. *J Psychol Neurol* **34**, 250-255 (1927).
85. Fu, H., *et al.* Tau Pathology Induces Excitatory Neuron Loss, Grid Cell Dysfunction, and Spatial Memory Deficits Reminiscent of Early Alzheimer's Disease. *Neuron* **93**, 533-541 e535 (2017).
86. Hevner, R.F., *et al.* Tbr1 regulates differentiation of the preplate and layer 6. *Neuron* **29**, 353-366 (2001).
87. Ferrari, S.L.P. & Cribari-Neto, F. Beta regression for modelling rates and proportions. *J Appl Stat* **31**, 799-815 (2004).

CHAPTER 3

CRISPRi screens in human astrocytes elucidate regulators of distinct inflammatory reactive states

This chapter is a manuscript in submission and is reproduced from the following preprint:

Leng, K., Rooney, B., Kim, H., Xia, W., Koontz, M., Krawczyk, M., Zhang Y., Ullian E.M., Fancy S.P.J., Schrag M.S., Lippman E.S. & Kampmann, M. (2021). CRISPRi screens in human astrocytes elucidate regulators of distinct inflammatory reactive states. *bioRxiv*. <https://doi.org/10.1101/2021.08.23.457400>

ABSTRACT

In response to central nervous system injury or disease, astrocytes become reactive, adopting context-dependent states with altered functions. Certain inflammatory insults induce reactive astrocyte states that lose homeostatic functions and gain harmful outputs, and likely contribute to neuroinflammatory and neurodegenerative diseases. However, the cellular pathways controlling these states are not fully understood. Here, we combined single-cell transcriptomics with CRISPRi screening in human iPSC-derived astrocytes to systematically interrogate inflammatory reactivity. We found that autocrine-paracrine IL-6 and interferon signaling downstream of canonical NF- κ B activation drove two distinct inflammatory reactive states promoted by and inhibited by STAT3, respectively. Furthermore, these states corresponded with those observed in other experimental contexts, including *in vivo*, and their markers were upregulated in the human brain in Alzheimer's disease and hypoxic ischemic encephalopathy. These results and the platform we established have the potential to guide the development of therapeutics to selectively modulate different aspects of inflammatory astrocyte reactivity.

INTRODUCTION

Astrocytes perform critical homeostatic functions in the central nervous system (CNS), such as providing trophic support for neurons, regulating the formation and function of synapses, and maintaining the blood–brain barrier¹. In CNS injury or disease, astrocytes respond to pathophysiological perturbations by becoming “reactive”, which is defined as the adoption of context-specific cell states and associated alterations in morphology and function^{1,2}.

Frequently, inflammatory processes play an important, if not central, role in the pathophysiology of CNS injuries, as seen in stroke³ and trauma⁴, and diseases such as multiple sclerosis⁵ and Alzheimer's disease⁶. As an immunocompetent CNS cell type, astrocytes actively participate in inflammatory signaling cascades and interact with both microglia, the CNS

resident immune cells, as well as infiltrating immune cells from the periphery^{6,7}. Proinflammatory cytokines, such as IL-1 α , TNF, and C1q, induce reactive astrocytes that lose homeostatic functions while concurrently releasing factors that are potentially harmful in specific contexts⁸⁻¹⁰. From here on, we will refer to this form of astrocyte reactivity as “inflammatory reactivity”.

Given that inflammatory astrocyte reactivity has been implicated in numerous neurodegenerative and neuroinflammatory diseases^{8,11}, in addition to being associated with normal aging¹², it is an attractive target for therapeutic development. However, the cellular pathways that control inflammatory astrocyte reactivity are still not fully understood, partly due to limitations in experimental scalability. On the one hand, animal models have provided key insights into genes required for astrocyte reactivity^{9,13,14}, but the throughput to test genetic perturbations *in vivo* is extremely limited. On the other hand, *in vitro* astrocyte culture is a powerful alternative, but the scalability of experiments is still limited by the necessity to isolate primary astrocytes or the long duration of the differentiation process (up to 6 months) required to generate mature, non-reactive human iPSC (hiPSC)-derived astrocytes¹⁵. Lastly, even though “omics” assays such as RNA-seq have been used extensively to identify cellular pathways altered in inflammatory reactive astrocytes^{9,16}, these assays by themselves can only provide correlative information and cannot uncover causal pathways controlling inflammatory reactivity.

Here, we developed a scalable method to generate hiPSC-derived astrocytes that allowed us to harness the power of pooled CRISPRi screening¹⁷ to systematically identify cellular pathways controlling inflammatory astrocyte reactivity. Following up on the top hits from CRISPRi screens with single-cell transcriptomics, we found that autocrine-paracrine IL-6 and interferon signaling drove two distinct inflammatory reactive states that were promoted by and inhibited by STAT3, respectively. Furthermore, we found that the inflammatory reactive states we identified corresponded to those observed in other experimental contexts, both *in vitro* and *in vivo*. Lastly, we also performed immunostaining supporting the existence of these inflammatory

reactive states in human brains in the context of Alzheimer's disease and hypoxic-ischemic encephalopathy.

RESULTS

iPSC-derived astrocytes (iAstrocytes) perform canonical astrocyte functions and sufficiently model inflammatory reactivity

To generate hiPSC-derived astrocytes in a scalable manner, we modified the protocol from TCW *et al.*¹⁸ by inducing the expression of the gliogenic transcription factors NFIA and SOX9¹⁹ during the differentiation process (see Methods). Our protocol resulted in astrocytes, which we will here on refer to as “iAstrocytes”, with increased expression of astrocyte markers (**Fig. 3.1a-b**) as well as astrocyte-specific genes in general (**Fig. S3.1**) compared to astrocytes generated using the original protocol from TCW *et al.*¹⁸ To confirm that iAstrocytes were capable of performing typical astrocyte functions such as maintaining the blood-brain barrier²⁰ or promoting neuronal synapse maturation²¹, we co-cultured iAstrocytes with hiPSC-derived brain endothelial-like cells or neurons (see Methods). We found that brain endothelial-like cells co-cultured with iAstrocytes displayed improved barrier formation and integrity compared to mono-culture (**Fig. 3.1c**), demonstrating that iAstrocytes can promote the expected functional maturation of these cells. In addition, hiPSC-derived neurons (iNeurons) co-cultured with iAstrocytes developed synchronized calcium oscillations^{22,23} compared to iNeurons in mono-culture (**Fig. 3.1d-f**), demonstrating the ability of iAstrocytes to promote neuronal synapse maturation and consistent with the higher expression of genes encoding synapse-promoting proteins such as GPC4²⁴ and CADM1²⁵ in iAstrocytes compared to TCW astrocytes.

Having validated that iAstrocytes performed typical astrocyte functions, we next tested whether iAstrocytes could be used to model inflammatory astrocyte reactivity. It has been shown that the cytokines IL-1 α +TNF+C1q induce inflammatory reactivity *in vitro* in both primary

mouse astrocytes⁸ as well as human cerebral organoid-derived astrocytes²⁶. We found that treatment of iAstrocytes with IL-1 α +TNF+C1q recapitulated previously reported *in vitro* phenotypes of inflammatory reactivity such as decreased phagocytosis of CNS substrates, decreased support of neuronal synapse maturation, and neurotoxicity^{8,26}. Specifically, iAstrocytes displayed decreased phagocytosis of pHrodo-labeled synaptosomes after treatment with IL-1 α +TNF+C1q (**Fig. 3.1g-h**). In addition, IL-1 α +TNF+C1q treatment of iAstrocytes co-cultured with iNeurons abolished the development of synchronized neuronal calcium oscillations (**Fig. 3.1d-f**), demonstrating decreased support of neuronal synapse maturation by iAstrocytes. Finally, we found that the conditioned media from IL-1 α +TNF+C1q-treated iAstrocytes was toxic to iNeurons (**Fig. 3.1i**).

In addition to recapitulating key functional phenotypes of inflammatory reactivity, iAstrocytes also responded to IL-1 α +TNF+C1q at the transcriptomic level in a similar manner as primary mouse astrocytes and human iPSC-derived astrocytes generated using alternative protocols (**Fig. S3.2a-e**). We noted, however, that the differentially expressed genes (DEGs) induced by IL-1 α +TNF+C1q in hiPSC-derived astrocytes were not restricted to the previously defined “pan-reactive” and “A1” reactive categories (**Fig. S3.2c**). This finding mirrored similar observations from Barbar *et al.*²⁶, and supports the growing consensus that there is a multitude of distinct, context-specific reactive astrocyte states²⁶.

To find a cell-surface marker for inflammatory reactivity that is also functionally involved in neuroinflammation, we examined the DEGs induced by IL-1 α +TNF+C1q in iAstrocytes. We found a dramatic increase in the transcript levels of *VCAM1* (**Fig. 3.1j**), which encodes a cell-adhesion sialoglycoprotein known to facilitate the infiltration of peripheral immune cells into the central nervous system (CNS) during neuroinflammation^{27,28}. We subsequently validated by flow cytometry that iAstrocytes indeed upregulated cell-surface VCAM1 after treatment with IL-

1 α +TNF+C1q (**Fig. 3.1k-l**), corroborating previous reports in the literature demonstrating induction of VCAM1 in astrocytes under pro-inflammatory conditions^{29,30}.

iAstrocytes differentiated from CRISPRi hiPSCs maintain robust knockdown activity

In order to investigate the effect of genetic perturbations on inflammatory reactivity in iAstrocytes, we generated iAstrocytes from hiPSCs stably expressing CRISPRi machinery (**Fig. 3.2a**), which enables specific and non-toxic knockdown of genes targeted by single guide RNAs (sgRNAs) delivered to the cell. We found that these iAstrocytes maintained robust CRISPRi activity, demonstrating ~100% knockdown of *TFRC* protein levels 6 days after lentiviral transduction with a single guide RNA (sgRNA) targeting *TFRC* compared to iAstrocytes transduced with a non-targeting control (NTC) sgRNA, regardless of whether the iAstrocytes were treated with IL-1 α +TNF+C1q (**Fig. 3.2b-c**).

CRISPRi screening and computational master regulator analysis uncover cellular pathways controlling inflammatory reactivity

Having established CRISPRi in iAstrocytes, we aimed to systematically interrogate inflammatory reactivity in iAstrocytes with pooled CRISPRi screening^{17,31}. We conducted screens based on two cell-autonomous phenotypes induced by IL-1 α +TNF+C1q that can be analyzed by fluorescence activated cell sorting (FACS): decreased phagocytosis of pHrodo-labeled synaptosomes (**Fig. 3.1g-h**) and upregulation of cell-surface of VCAM1 (**Fig. 3.1k-l**). For synaptosome phagocytosis, we performed the screens in both vehicle control-treated and IL-1 α +TNF+C1q-treated iAstrocytes to find genes whose knockdown could rescue or exacerbate the decrease in synaptosome phagocytosis induced by IL-1 α +TNF+C1q (**Fig. 3.3a**). For upregulation of cell-surface VCAM1, we performed the screens in only IL-1 α +TNF+C1q-treated iAstrocytes (**Fig. 3.3a**) given that in the absence of cytokine treatment, very few

iAstrocytes expressed VCAM1 (**Fig. 3.1I**). To ensure that the results from the screens are generalizable, we validated that IL-1 α +TNF+C1q also caused decreased synaptosome phagocytosis and upregulation of cell-surface VCAM1 in hiPSC-derived astrocytes generated using alternative protocols, as well as in primary mouse astrocytes (**Fig. S3.2f-i**).

In addition to pooled CRISPRi screening, we also turned to computational master regulator analysis (MRA)³²⁻³⁴ as a method to uncover cellular pathways controlling inflammatory reactivity. The workflow of MRA consisted of first reconstructing a gene regulatory network between upstream regulators (e.g. transcription factors, or kinases and phosphatases) and target genes in human astrocytes based on coexpression, which required integrating a large number of human astrocyte expression profiles collected under diverse experimental conditions³⁵ (see Methods); upstream regulators that control inflammatory reactivity were then predicted by examining the overlap between the regulons of upstream regulators with the DEGs induced by IL-1 α +TNF+C1q in iAstrocytes (**Fig. 3.3b**).

We performed MRA using the human transcription factors³⁶ (**Fig. 3.3c**) or kinases and phosphatases^{37,38} (**Fig. 3.3f**) as upstream regulators, and similarly conducted pooled CRISPRi screening using a new custom sgRNA library targeting the human transcription factors (**Fig. 3.3d-e**) and a library targeting all kinases, phosphatases, and other genes representing the “druggable genome”³⁹ (**Fig. 3.3g-h**). Together, these two approaches uncovered both expected regulators of inflammatory reactivity as well as potentially novel regulators.

For example, the top hits from both MRA and CRISPRi screens included the entire set of genes encoding all potential subunits of the NF- κ B transcription factor (*REL*, *RELA*, *RELB*, *NFKB1*, *NFKB2*; **Fig. 3.3c-e**) as well as genes encoding the upstream kinases of the canonical NF- κ B pathway (*IKBKB*, *CHUK*, *IKBKG*; **Fig. 3.3f-h**)⁴⁰. For all of the above genes (with the exception of *NFKB2*), the directionality of their screening phenotypes or master regulator analysis activity scores (see Methods) was consistent with the activation of the canonical NF- κ B

pathway being required for the induction of inflammatory reactivity. As an example, knockdown of *RELA*, which encodes the p65 subunit of the NF- κ B transcription factor, blocked the induction of cell-surface VCAM1 (**Fig. 3.3e**) and rescued the decrease in phagocytosis (**Fig. 3.3d**) induced by IL-1 α +TNF+C1q. In addition, the activity score of *RELA* from MRA was positive, consistent with the positive average log-fold change of DEGs under the control of *RELA*. For the case of *NFKB2*, knockdown of which actually increased VCAM1 induction by IL-1 α +TNF+C1q (**Fig. 3.3e**), it is possible that the encoded protein, p100, may act to inhibit *RELA*-dependent transcription through the cytoplasmic sequestration of p65⁴¹.

Given that the canonical NF- κ B pathway is a well-studied master regulator of cellular responses to inflammatory stimuli⁴², its strong enrichment in the top hits from the screens and MRA serves as a positive control for the technical quality of the screens and the validity of the MRA pipeline. As a further control for the technical quality of the screens, we validated the phenotypes of selected top hits in independent experiments (**Fig. S3.3**).

In addition to the canonical NF- κ B pathway, we also recovered genes involved in numerous other cellular pathways known to mediate inflammatory processes. One group of genes (*STAT3*, *CEBPB*, *CEBPD*) consisted of transcription factors classically associated with the acute phase response in the context of systemic inflammation^{43,44}. In the central nervous system, these transcription factors control similar responses in reactive astrocytes, such as the production of acute phase proteins C3 and α 1-antitrypsin (encoded by the gene *SERPINA1*) by astrocytes challenged with IL-1 and TNF⁴³ (also see **Fig. 3.1j**). Furthermore, *STAT3* is required for the full induction of astrocyte reactivity caused by spinal cord injury^{13,45,46}, and *CEBPB* has been implicated in the pathogenesis of Alzheimer's disease (AD)^{47,48}. We found that knockdown of *STAT3*, *CEBPB*, and *CEBPD* in the context of *in vitro* IL-1 α +TNF+C1q treatment surprisingly promoted the induction VCAM1 while having complex effects on phagocytosis (**Fig. 3.3d,e,h**).

Another group of genes consisted of those involved in the response to interferons (*IRF1*, *STAT1*, *IKBKE*)⁴⁹⁻⁵¹. For example, we found that knockdown of *IRF1* reduced VCAM1 induction by IL-1 α +TNF+C1q. This is consistent with the fact that interferons have been shown to potentiate the induction of VCAM1 by inflammatory cytokines^{29,52}.

Lastly, we found genes involved cellular pathways that have been relatively less studied in the context of inflammatory astrocyte reactivity. For example, we uncovered genes involved in or related to the mTOR pathway (*MTOR*, *LAMTOR3*, *LATS2*, *FOXK1*)^{53,54}, the glucocorticoid receptor pathway (*NR3C1*), the actin cytoskeleton (*ARPC3*, *ACTR2*), and also relatively uncharacterized genes such as *FOXC2* and *ZBTB7A*.

Overall, the results from CRISPRi screening and MRA demonstrate that numerous cellular pathways regulate distinct aspects of inflammatory reactivity. Of particular interest to us was the fact that knockdown of the acute phase response-related genes *STAT3*, *CEBPB*, and *CEBPD* increased the induction of VCAM1 by IL-1 α +TNF+C1q, whereas knockdown of the interferon-related gene *IRF1* decreased VCAM1 induction. Since all of the above genes are known to be involved in inflammatory responses, their opposing phenotypes suggested to us that VCAM1 upregulation may only be capturing one particular aspect of inflammatory reactivity, i.e. that there may exist distinct inflammatory reactive states, one of which is marked by VCAM1 upregulation.

CROP-seq reveals two distinct inflammatory reactive states

To gain deeper insight into how regulators uncovered by CRISPRi screening and MRA may control distinct inflammatory reactive states, we turned to CROP-seq⁵⁵. By coupling CRISPRi perturbations to single-cell transcriptomics, CROP-seq enables the recovery of perturbation-associated changes in gene expression from a pooled experiment. We selected 30 regulators (**Fig. S3.4b**) that were strong hits from CRISPRi screening and MRA for pooled

knockdown in iAstrocytes treated with vehicle control or IL-1 α +TNF+C1q, and then performed CROP-seq to characterize the effect of knockdown on IL-1 α +TNF+C1q-induced gene expression (see Methods).

Before examining the effect of knocking down different regulators on inflammatory reactivity, we first focused on iAstrocytes transduced with non-targeting control (NTC) sgRNAs. In the absence of IL-1 α +TNF+C1q, NTC iAstrocytes partitioned largely by cell cycle in uniform manifold approximation projection (UMAP), with cluster 3 corresponding to dividing cells. A small fraction (<10%) of endothelial-like and stromal-like cells were also present, corresponding to clusters 5 and 6, respectively (**Fig. 3.4a, Fig. S3.4a-c**). Upon treatment with IL-1 α +TNF+C1q, NTC iAstrocytes partitioned into two distinct inflammatory reactive states corresponding to clusters 1 and 2, with an additional cluster (cluster 4) corresponding to cycling cells (**Fig. 3.4a, Fig. S3.4a-c**).

Upon further examination of the two distinct inflammatory reactive states induced by IL-1 α +TNF+C1q, we found that iAstrocytes in cluster 1 expressed markers related to the acute phase response such as *C3*, *IL6*, and *IL1B*, whereas iAstrocytes in cluster 2 expressed markers related to interferon signaling such as *VCAM1*, *CXCL10*, and *LTB*⁵⁶ (**Fig. 3.4b**). Enrichment analysis of cluster 2 markers confirmed a strong, specific enrichment (i.e. unique to cluster 2 markers) for interferon-related pathways (e.g. “Interferon Gamma Response”, “Interferon Alpha Response”) and transcription factor regulons (e.g. STAT1, IRF1; **Fig. 3.4c**). On the other hand, cluster 1 markers showed a specific enrichment for pathways and transcription factor regulons related to the mTORC1-HIF1 α /MYC axis of metabolic control⁵⁷ (e.g. “mTORC1 Signaling”, “Hypoxia”, “Myc Targets V1”; HIF1A, CEBPD⁵⁸). For brevity, we will hereon refer to the inflammatory reactive astrocyte state corresponding to cluster 1 as “IRAS1” and the one corresponding to cluster 2 as “IRAS2”.

Given that the results from CRISPRi screening and MRA pointed towards the canonical NF- κ B pathway being required for the induction of inflammatory reactivity, we examined the effect of knocking down *RELA* (p65 NF- κ B), *IKBKG* (NEMO), and *MAP3K7* (TAK1) on the induction of IRAS1 and IRAS2 by IL-1 α +TNF+C1q in our CROP-seq data. Aligned UMAP embedding (see Methods) of *RELA*, *IKBKG*, and *MAP3K7* knockdown iAstrocytes and NTC iAstrocytes showed that *RELA* knockdown abrogated the induction of both IRAS1 and IRAS2, with *IKBKG* and *MAP3K7* knockdown showing similar but less complete effects (**Fig. 3.4d**). Examining the expression of IRAS1 and IRAS2 markers in IL-1 α +TNF+C1q-treated NTC iAstrocytes vs. IL-1 α +TNF+C1q-treated *RELA*, *IKBKG*, and *MAP3K7* knockdown iAstrocytes showed the same pattern (**Fig. 3.4e**). Lastly, using C3 and VCAM1 as markers of IRAS1 and IRAS2, respectively, we validated the above finding with flow cytometry in an independent experiment (**Fig. 3.4f**).

To gain a more global view of how knocking down different regulators affected the induction of inflammatory reactivity, we performed differential gene expression analysis for each regulator to find how regulator knockdown altered the differential expression induced by IL-1 α +TNF+C1q (**Fig. S3.4d**; see Methods). We then performed hierarchical clustering on the log-fold-changes (weighted by statistical significance) of the union of all DEGs (see Methods). We found that regulators segregated into three major groups, with one group (G1) consisting largely of regulators involved in the canonical NF- κ B pathway (*RELA*, *IKBKG*, *NFKB1*, *REL*, *CHUK*) and upstream signal transduction (*IRAK4*, *RIPK1*, *MAP3K7*), another group (G2) that contained acute phase response-related transcription factors (*CEBPB*, *CEBPD*, *STAT3*), and the last group (G3) consisting of regulators with weak knockdown phenotypes (**Fig. S3.4e**). In terms of coordinately regulated genes, we recovered 10 gene modules that displayed distinct patterns across knockdown of different regulators (**Fig. S3.4e**).

Of particular interest were modules M3, M4, and M9, which all had reduced induction upon knockdown of G1 regulators and thus appeared to be downstream of the canonical NF- κ B pathway. Interestingly, M4 genes contained and had similar enrichments as IRAS1 markers (e.g. IL6) and displayed reduced induction upon knockdown of G2 regulators, whereas M3 and M9 genes contained and had similar enrichments as IRAS2 markers (e.g. VCAM1) and displayed increased induction upon knockdown of G2 regulators (**Fig. S3.5**). This led us to hypothesize that the acute phase response-related transcription factors *CEBPB*, *CEBPD*, and *STAT3* promoted IRAS1 while inhibiting IRAS2.

IL-6 and interferons act in an autocrine-paracrine manner to drive IRAS1 and IRAS2

Given that IRAS1 expressed markers related to the acute phase response, which is driven by IL-6⁵⁹, and that IRAS2 expressed markers related to the response to interferons, we hypothesized that IL-1 α +TNF+C1q induced iAstrocytes to secrete IL-6 and interferons, which then acted on the iAstrocytes in an autocrine-paracrine manner. We found that iAstrocytes indeed secreted appreciable amounts of IL-6 (~40,000 pg/mL) and interferons (~1,000 pg/mL of IFN- β) in response to IL-1 α +TNF+C1q (**Fig. 3.5a**). iAstrocytes also secreted appreciable amounts of GM-CSF (~3,500 pg/mL), which is known to act synergistically with IL-6⁶⁰, as well as CXCL10 (~30,000 pg/mL), which is produced in response to interferons⁶¹.

To test whether the secreted IL-6 and interferons acted on the iAstrocytes in an autocrine-paracrine manner, we knocked down their receptors and downstream transcription factors and measured the induction of IRAS1 and IRAS2 by performing flow cytometry on C3 and VCAM1. We found that knockdown of *IL6R* or *IL6ST*, which respectively encode the IL-6 receptor and its signal transducing partner gp130, decreased the induction of C3+ iAstrocytes; the induction of VCAM1 in iAstrocytes increased slightly for the case of *IL6ST* knockdown but did not change for *IL6R* knockdown (**Fig. 3.5b**). Knockdown of *STAT3*, which is activated

downstream of IL-6⁶², similarly decreased the induction of C3+ iAstrocytes while increasing the induction of VCAM1+ iAstrocytes (**Fig. 3.5b**).

On the other hand, concurrent knockdown of *IFNAR1* and *IFNAR2* (see Methods), which encode subunits of the type I interferon receptor, or *IFNGR1* and *IFNGR2*, which encode subunits of the type II interferon receptor, decreased the induction of both C3+ iAstrocytes and VCAM1+ iAstrocytes (**Fig. 3.5b**). Concurrent knockdown of *STAT1* and *STAT2*, which are activated downstream of interferons⁶³, also resulted in a decrease in the induction of both C3+ iAstrocytes and VCAM1+ iAstrocytes (**Fig. 3.5b**).

As an alternative approach to assay the induction of IRAS1 and IRAS2, we assayed the production of GM-CSF and CXCL10, which should be produced by IRAS1 and IRAS2 iAstrocytes respectively on the basis of mRNA expression (**Fig. 3.5c**). Knockdown of *IL6ST* or *STAT3* decreased the production of GM-CSF but increased the production of CXCL10, whereas knockdown of *IFNAR1/2* or *STAT1/2* decreased the production of both GM-CSF and CXCL10 (**Fig. 3.5d**).

In addition to perturbing the response of iAstrocytes to autocrine-paracrine IL-6 and interferons, we also aimed to perturb transcription factors that we hypothesized to control the production of IL-6 and interferons, such as CEBPB⁶⁴ and IRF1⁴⁹, respectively. In these experiments, we stained for VCAM1 and C3 simultaneously (see Methods) to better assess the relative balance of IRAS1 and IRAS2. We noted that IL-1 α +TNF+C1q induced some iAstrocytes that were both VCAM1+ and C3+ (**Fig. 3.5e**), consistent with the fact that in our single-cell data, C3 and *VCAM1* expression was enriched but not exclusive to IRAS1 and IRAS2, respectively. We found that knockdown of *CEBPB* increased the induction of VCAM1+/C3- and VCAM1+/C3+ iAstrocytes while decreasing the induction of VCAM1-/C3+ iAstrocytes, whereas knockdown of *IRF1* did not dramatically change the induction of VCAM1+/C3- or VCAM1-/C3+ iAstrocytes but decreased the induction of VCAM1+/C3+ iAstrocytes (**Fig. 3.5e**). Furthermore,

we found that *NFKB2* knockdown phenocopied *CEBPB* knockdown (**Fig. 3.5f**), suggesting a potentially novel regulation of *CEBPB* by *NFKB2*.

To summarize our findings so far, we created a model of how IL-1 α +TNF+C1q treatment induces IRAS1 and IRAS2 through a primary NF- κ B-dependent transcriptional response followed by autocrine-paracrine IL-6 and interferon signaling feedback loops (**Fig. 3.5g**): *CEBPB/D* and *STAT3* drive the induction of IRAS1 while inhibiting the induction of IRAS2 through the IL-6 loop, whereas *STAT1/2* and *IRF1* promote the induction of both IRAS1 and IRAS2 through the interferon loop.

IRAS1 and IRAS2 correspond to reactive astrocyte states generalizable across different species and disease contexts

To test if IRAS1 and IRAS2 correspond to inflammatory reactive astrocyte states generalizable across different experimental paradigms of neuroinflammation, we integrated the NTC sgRNA-transduced iAstrocytes from our single-cell RNA-seq data to previously published astrocyte single-cell RNA-seq datasets using the anchor-based data integration functionality of Seurat⁶⁵ (see Methods).

In Barbar *et al.*²⁶, mixed cultures of neurons and glia derived from dissociation of human cerebral organoids were treated with vehicle control or IL-1 α +TNF+C1q. After isolating astrocytes from the Barbar *et al.* dataset and integrating them with NTC iAstrocytes from our study (see Methods), we found that a subset of IL-1 α +TNF+C1q-treated astrocytes from Barbar *et al.* co-clustered with IRAS1 and IRAS2 iAstrocytes (**Fig. 3.6a-c**). While Barbar *et al.* astrocytes co-clustering with IRAS1 iAstrocytes expressed IRAS1 markers such as *IL6*, *CXCL2*, and *CXCL5*, those co-clustering with IRAS2 iAstrocytes expressed IRAS2 markers such as *CXCL10*, *IFIT3*, and *ISG15* (**Fig. 3.6d**; **Fig. S3.6e**). Furthermore, the DEGs between IRAS2 vs.

IRAS1 iAstrocytes overlapped strongly with the DEGs between the corresponding co-clustering Barbar *et al.* astrocytes (**Fig. S3.6a**).

In Wheeler *et al.*⁶⁶, astrocytes were isolated by FACS from mice induced with experimental autoimmune encephalomyelitis (EAE), a widely used model of multiple sclerosis (MS), at different stages of EAE progression (naïve, acute, and remitting). After removing low-quality astrocytes from the Wheeler *et al.* dataset and integrating the remaining astrocytes with NTC iAstrocytes from our study (see Methods), we found that the vast majority of Wheeler *et al.* astrocytes from the acute stage of EAE co-clustered with IRAS1 and IRAS2 iAstrocytes (**Fig. 3.6e-g**) and also correspondingly expressed IRAS1 markers such as *Srgn*, *Cxcl2*, and *Il1b* or IRAS2 markers such as *Cxcl10*, *Ifit3*, and *Isg15* (**Fig. 3.6h**; **Fig. S3.6f**). Overlap analysis of the DEGs between IRAS2 vs. IRAS1 iAstrocytes and the DEGs between the corresponding co-clustering astrocytes from Wheeler *et al.* also showed good agreement (**Fig. S3.6b**).

Lastly, in Hasel *et al.*⁵², astrocytes were isolated by FACS from mice injected peripherally with saline or lipopolysaccharide (LPS), which induces acute neuroinflammation similar to that caused by sepsis. After removing non-astrocyte cells from the Hasel *et al.* dataset, integration of the Hasel *et al.* astrocytes with NTC iAstrocytes from our study showed that a subset of Hasel *et al.* astrocytes from LPS-injected mice co-clustered with IRAS1 and IRAS2 iAstrocytes (**Fig. 3.6i-k**) and also correspondingly expressed IRAS1 markers such as *C3*, *Cxcl5*, and *Tnfaip2* or IRAS2 markers such as *Cxcl10*, *Ifit3*, and *Isg15* (**Fig. 3.6l**, **Fig. S3.6g**). Overlap analysis of the DEGs between IRAS2 vs. IRAS1 iAstrocytes and the DEGs between the corresponding co-clustering astrocytes from Hasel *et al.* further supported this correspondence (**Fig. S3.6c**).

In addition to single-cell RNA-seq datasets, we also reanalyzed bulk RNA-seq data from Anderson *et al.*⁴⁵, where astrocyte-specific RNA was purified from wild-type or astrocyte-specific *Stat3* conditional knockout (cKO) mice subject to spinal cord injury (SCI). We found that *Stat3*-dependent genes (i.e. genes with lower expression in *Stat3* cKO SCI vs. WT SCI; e.g. *C3*)

tended to be highly expressed in IRAS1 iAstrocytes (**Fig. S3.6h**), whereas Stat3-repressed genes (i.e. genes with higher expression in *Stat3* cKO SCI vs. WT SCI; e.g. *ligp1*) were enriched for genes involved in the response to interferons (**Fig. S3.6i**), similar to IRAS2 markers. Thus, the results from Anderson *et al.* not only further corroborate the existence of *in vivo* inflammatory reactive astrocyte states similar to IRAS1 and IRAS2, but also the regulatory role of STAT3 in inducing IRAS1 and inhibiting IRAS2 that we have proposed.

Markers of IRAS1 and IRAS2 are upregulated in astrocytes in human disease

Given that IRAS1 and IRAS2 corresponded to inflammatory reactive states found in various experimental paradigms of neuroinflammation, we reasoned that they would be present in the human brain as well under inflammatory conditions. In Alzheimer's disease (AD), neuroinflammation mediated by microglia and astrocytes contributes substantially to disease progression⁶⁷. We performed immunostaining of C3 and VCAM1, markers of IRAS1 and IRAS2 respectively, in post-mortem brain tissue derived from AD cases vs. age-matched controls. We found a significant increase in the abundance of C3+ astrocytes in AD (**Fig. 3.7a-b**), consistent with previous studies⁸. Notably, C3+ astrocytes tended to be localized near C3+ plaques (**Fig. 3.7a**), which we deduced to be amyloid plaques given the fact that they are known to accumulate complement proteins such as C3⁶⁸. Amyloid plaques are also known to accumulate SERPINA3⁶⁹, which is upregulated in IRAS1 reactive astrocytes and also in disease-associated reactive astrocytes found in mouse models of AD⁷⁰. As for VCAM1, we did not observe a statistically significant difference in the abundance of VCAM1+ astrocytes between AD cases vs. controls (**Fig. 3.7c-d**). Lastly, C3+ astrocytes tended to be VCAM1- (118 VCAM1- vs. 1 VCAM1+ astrocytes among C3+ astrocytes aggregated across all individuals; **Fig. 3.7a**), and VCAM1+ astrocytes tended to be C3- (13 C3- vs. 1 C3+ astrocytes among VCAM1+ astrocytes aggregated across all individuals; **Fig. 3.7c**).

In addition to AD, we also examined tissue derived from human neonatal hypoxic-ischemic encephalopathy (HIE), in which neuroinflammation contributes significantly to neuronal injury and negative neurologic sequela⁷¹. We observed increased abundance of both C3+ and VCAM1+ astrocytes in HIE (**Fig. 3.7e-h**).

DISCUSSION

Inflammatory reactive astrocytes have been implicated in numerous neurodegenerative and neuroinflammatory diseases such as Alzheimer's disease, Parkinson's disease, Huntington's disease, amyotrophic lateral sclerosis, and multiple sclerosis^{8,11}. However, we do not yet have a full understanding of the cellular pathways controlling inflammatory reactivity in these contexts. Here, we employed pooled CRISPRi screening to systematically identify genes that control the response of hiPSC-derived astrocytes to the inflammatory reactivity-inducing cytokines IL-1 α +TNF+C1q.

The scalability and homogeneity of our hiPSC-derived astrocytes ("iAstrocytes") was critical to our ability to perform pooled screens. However, it should be noted that iAstrocytes represent one of many available hiPSC-derived astrocyte models, and that there is a tradeoff between the scalability and maturation status of hiPSC-derived astrocytes. For our study, we found that iAstrocytes sufficiently modeled inflammatory reactivity, and we also ensured that the phenotypes we investigated were conserved across different hiPSC-derived astrocyte models.

Following up on the top hits from our CRISPRi screens with single-cell transcriptomics, we identified two distinct inflammatory reactive astrocyte states – "IRAS1" and "IRAS2" – driven by autocrine-paracrine IL-6 and interferon signaling. We found that *STAT3* promoted IRAS1 while inhibiting IRAS2 through IL-6, whereas *STAT1/2* and *IRF1* promoted both IRAS1 and IRAS2 through interferons. Importantly, we found that IRAS1 and IRAS2 corresponded to inflammatory reactive astrocyte states found in other experimental contexts, both *in vitro* and *in*

vivo. In light of the cellular pathways driving IRAS1 and IRAS2, we propose that IRAS1 be referred to in a general context as “STAT3-dependent reactivity”^{13,46,72} and IRAS2 as “interferon-responsive reactivity”^{52,73,74}.

It is likely that STAT3-dependent vs. interferon-responsive astrocyte reactivity have distinct functional outputs. Several studies already point towards potential functional outputs of STAT3-dependent reactivity. For example, in Anderson *et al.*⁴⁵, astrocyte-specific deletion of *Stat3* was shown to prevent proper axon regeneration after spinal cord injury, suggesting that STAT3-dependent reactivity may promote axon regeneration.

On the other hand, interferon-responsive reactivity may play an important role in EAE and MS. For example, Rothhammer *et al.*⁷⁵ showed that inhibiting type I interferon signaling in astrocytes exacerbated the severity of EAE. Similarly, Hindinger *et al.*⁷⁶ showed that inhibiting type II interferon in astrocytes exacerbated the severity of clinical symptoms during peak disease. Furthermore, given that interferon-responsive reactive astrocytes upregulate VCAM1 and were shown to be adjacent to vasculature in Hasel *et al.*⁵², they may be important for controlling the trafficking of peripheral immune cells into the CNS parenchyma.

We believe that our work here will serve as a valuable resource for future work to further characterize the functional outputs of STAT3-dependent vs. interferon-responsive astrocyte reactivity. More generally, the approach pioneered here could be applied to uncover regulators of different reactive astrocytes states induced by other perturbations, which will pave the way for characterizing their functions and targeting them therapeutically.

ACKNOWLEDGEMENTS

We thank Emmy Li, Brandon Desousa, Indigo L. V. Rose, Vukasin Jovanovic, Zuzana Krejciova, and Nawei Sun for contributions to preliminary studies and discussions. We thank Professors Anna Molofsky, Aimee Kao, and Michael Oldham for serving on KL’s thesis

committee. We thank members of the Kampmann lab (Greg Mohl, Sydney Sattler, Olivia Teter) for discussions and feedback on the manuscript. We thank Brian Woo for cloning the transcription factors sgRNA library. This research was supported by NIH grant F30 AG066418 to KL, Chan Zuckerberg Initiative Ben Barres Early Career Acceleration Awards to ESL and M. Kampmann, NIH/NINDs grants (R01NS097551, P01NS083513, R21NS119954) to SF, and NIH grants P30 EY02162-39 and R03AG063157 to EMU. SF is a Harry Weaver Neuroscience Scholar of the National Multiple Sclerosis Society.

AUTHOR CONTRIBUTIONS

KL and M. Kampmann. conceptualized and led the overall project, and wrote the manuscript with input from all co-authors. KL performed the majority of experiments with support from BR and performed all data analysis. HK performed immunostaining of AD tissues provided by MSS and co-culture experiments with guidance from ESL, and WX performed immunostaining of HIE tissue with guidance from SF. M. Koontz generated hiPSC-derived astrocytes using the methods of Krencik *et al.* and Li *et al.* with guidance from EMU. M. Krawczyk and YZ supplied unpublished human astrocyte RNA-seq data for master regulator analysis.

COMPETING INTERESTS STATEMENT

M. Kampmann has filed a patent application related to CRISPRi and CRISPRa screening (PCT/US15/40449) and serves on the Scientific Advisory Board of Engine Biosciences, Casma Therapeutics, and Cajal Neuroscience, and is an advisor to Modulo Bio and Recursion Therapeutics. None of the other authors declare competing interests.

DATA AVAILABILITY STATEMENT

Bulk RNA-seq data of hiPSC-derived astrocytes generated in this study shown in Fig. S3.2 are available on the Gene Expression Omnibus (GEO) under accession code GSE182307. The raw single-cell RNA-seq data and UMI count matrices from the CROP-seq experiment are available on GEO under accession code GSE182308. Processed data from the CRISPRi screens and CROP-seq experiment can also be interactively explored on CRISPRbrain (<https://www.crisprbrain.org/>).

CODE AVAILABILITY STATEMENT

The full analysis pipeline (including code and processed data objects) used for master regulator analysis, analysis of CROP-seq data, and integration with previously published single-cell RNA-seq datasets is available at <https://kampmannlab.ucsf.edu/inflammatory-reactive-astrocyte-analysis>.

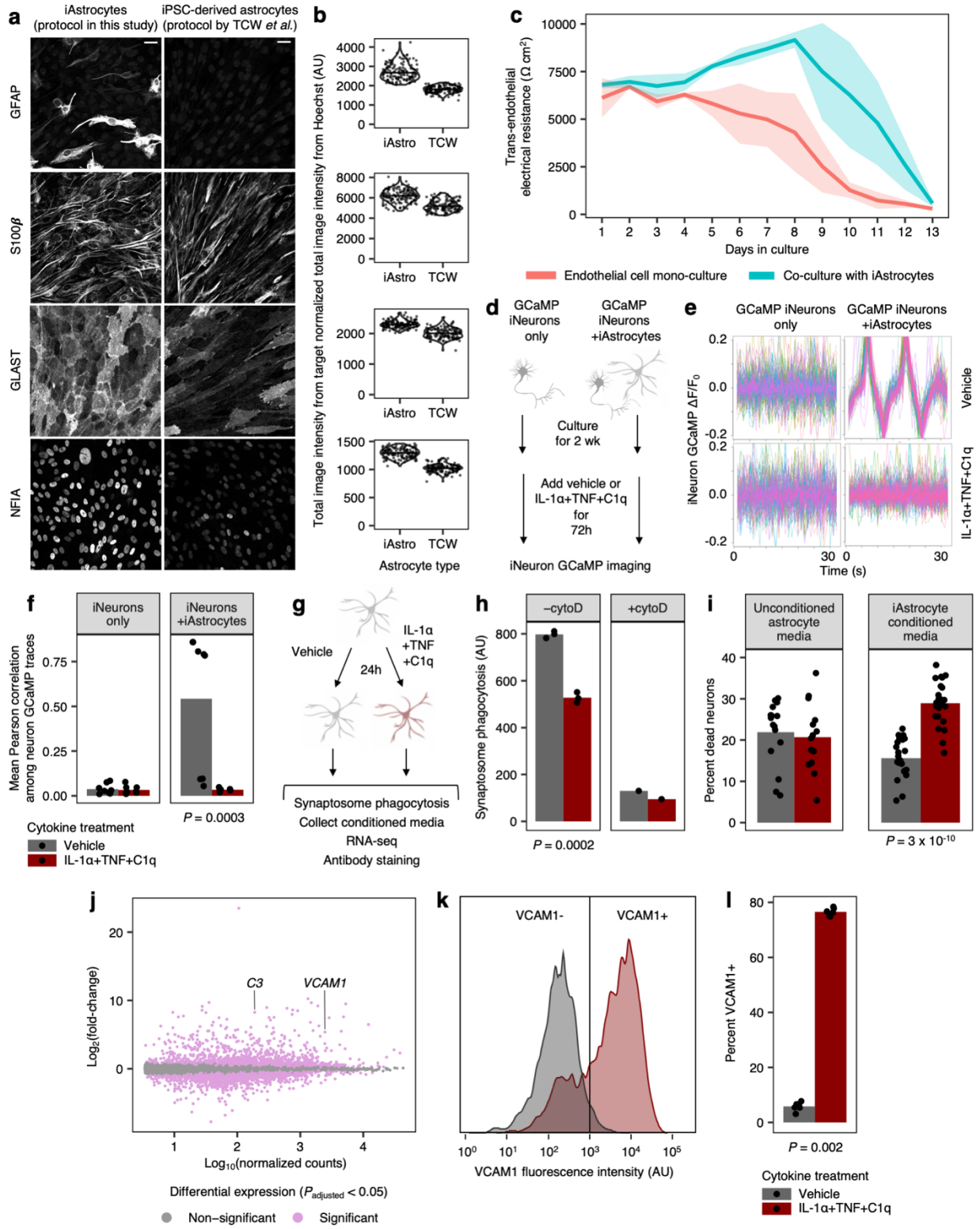


Fig. 3.1 (Legend overleaf)

Fig. 3.1 | iPSC-derived astrocytes (iAstrocytes) perform canonical astrocyte functions and recapitulate key aspects of inflammatory reactivity upon treatment with IL-1 α +TNF+C1q.

a, Representative immunofluorescence micrographs of astrocyte marker expression in iAstrocytes vs. iPSC-derived astrocytes generated using the protocol from *TCW et al.*¹⁸ Scale bar: 60 μ m. **b**, Quantification of astrocyte marker expression measured by immunofluorescence (see Methods) in iAstrocytes (iAstro) vs. astrocytes generated using the *TCW et al.* protocol (TCW); data points represent fields of view collected over two experimental replicates. **c**, Barrier integrity of brain endothelial-like cells cultured alone or with iAstrocytes over time; lines represent group means ($n = 5-6$ per condition), and shaded bands around lines represent 95% confidence intervals. **d**, Workflow schematic of calcium imaging experiments using GCaMP-expressing iPSC-derived neurons (iNeurons) cultured alone or with iAstrocytes. **e**, Neuronal calcium activity traces of GCaMP iNeurons co-cultured with iAstrocytes treated with vehicle control or IL-1 α +TNF+C1q; traces from individual neurons are colored differently and overlaid. **f**, Quantification of synchrony between neuronal calcium activity traces in iNeuron mono-cultures or iNeuron + iAstrocyte co-cultures treated with vehicle control or IL-1 α +TNF+C1q ($n = 8$ experimental replicates for each condition). **g**, Workflow schematic of experiments assessing inflammatory reactivity induced by IL-1 α +TNF+C1q in iAstrocytes. **h**, Phagocytosis of pHrodo-labeled rat synaptosomes (median pHrodo fluorescence intensity measured by flow cytometry) by iAstrocytes treated with vehicle control or IL-1 α +TNF+C1q in the absence ($n = 3$) or presence ($n = 1$) of cytochalasin D (cytoD); n is number of experimental replicates. **i**, Percentage of dead cells (measured by TO-PRO-3 permeability) for iNeurons incubated with unconditioned astrocyte media +/- IL-1 α +TNF+C1q or astrocyte media conditioned by iAstrocytes treated with vehicle control or IL-1 α +TNF+C1q ($n = 23-24$ experimental replicates for each condition). **j**, Log-scaled fold change vs. average expression of differentially expressed genes (measured by RNA-seq) induced by IL-1 α +TNF+C1q in iAstrocytes ($n = 3$ experimental replicates for each condition). **k**, Representative histogram of cell-surface VCAM1 levels (measured by flow cytometry) in iAstrocytes treated with vehicle control or IL-1 α +TNF+C1q. **l**, Percent of VCAM1+ iAstrocytes (measured by flow cytometry) after treatment with vehicle control or IL-1 α +TNF+C1q ($n = 3$ experimental replicates for each condition). The two-sided Mann-Whitney U-test was used in panels **f**, **i**, and **l**. The two-sided Student's t-test was used in panel **h**.

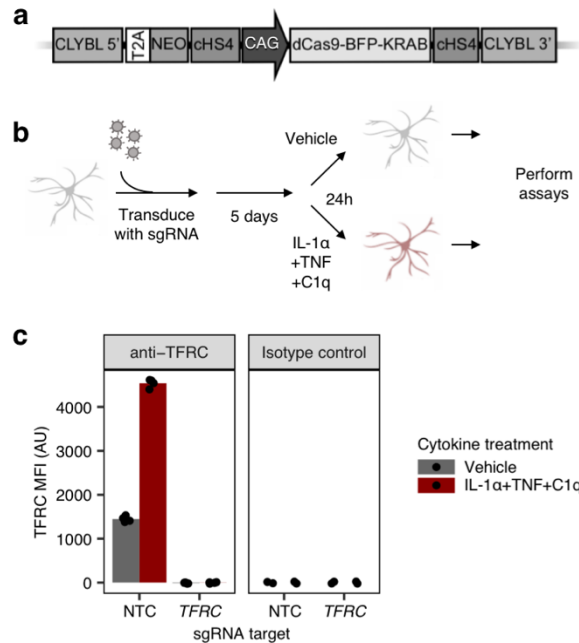


Fig. 3.2 | CRISPR interference (CRISPRi) platform in iAstrocytes. **a**, Schematic of CRISPRi machinery cassette. **b**, Workflow schematic of experiments involving lentiviral sgRNA transduction for CRISPRi knockdown. **c**, Cell-surface TFRC levels (measured by flow cytometry using an anti-TFRC antibody or isotype control; MFI: median fluorescence intensity) in iAstrocytes transduced with a non-targeting control (NTC) sgRNA or a sgRNA targeting *TFRC*, treated with vehicle control or IL-1 α +TNF+C1q ($n = 4$ for anti-TFRC, $n = 2$ for isotype control; n is number of experimental replicates).

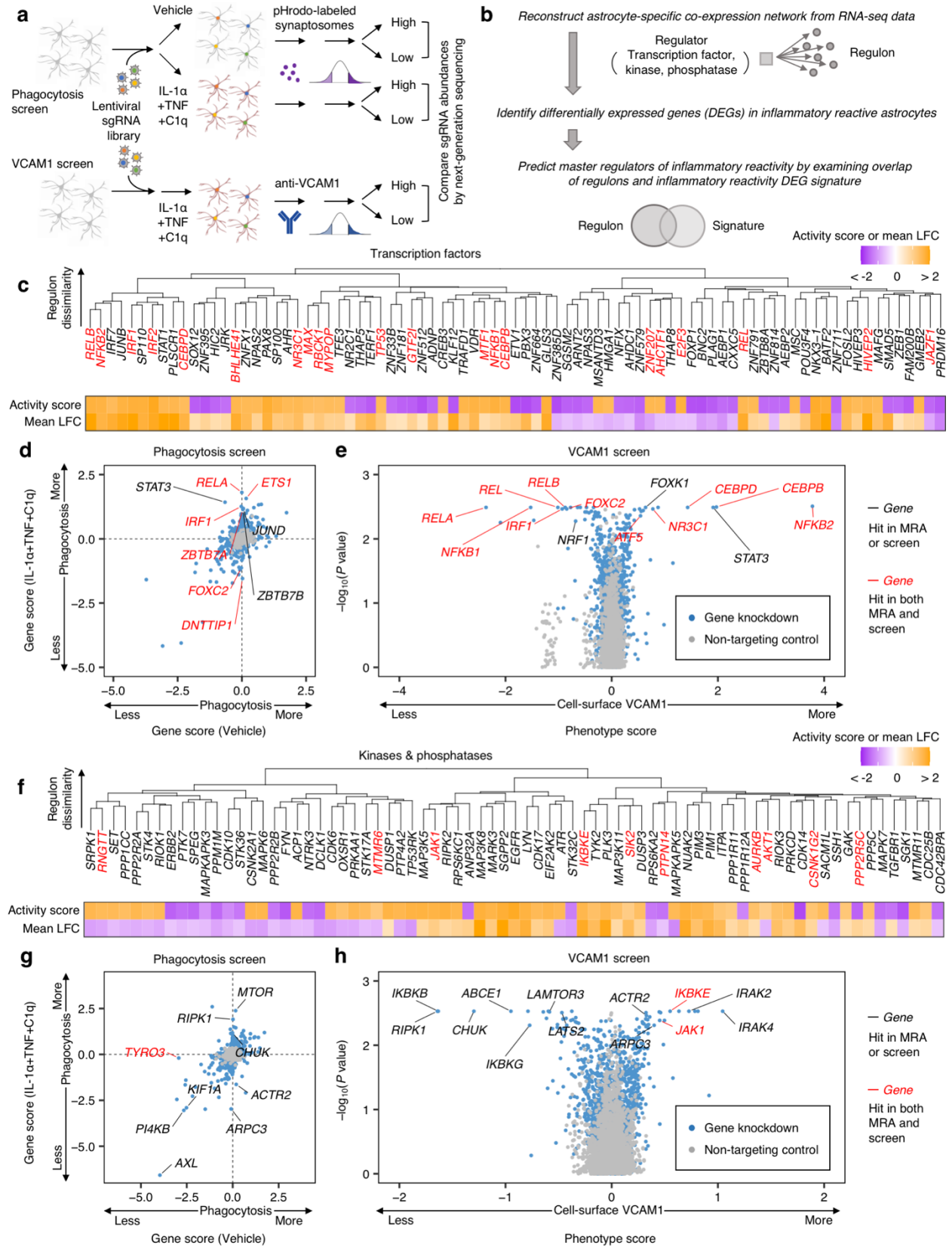


Fig. 3.3 (Legend overleaf)

Fig. 3.3 | CRISPRi screening and master regulator analysis uncover regulators of inflammatory reactivity. **a**, Workflow schematic of synaptosome phagocytosis and cell-surface VCAM1 CRISPRi screens ($n = 2$ experimental replicates for each condition). **b**, Workflow schematic of bioinformatic master regulator analysis (MRA). **c, f**, Clustering of transcription factors (**c**) or kinases and phosphatases (**f**) predicted to regulate inflammatory reactivity based on regulon overlap (see Methods); the activity score and regulon mean log-fold-change (LFC) associated with each predicted regulator (see Methods) are shown below the dendrogram. **d, g**, Scatterplot of gene scores (see Methods) of transcription factors (**d**) or the druggable genome (**g**) from synaptosome phagocytosis screens on iAstrocytes treated with vehicle control vs. IL-1 α +TNF+C1q. **e, h**, Volcano plot of phenotype scores and associated log-scaled P values (see Methods) of transcription factors (**e**) or the druggable genome (**h**) from cell-surface VCAM1 screens on iAstrocytes treated with IL-1 α +TNF+C1q.

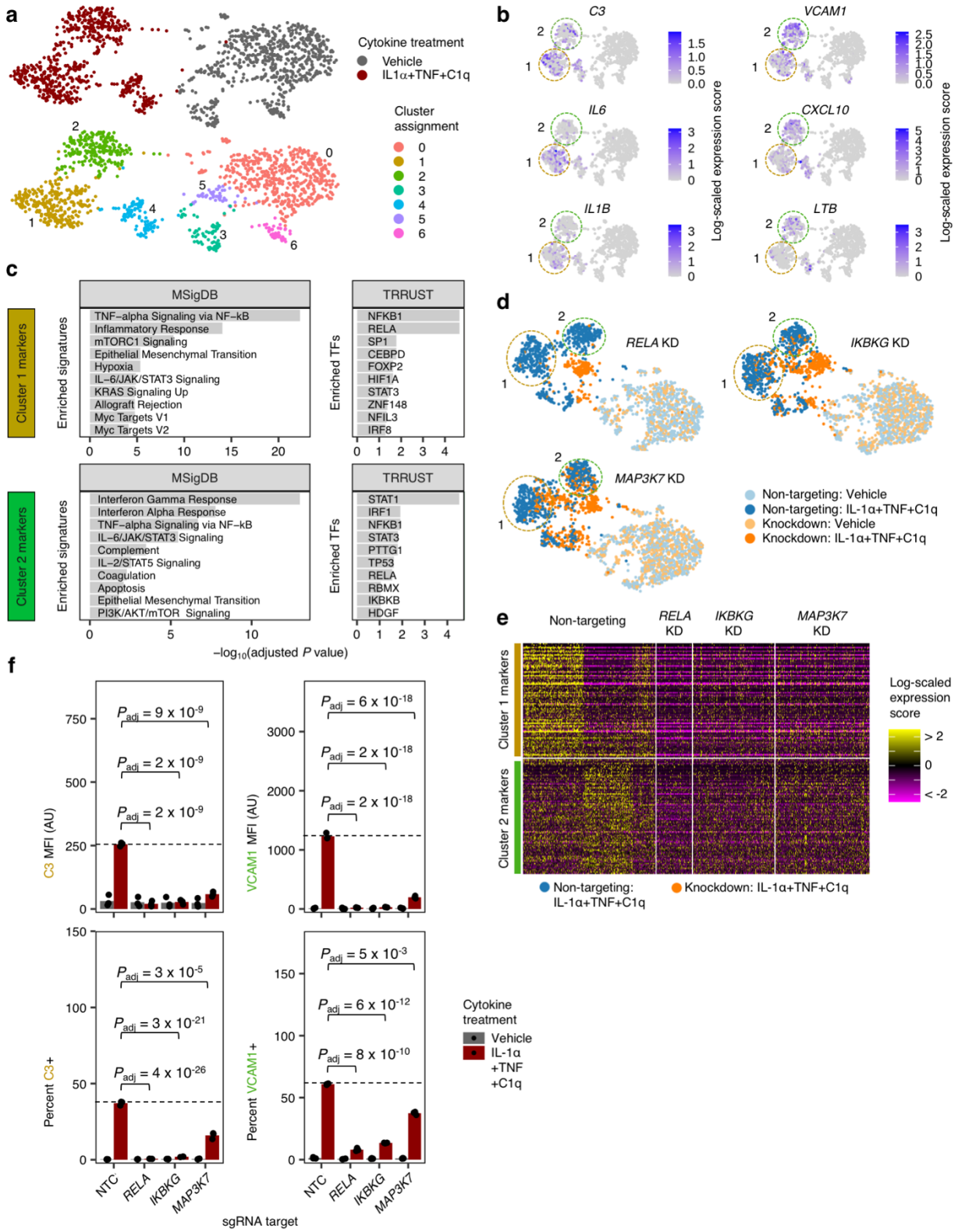


Fig. 3.4 (legend overleaf)

Fig. 3.4 | CROP-seq of iAstrocytes reveals two distinct inflammatory reactive states dependent on the canonical NF- κ B pathway. **a**, Uniform manifold approximation projection (UMAP) of iAstrocytes transduced with a non-targeting control (NTC) sgRNA treated with vehicle control or IL-1 α +TNF+C1q, colored by cytokine treatment or cluster assignment. **b**, Visualization of transcript levels of selected Cluster 1 and Cluster 2 markers in the iAstrocytes shown in panel **a**, overlaid onto the same UMAP embedding. **c**, Cellular pathway (MSigDB⁷⁷) and upstream transcription factor (TRRUST⁷⁸) enrichment analysis of Cluster 1 and Cluster 2 markers; TF – transcription factor. **d**, Aligned UMAP embedding (see Methods) of NTC sgRNA transduced iAstrocytes with iAstrocytes transduced with sgRNAs knocking down *RELA*, *IKBKG*, or *MAP3K7*. **e**, Heatmap of Cluster 1 and Cluster 2 marker transcript levels in IL-1 α +TNF+C1q-treated NTC sgRNA iAstrocytes compared to IL-1 α +TNF+C1q-treated *RELA*, *IKBKG*, and *MAP3K7* sgRNA iAstrocytes. **f**, VCAM1/C3 levels (MFI: median fluorescence intensity) or percent positive cells measured by flow cytometry in NTC, *RELA*, *IKBKG*, or *MAP3K7* sgRNA iAstrocytes treated with vehicle control or IL-1 α +TNF+C1q ($n = 3$ experimental replicates for each condition). Statistical significance of differences between IL-1 α +TNF+C1q-treated NTC iAstrocytes (marked by dotted line) and knockdown iAstrocytes was determined by linear regression for MFI values or beta regression for percentages (see Methods); comparisons with statistically significant differences are marked; adjustment of P values for multiple testing (P_{adj} ; Holm's method) is performed per family of tests, i.e. all comparisons made within a plot. In panels **b** and **d**, NTC sgRNA astrocytes in Cluster 1 or Cluster 2 are circled by colored dotted lines.

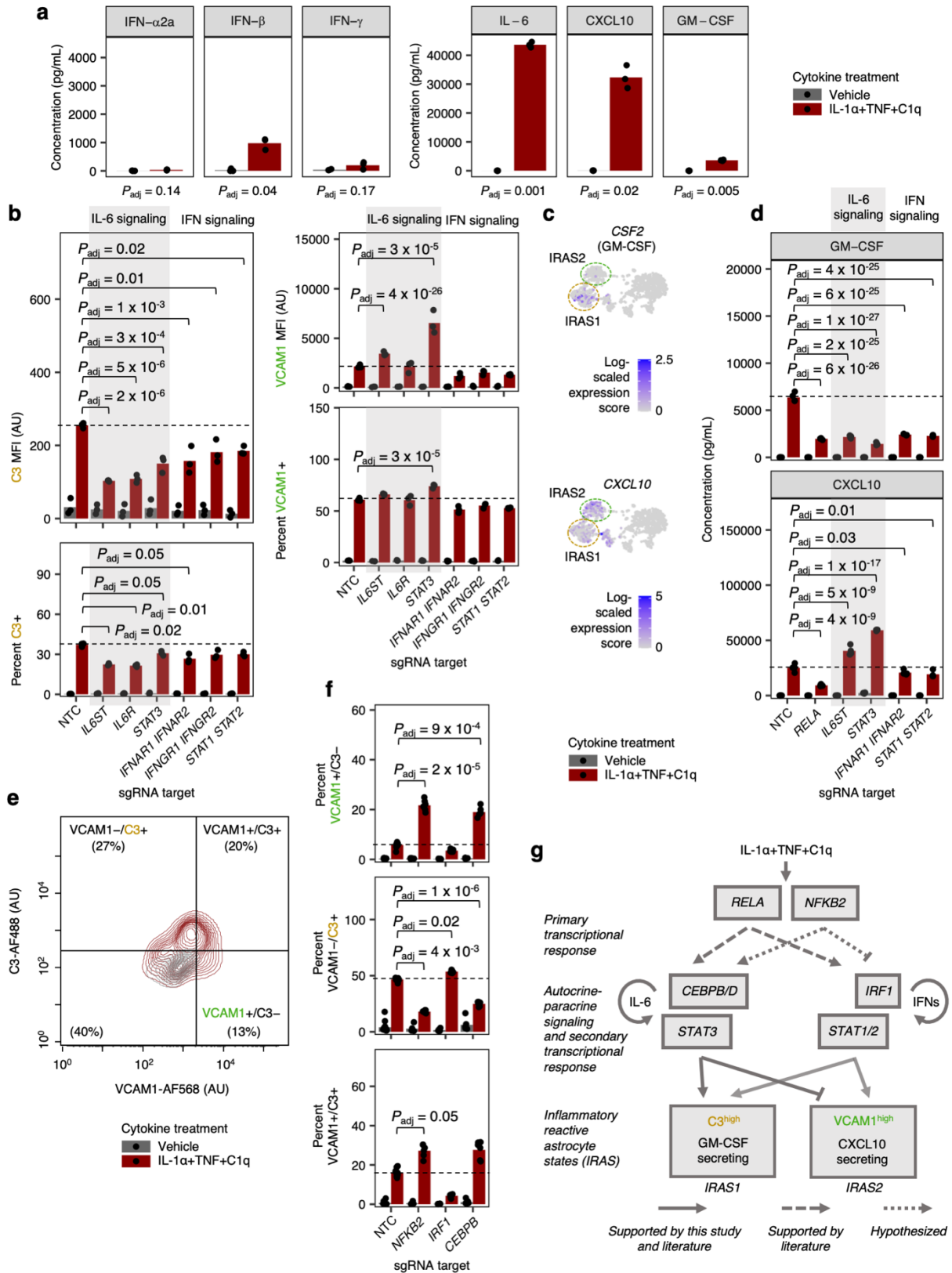


Fig. 3.5 (legend overleaf)

Fig. 3.5 | IL-6 and interferons act in an autocrine-paracrine manner to drive distinct inflammatory reactive states. **a**, Cytokine concentrations in conditioned media (measured by multi-spot electrochemiluminescence) from iAstrocytes treated with vehicle control or IL-1 α +TNF+C1q ($n = 3$ experimental replicates for each condition). **b**, VCAM1/C3 levels (MFI: median fluorescence intensity) or percent positive cells measured by flow cytometry from NTC sgRNA iAstrocytes compared to iAstrocytes transduced with sgRNAs knocking down genes involved in IL-6 or interferon (IFN) signaling; $n = 3$ experimental replicates per condition. **c**, Transcript levels of *CSF2* and *GM-CSF* overlaid onto the UMAP embedding from Fig. 3.3a. **d**, Concentration of GM-CSF or CXCL10 in conditioned media from iAstrocytes transduced with sgRNAs knocking down genes involved in IL-6 or IFN signaling; $n = 4$ experimental replicates per condition. **e**, Representative scatterplot of VCAM1 and C3 levels (measured by flow cytometry) in iAstrocytes treated with vehicle control or IL-1 α +TNF+C1q. **f**, Percent VCAM1+/C3-, VCAM1-/C3+, or VCAM1+/C3+ cells (measured by flow cytometry) in NTC, *NFKB2*, *IRF1*, or *CEBPB* sgRNA iAstrocytes treated with vehicle control or IL-1 α +TNF+C1q ($n = 6$ experimental replicates for each condition). **g**, Model schematic of transcription factors and signaling pathways controlling inflammatory reactivity. Statistical significance of differences between IL-1 α +TNF+C1q-treated NTC iAstrocytes (marked by dotted line) and knockdown iAstrocytes was determined by linear regression for MFI values or beta regression for percentages (see Methods); comparisons with statistically significant differences are marked; adjustment of P values for multiple testing (P_{adj} ; Holm's method) is performed per family of tests, i.e. all comparisons made within a plot.

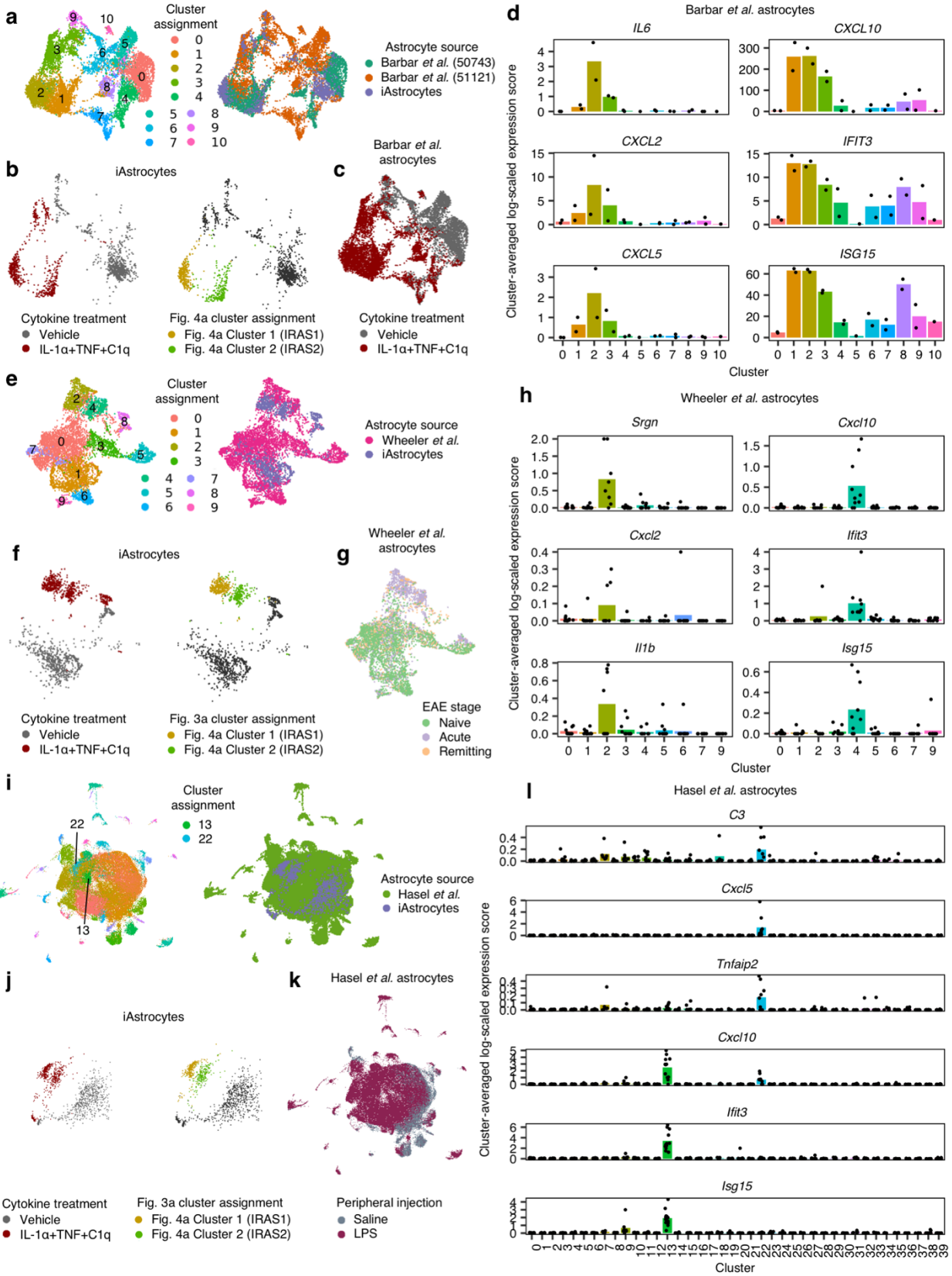


Fig. 3.6 (legend overleaf)

Fig. 3.6 | Integration of iAstrocyte single-cell data with published single-cell datasets shows conservation of distinct inflammatory reactive states across species in diverse disease contexts. **a**, UMAP of integrated analysis (see Methods) of NTC sgRNA iAstrocytes with astrocytes from Barbar *et al.*, colored by cluster assignment or astrocyte source. **b-c**, The same UMAP embedding as in **a**, showing only iAstrocytes colored by cytokine treatment or Fig. 3.3a cluster assignment (**b**) or Barbar *et al.* astrocytes colored by cytokine treatment (**c**). **d**, Cluster-averaged expression levels of selected cluster markers in Barbar *et al.* astrocytes. **e**, UMAP of integrated analysis of NTC sgRNA iAstrocytes with astrocytes from Wheeler *et al.*, colored by cluster assignment or astrocyte source. **f-g**, The same UMAP embedding as in **e**, showing only iAstrocytes colored by cytokine treatment or Fig. 3.3a cluster assignment (**f**) or astrocytes from Wheeler *et al.* colored by EAE stage (**g**). **h**, Cluster-averaged expression levels of selected cluster markers in Wheeler *et al.* astrocytes. **i**, UMAP of integrated analysis of NTC sgRNA iAstrocytes with astrocytes from Hasel *et al.*, colored by cluster assignment or astrocyte source. **j-k**, The same UMAP embedding as in **i**, showing only iAstrocytes colored by cytokine treatment or Fig. 3.3a cluster assignment (**j**) or astrocytes from Hasel *et al.* colored by LPS treatment (**k**). **l**, Cluster-averaged expression levels of selected cluster markers in Hasel *et al.* astrocytes.

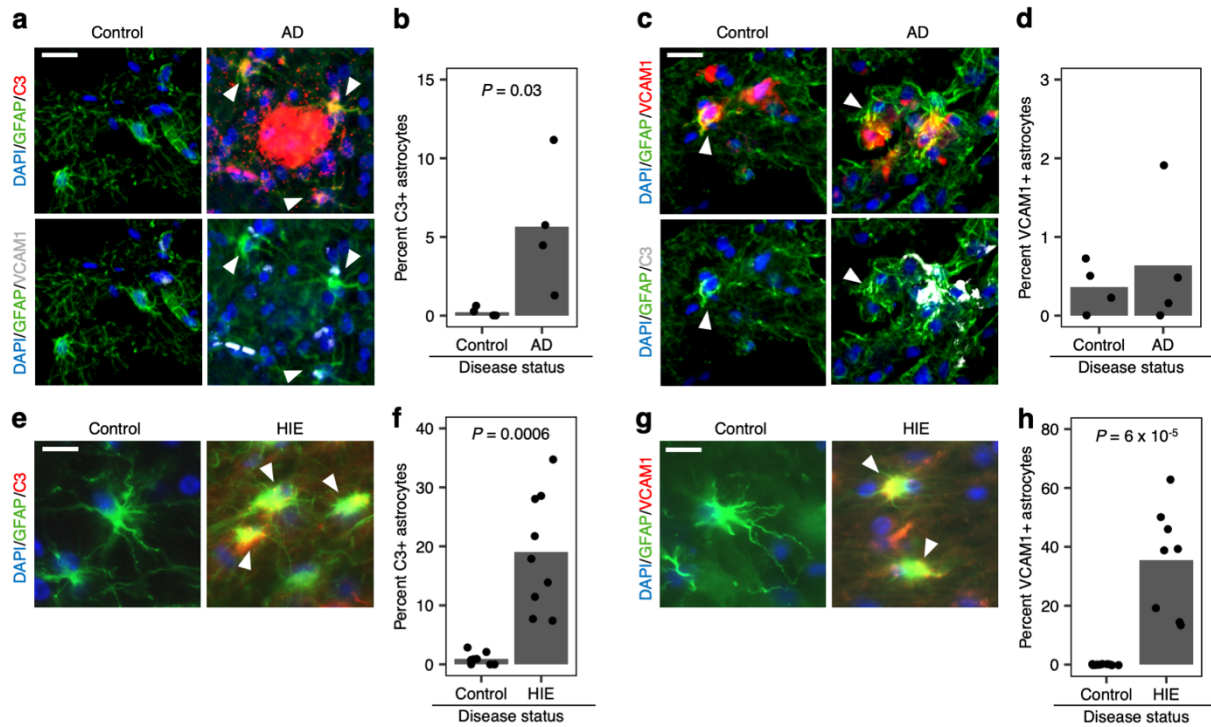


Fig. 3.7 | Markers of distinct inflammatory reactive states are upregulated in astrocytes in Alzheimer's disease (AD) and hypoxic-ischemic encephalopathy (HIE). **a,c**, Representative images of C3+ (**a**) or VCAM1+ (**c**) astrocytes (marked by arrowheads) in the AD brain compared to control; staining for VCAM1, C3, and GFAP was performed simultaneously. **b,d**, Quantification of the percentage of C3+ (**b**) or VCAM1+ (**d**) astrocytes in controls ($n = 4$) vs. AD cases ($n = 4$). **e,g**, Representative image of C3+ (**e**) or VCAM1+ (**g**) astrocytes (marked by arrowheads) in HIE compared to control; staining for VCAM1 or C3 was performed separately. **f,h**, Quantification of the percentage of C3+ (**f**) or VCAM1+ (**h**) astrocytes in control ($n = 1$ individual; data points reflect fields of view) vs. HIE ($n = 1$ individual; data points reflect fields of view). Scale bars in **a** and **c** correspond to $20 \mu\text{m}$; scale bars in **e** and **g** correspond to $10 \mu\text{m}$. P values were calculated using the Wilcoxon ranked-sum test.

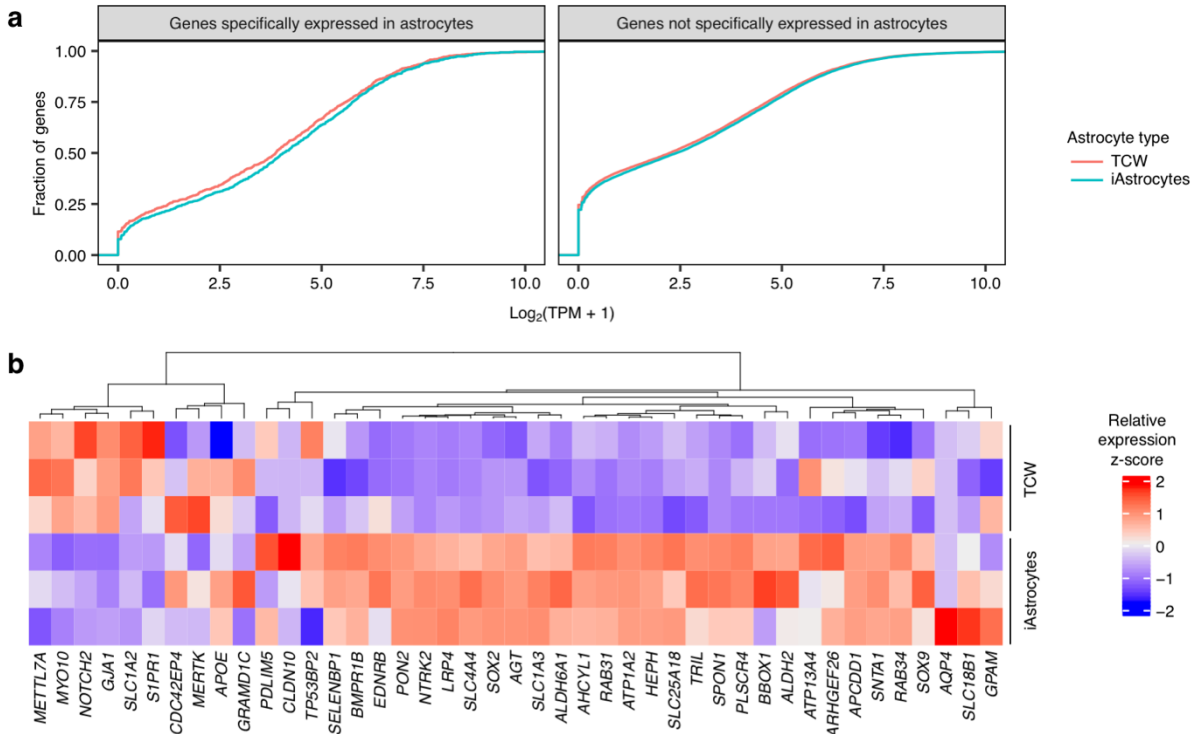


Fig. S3.1 | iAstrocytes express higher levels of astrocyte-specific genes compared to iPSC-derived astrocytes generated using the protocol from TCW *et al.*¹⁸

a, Empirical cumulative distribution functions of the mean expression of genes (averaged across biological replicates, $n = 3$) with astrocyte-specific expression (astrocyte fidelity > 40) or without astrocyte specific expression (astrocyte fidelity < 40) in iAstrocytes vs astrocytes generated using the TCW *et al.* protocol (TCW astrocytes). Genome-wide astrocyte fidelity scores were obtained from Kelley *et al.* TPM: transcripts per million. **b**, Relative expression (z-scored) of the top 50 genes with the highest astrocyte fidelity scores from Kelley *et al.*⁷⁹ (organized by hierarchical clustering, see Methods) in iAstrocytes vs. TCW astrocytes ($n = 3$ biological replicates corresponding to heatmap rows).

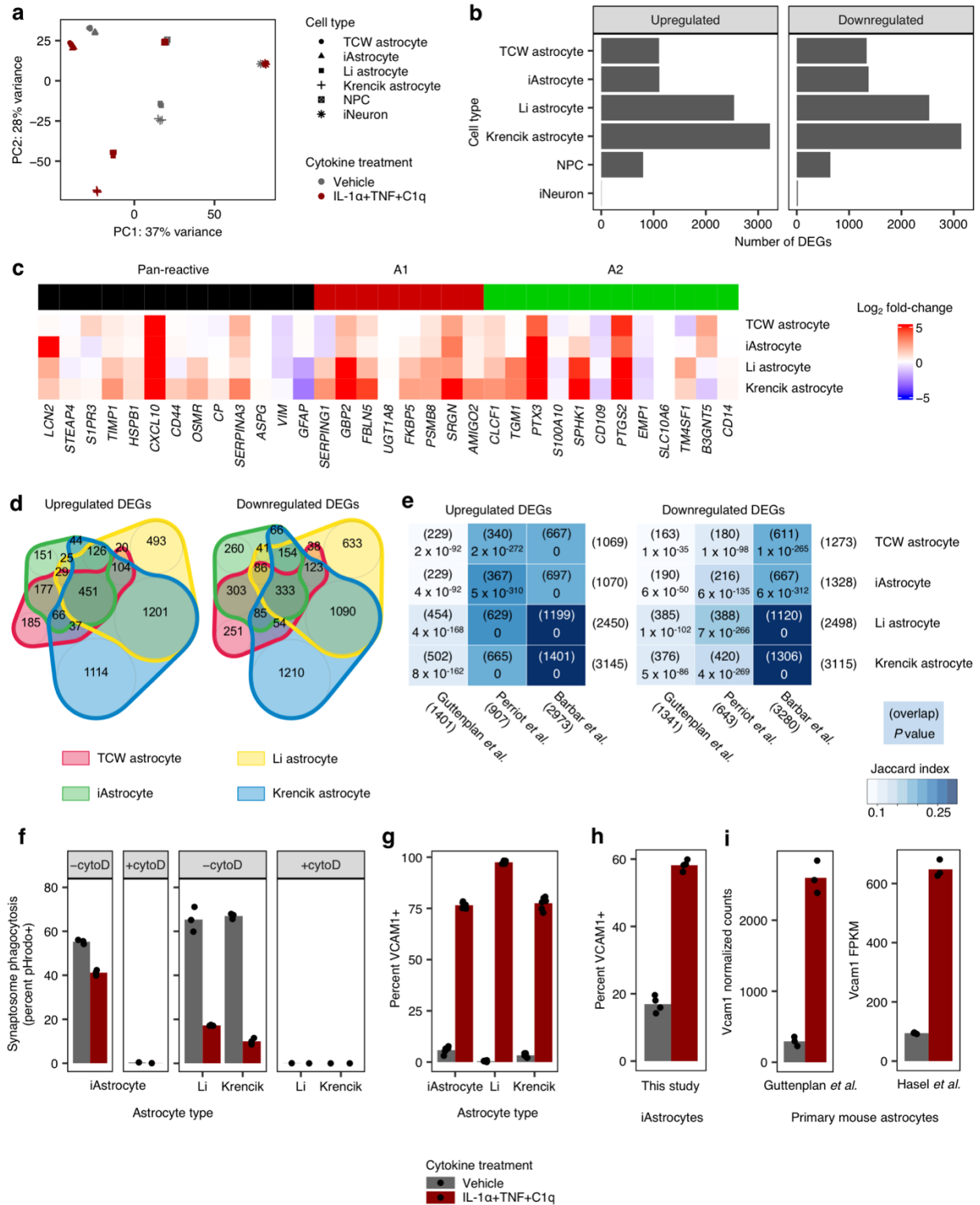


Fig. S3.2 | iAstrocytes respond to IL-1 α +TNF+C1q in a highly similar manner as iPSC-derived astrocytes generated using different protocols and primary mouse astrocytes. a, Principal component (PC) analysis plot of the gene expression profiles (top 5000 variable genes) of iAstrocytes vs. astrocytes derived using the protocols from TCW *et al.*¹⁸ (TCW

astrocytes), Li *et al.*¹⁹ (Li astrocytes), or Krencik *et al.*¹⁵ (Krencik astrocytes), as well as iPSC-derived neurons (iNeurons) and neural progenitor cells (NPCs), treated with vehicle control or IL-1 α +TNF+C1q ($n = 3$ per condition for astrocyte samples, $n = 2$ per condition for iNeuron and NPC samples). **b**, Number of differential expressed genes (DEGs) induced by IL-1 α +TNF+C1q. **c**, Log₂-fold-changes of pan-reactive, A1 reactive, and A2 reactive genes defined in Liddlelow *et al.*⁸ in iPSC-derived astrocytes from this study. **d**, Overlap of upregulated and downregulated DEGs induced by IL-1 α +TNF+C1q among iPSC-derived astrocytes from this study. **e**, Overlap of upregulated and downregulated DEGs induced by IL-1 α +TNF+C1q from iPSC-derived astrocytes from this study compared to DEGs from inflammatory reactive astrocytes in other studies. **f-g**, Phagocytosis of pHrodo-labeled synaptosomes (**f**; $n = 3$ experimental replicates per condition for -cytoD samples) or induction of cell-surface VCAM1 (**g**; $n = 6$ experimental replicates per condition) by iAstrocytes compared to Li and Krencik astrocytes. cytoD: cytochalasin D ($n = 1$ per condition). **h-i**, Induction of VCAM1 expression by IL-1 α +TNF+C1q in iAstrocytes measured by flow cytometry in this study (**h**; $n = 4$ experimental replicates per condition) or primary mouse astrocytes measured by RNA-seq in Guttenplan *et al.*⁹ and Hasel *et al.*⁵² (**i**; $n = 3$ experimental replicates per condition).

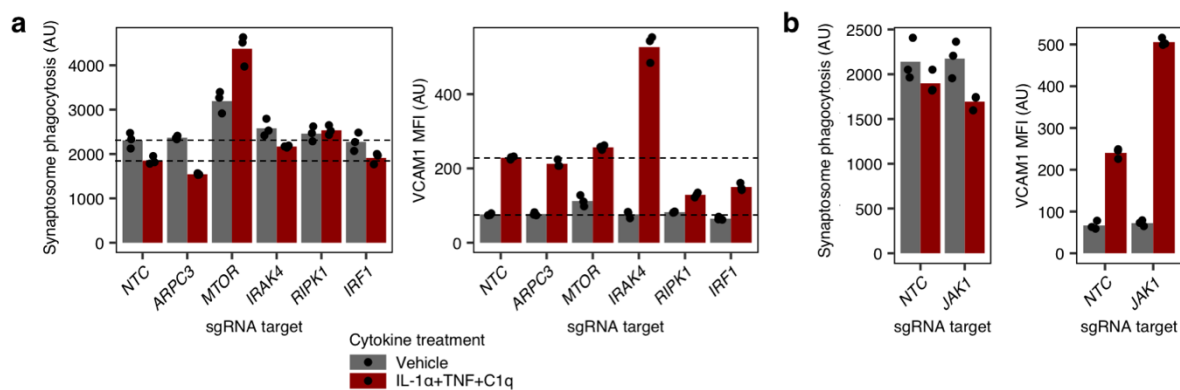


Fig. S3.3 | Validation of hits from CRISPRi screens and master regulator analysis. a-b, Phagocytosis of pHrodo-labeled synaptosomes (left; median pHrodo fluorescence intensity measured by flow cytometry) or induction of cell-surface VCAM1 (right; median VCAM1 fluorescence intensity measured by flow cytometry) by iAstrocytes transduced with non-targeting sgRNA (NTC) vs. sgRNAs targeting selected top hits from the screens shown in Fig. 3.3, treated with vehicle control or IL-1 α +TNF+C1q. MFI: median fluorescence intensity.

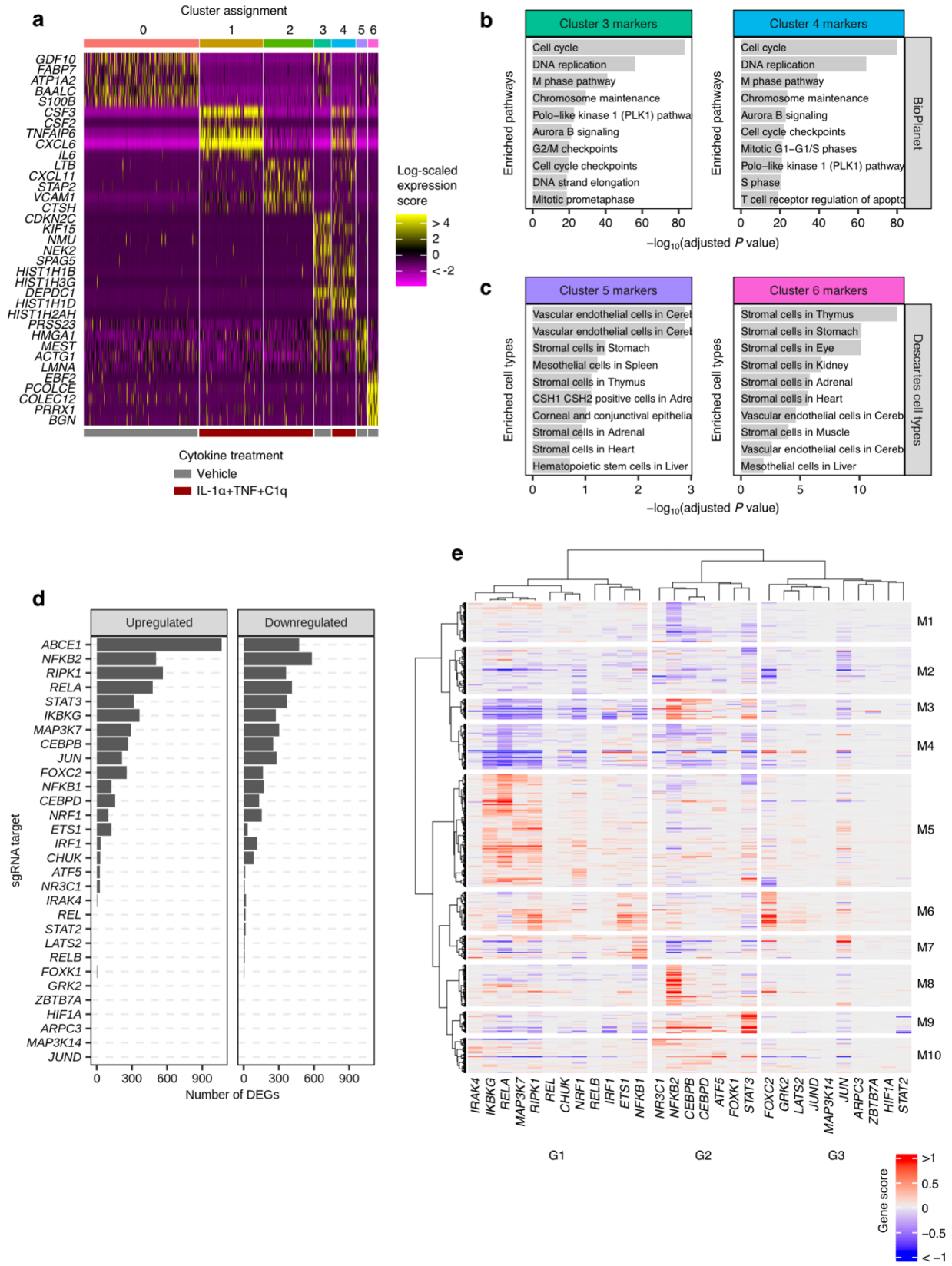


Fig. S3.4 (legend overleaf)

Fig. S3.4 | Additional analyses of CROP-seq data. **a**, Expression levels of the top cluster markers of non-targeting control (NTC) sgRNA-transduced iAstrocytes shown in Fig. 3.4a. **b-c**, Cellular pathway (BioPlanet⁸⁰) enrichment analysis of Cluster 3 and 4 markers (**b**) and cell type marker (Descartes⁸¹) enrichment analysis of Cluster 5 and 6 markers (**c**) of NTC sgRNA-transduced iAstrocytes shown in Fig. 3.4a. **d**, The number of differentially expressed genes (DEGs) whose differential expression induced IL-1 α +TNF+C1q is significantly altered by regulator knockdown. **e**, Hierarchical clustering of the *P*-value-weighted log-fold-changes (gene score) of the union of knockdown-associated DEGs from panel **d**; DEGs associated with *ABCE1* knockdown were excluded due to a significant number of DEGs also being caused by *ABCE1* knockdown in vehicle control-treated iAstrocytes.

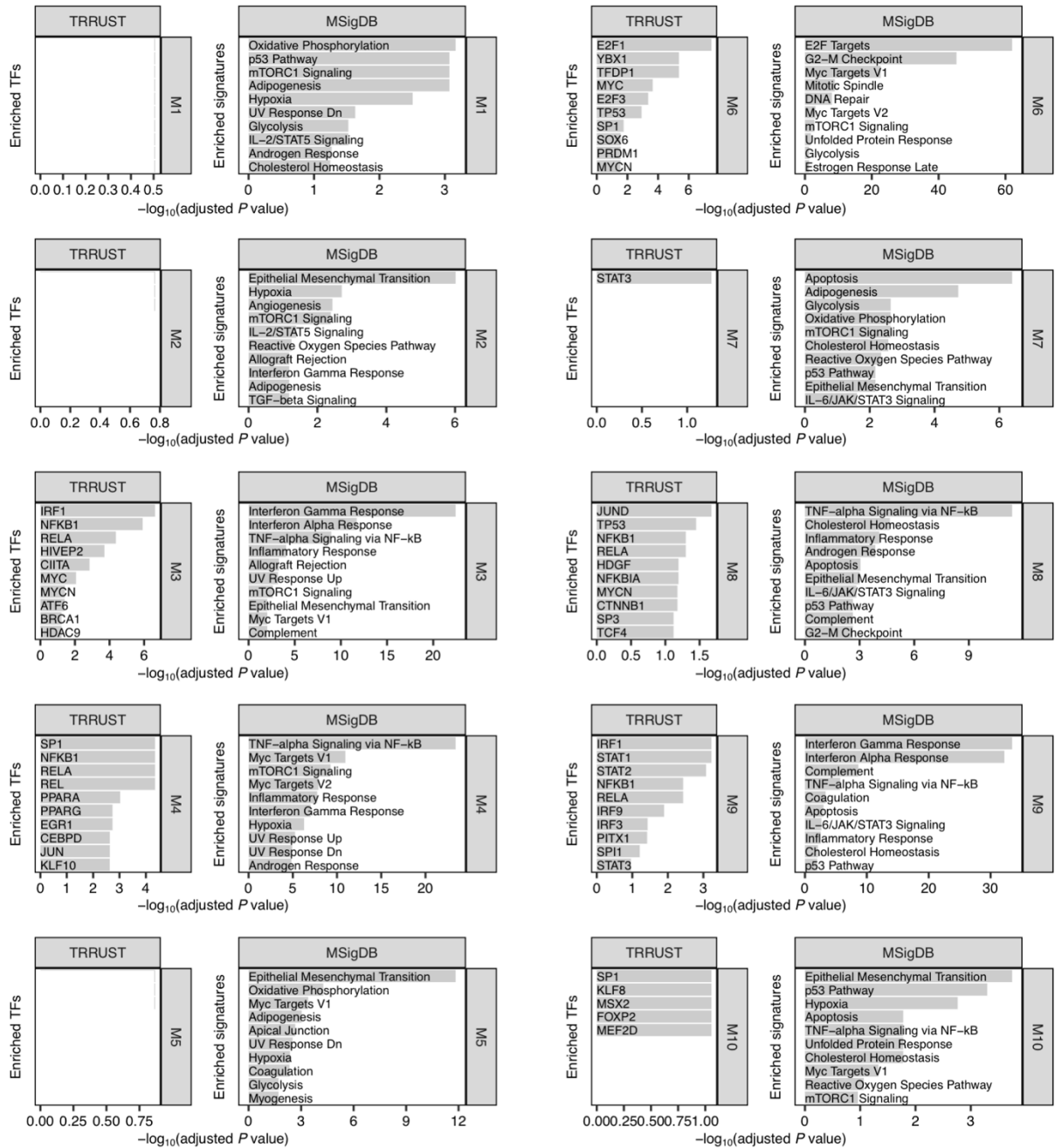


Fig. S3.5 | Enrichment analysis of CROP-seq knockdown-associated gene modules. Cellular pathway (MSigDB⁷⁷) and upstream transcription factor (TRRUST⁷⁸) enrichment analysis of gene modules from Fig. S3.4e; TF – transcription factor.

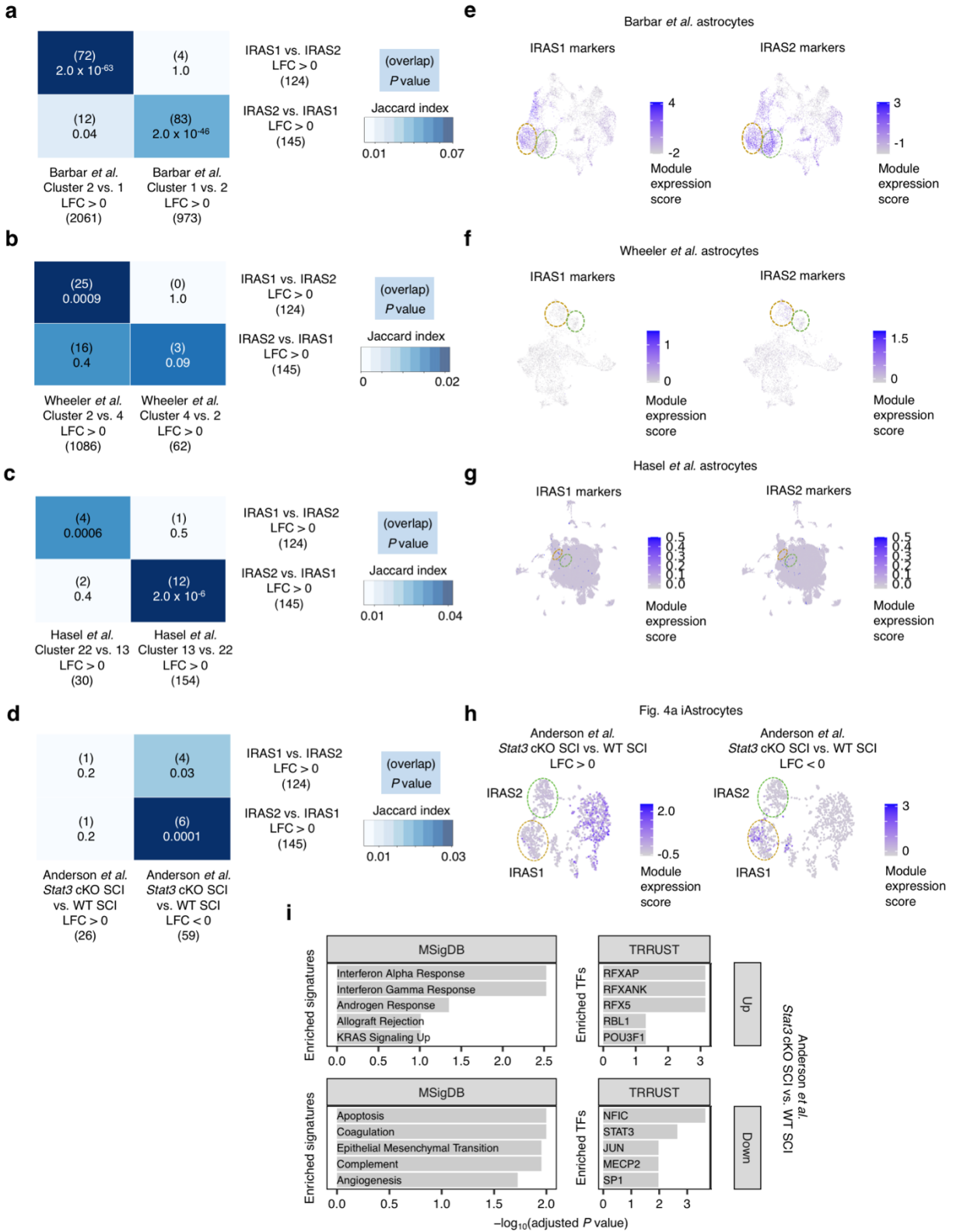


Fig. S3.6 | Overlap analysis of IRAS1 and IRAS2 markers with external datasets. a-c, Overlap analysis (Fisher's exact test; see Methods) of differentially expressed genes (DEGs) between IRAS1 vs. IRAS2 with DEGs between IRAS1- and IRAS2-co-clustering astrocytes from

Barbar *et al.*²⁶ (a), Wheeler *et al.*⁶⁶ (b), or Hasel *et al.*⁵² (c). d, Overlap analysis of DEGs between IRAS1 vs. IRAS2 with DEGs between astrocytes from *Stat3* astrocyte-specific conditional knockout (cKO) mice vs. wild-type (WT) mice subject to spinal cord injury (SCI) from Anderson *et al.*⁴⁵. e-g, Module expression score (see Methods) of IRAS1 or IRAS2 markers overlaid onto the UMAP embedding of Barbar *et al.*²⁶ (e), Wheeler *et al.*⁶⁶ (f), or Hasel *et al.*⁵² (g) astrocytes from Fig. 3.7d, h, and i, respectively. h, Module expression score of upregulated vs. downregulated DEGs between astrocytes from *Stat3* cKO SCI vs. WT SCI mice from Anderson *et al.*⁴⁵ overlaid onto the UMAP embedding of iAstrocytes from Fig. 3.4a. i, Cellular pathway (MSigDB⁷⁷) and upstream transcription factor (TRRUST⁷⁸) enrichment analysis of upregulated vs. downregulated DEGs between astrocytes from *Stat3* cKO SCI vs. WT SCI mice from Anderson *et al.*⁴⁵.

METHODS

Human iPSC (hiPSC) culture

Human iPSCs (male WTC11 background⁸²) were cultured in Essential 8 (E8) Medium (ThermoFisher Scientific cat. no. A1517001) on BioLite Cell Culture Treated Dishes (ThermoFisher Scientific) coated with Growth Factor Reduced, Phenol Red-Free, LDEV-Free Matrigel Basement Membrane Matrix (Corning cat. no. 356231) diluted 1:100 in DMEM/F12 (ThermoFisher Scientific cat. no. 11330032). Essential 8 Medium was replaced daily. When hiPSC colonies demonstrated mature morphology, the hiPSCs were either clump passaged with EDTA for routine maintenance or dissociated to a near single-cell suspension with Accutase Cell Dissociation Reagent (ThermoFisher Scientific cat. no. A11105-01) for applications requiring cell counting. For clump passaging with EDTA, hiPSCs were washed with Dulbecco's phosphate buffered saline (DPBS; Milipore Sigma cat. no. D8537) and then incubated with Versene (ThermoFisher Scientific cat. no. 15040066) for 5-7 min at room temperature; the Versene solution was then aspirated and replaced with E8 + 10 nM Y-27632 dihydrochloride ROCK inhibitor (Tocris cat. no. 125410); hiPSC colonies were then gently detached mechanically using a cell scraper, resuspended gently, and passaged at 1:10-1:30 dilution in E8 + Y-27632, with Y-27632 removed the next day. For near single-cell dissociation, hiPSCs were washed with DPBS, incubated with Accutase for 5-10 min at 37 °C, and then gently triturated with a P1000 pipette tip; the cell suspension was then diluted with PBS, collected into conical tubes, and spun down at 300 g for 3 min; hiPSCs were then resuspended in E8 + Y-27632, counted, and plated onto Matrigel-coated plates at the desired density in E8 + Y-27632; Y-27632 would be maintained until the hiPSC colonies reached the appropriate size (> ~40 cells). Studies with hiPSCs at UCSF were approved by the The Human Gamete, Embryo and Stem Cell Research (GESCR) Committee. Informed consent was obtained from the human subject when the WTC11 line⁸² was originally derived.

Cloning of *NFIA* and *SOX9* cDNA into dox-inducible cassette

To obtain *NFIA* cDNA, we designed PCR primers to amplify cDNA corresponding to transcript ENST00000403491 (*NFIA* isoform 1) from astrocyte cDNA (Forward primer complementary sequence: ATGTATTCTCCGCTCTGTCTCAC; reverse primer complementary sequence: TCCCAGGTACCAGGACTGTG). We chose to amplify cDNA corresponding to *NFIA* isoform 1 because the cDNA clone (BC022264) used in Li *et al.*¹⁹ corresponds to transcript ENST00000371187 (*NFIA* isoform 2), which we found was not expressed highly in human astrocytes. To obtain *SOX9* cDNA, we ordered cDNA clone OHu19789 (which corresponds to MGC clone BC056420) from GeneScript and then amplified *SOX9* cDNA from the plasmid (Forward primer complementary sequence: ATGAATCTCCTGGACCCCTTCA; reverse primer complementary sequence: TCAAGGTCGAGTGAGCTGTGT). We then inserted *NFIA* and *SOX9* cDNA joined by a T2A sequence into an AAVS1 safe-harbor plasmid containing a dox-inducible cassette (Addgene plasmid no. 105840, gift from Michael Ward; digested with AflIII and ClaI) using Gibson assembly (New England Biolabs; cat. no. E2611L), resulting in pKL100.

Generation of hiPSC line with stable integration of *NFIA-SOX9* cassette and CRISPRi cassette

WTC11 hiPSCs were transfected with pC13N-dCas9-BFP-KRAB⁸³ (Addgene plasmid no. 127968) to stably integrate constitutive CRISPRi machinery into the CLYBL locus using TALEN-based editing as previously described⁸³. CRISPRi WTC11 hiPSCs were then transfected with pKL100 to stably integrate the dox-inducible *NFIA-SOX9* cassette into the AAVS1 locus using the same TALEN-based editing approach. Briefly, CRISPRi WTC11 hiPSCs were dissociated with Accutase to a single-cell suspension and plated at 500,000 cells per well in a Matrigel-coated 6-well plate in E8 + 10 μ M Y-27632. The next day, a media change with E8 + Y-27632 was performed and then the hiPSCs were transfected with 2.5 μ g of pKL100, 1.25 μ g of left and right AAVS1 TALEN plasmids (Addgene plasmid no. 59025 and 59026, gift from Danwei

Huangfu), and 0.5 ug of Bcl-XL plasmid (pEF1-BCL-XL-wpre-polyA P1102, gift from Xiaobing Zhang, described in ref⁸⁴) using Lipofectamine Stem Transfection Reagent (ThermoFisher Scientific cat. no. STEM00015) following the manufacture's protocol. After hiPSCs reached confluence, they were dissociated with Accutase and passaged to a 10 cm dish in E8 + 10 uM Y-27632 + 0.1 ug/mL puromycin (ThermoFisher Scientific cat. no. A1113803) to select for clones with stable integration. Y-27632 was maintained until stable colonies formed, and puromycin was maintained for 5-7 days. The hiPSCs were then sorted for mCherry+ cells, which were then plated at 500,000 cells per well in a Matrigel-coated 6-well plate for transfection with 1.2 ug of Cre recombinase mRNA (TriLink Biotechnologies cat. no. L-7211) using Lipofectamine Stem to remove the puromycin resistance gene and mCherry. The Cre-transfected hiPSCs were then expanded and sorted for mCherry- cells, which were then plated for colony picking to generate monoclonal hiPSC lines. hiPSC clones were tested for integration of the NFIA-SOX9 cassette and removal of the puromycin resistance and mCherry by genomic PCR with the following pairs of primers:

AAVS1 FWD: CTGCCGTCTCTCTCCTGAGT

bGHpolyA REV: GCTGGCAACTAGAAGGCACAG

AAVS1 FWD: CTGCCGTCTCTCTCCTGAGT

Puro REV: GTGGGCTTGTACTIONCGGTCAT

TRE3G FWD: GTGTTGTGGAATTGCTCCAG

AAVS1 REV: AAGAGTGAGTTTGCCAAGCAGT

Neural induction of hiPSCs

Embryoid body (EB)-based neural induction of WTC11 hiPSCs stably integrated with CRISPRi machinery and dox-inducible NFIA-SOX9 was performed as previously described⁸⁵ with some modifications. Briefly, on day 0, hiPSCs were dissociated to a near single-cell suspension with Accutase, resuspended in neural induction media (NIM; see recipe below) + 10 nM Y-27632, and then transferred to an Aggrewell 800 plate (StemCell Technologies cat. no. 34815) pre-coated with Anti-adherence rinsing solution (StemCell Technologies cat. no. 07010) at 3 million cells per well for EB formation. The next day (day 1), a half media change with NIM was performed and LDN193189 (LDN; Tocris cat. no. 6053) and SB431542 (SB; Tocris cat. no. 1614) were added to final concentrations of 0.1 μ M and 10 μ M, respectively. A half media change of NIM + LDN + SB was performed every day until day 7, when EBs were transferred to a Matrigel-coated 6-well plate after performing a half media change (one well from the Aggrewell plate would be transferred to one well in the 6-well plate). The next day (day 8), a full media change with NIM + LDN + SB was performed, and then every other day afterwards until day 14, during which time neural rosettes would appear in the attached EBs. On day 14, neural rosettes were detached non-enzymatically with the following method: the attached EBs were incubated Neural Rosette Selection Reagent (NRSR; StemCell Technologies cat. no. 05832) for 1 hour at 37 °C to weaken the attachment of the neural rosettes, the NRSR was aspirated and replaced with DMEM/F12, and the rosettes were detached with targeted jetting of DMEM/F12 using a wide-orifice P1000 pipette tip and then collected into a conical tube; targeted jetting with DMEM/F12 and collection of released rosettes was repeated until the majority of rosettes had detached. Rosettes were then spun down at 100 g for 3 min, resuspended in NPC media (see recipe below), and transferred to a Matrigel-coated 6-well plate (rosettes collected from 1-2 wells would be replated into 1 well depending on the yield). From day 15 to 21, a full media change with NPC media was performed every other day, during which time neural progenitor cells (NPCs) would spread out from the attached rosettes and cover the well completely. Once

NPCs reached confluency, they were dissociated with Accutase and replated at high density (at least 1 million cells per well of a 6-well plate) in Matrigel-coated plates for expansion.

Neural induction media (NIM) formulation:

DMEM/F12 (+HEPES, +Glutamine) basal media (ThermoFisher Scientific cat. no. 11330032)

2% (v/v) B27 supplement minus Vit. A (ThermoFisher Scientific cat. no. 12587010)

1% (v/v) N2 supplement (ThermoFisher Scientific cat. no. 17502048)

Neural progenitor cell (NPC) media formulation:

DMEM/F12 (+HEPES, +Glutamine) basal media (ThermoFisher Scientific cat. no. 11330032)

2% (v/v) B27 supplement minus Vit. A (ThermoFisher Scientific cat. no. 12587010)

1% (v/v) N2 supplement (ThermoFisher Scientific cat. no. 17502048)

20 ng/mL bFGF (PeproTech cat. no. 100-18B)

Purification of NPCs

To remove contaminating neural crest cells from the NPC cultures, we used fluorescence activated cell sorting (FACS) to select for CD133+/CD271- cells following the protocol described in Cheng *et al.*⁸⁵ with modifications. Briefly, NPCs were dissociated to a single-cell suspension with Accutase, resuspended in FACS buffer (see recipe below), and then incubated with PE-conjugated CD133 antibody (1:50 dilution; Miltenyi Biotec cat. no. 130-113-108) and PerCP-Cy5.5-conjugated CD271 antibody (1:50 dilution; BD Biosciences cat. no. 560834), including single antibody-stained and unstained controls. After antibody incubation, the cell suspension was diluted 10x with FACS buffer, spun down, and resuspended in FACS buffer for sorting. CD133+/CD271- cells were sorted using a BD FACSAria Fusion cell sorter at 5,000-10,000 events per second, and then plated at 100,000 cells per cm² onto Matrigel-coated plates. Media was then changed every other day until the NPCs reached confluency, at which point the NPCs

were passaged for expansion. After 2-3 additional expansion passages after sorting, NPCs were characterized by immunostaining and qPCR for NPC markers such as PAX6 and Nestin, and then cryopreserved in NPC media + 10% DMSO.

FACS buffer formulation:

DPBS (Milipore Sigma cat. no. D8537)

1% (w/v) BSA (Milipore Sigma cat. no. A9647)

2 mM EDTA (Milipore Sigma cat. no. 324506)

Generation of iAstrocytes from NPCs

For iAstrocyte differentiation, CD133+/CD271- sorted NPCs generated from WTC11 iPCS with stably integrated CRISPRi machinery and dox-inducible NFIA-SOX9 were dissociated to a single-cell suspension with Accutase and then replated at 7,500 cells per cm² in NPC media onto a 10-cm or 15-cm dish coated with Matrigel diluted at 1:200 in DMEM/F12. The next day, media was changed to ScienCell Astrocyte Media (ScienCell Research Laboratories cat. no. 1801) + 2 µg/mL doxycycline (Millipore Sigma cat. no. D9891) to initiate iAstrocyte differentiation. A full media was then changed every other day, with doxycycline maintained at 2 µg/mL throughout the differentiation process. When the differentiating NPCs reached confluency within 3-4 days, the culture was dissociated with Accutase and split 1:10 onto new Matrigel coated dishes for expansion, with some cells saved for cryopreservation. After confluency was reached within 5-6 days, the cultures were dissociated and split 1:8, saving some cells for cryopreservation. Expansion of the cultures at 1:8 split with cryopreservation of cells after each split was continued until day 20 of differentiation, yielding iAstrocytes.

Generation of hiPSC-derived astrocytes using alternative protocols

In parallel to the generation of iAstrocytes, hiPSC-derived astrocytes were also generated from CD133+/CD271- sorted NPCs according to the protocol published in TCW *et al.*¹⁸, which mirrored the process described above for iAstrocyte generation with the exception of adding doxycycline. In addition to the protocol published in TCW *et al.*, hiPSC-derived astrocytes were also generated from WTC11 iPSCs with stably integrated CRISPRi machinery and dox-inducible NFIA-SOX9 according to Li *et al.*¹⁹, or from WTC11 iPSCs with stably integrated CRISPRi machinery according to Krencik *et al.*¹⁵.

Induction of inflammatory reactivity in hiPSC-derived astrocytes

iAstrocytes or hiPSC-derived astrocytes generated according to TCW *et al.*¹⁸ were plated onto Matrigel-coated (1:200 diluted Matrigel) 96-well plates, 24-well plates or 6-well plates at 20,000 cells per cm² in ScienCell Astrocyte Media without addition of doxycycline; hiPSC-derived astrocytes generated according to Li *et al.*¹⁹ or Krencik *et al.*¹⁵ were plated onto Matrigel-coated (1:200 diluted Matrigel) 96-well plates at ~62,500 cells per cm² in Astrocyte Maturation Media (AMM; see recipe below) without addition of doxycycline. A full media change was performed the next day, and then every other day afterwards. Five days after plating, hiPSC-derived astrocytes were treated with vehicle control or IL-1 α (3 ng/mL; Peprotech cat. no. AF-200-01A), TNF (30 ng/mL; Peprotech cat. no. AF-300-01A), and C1q (400 ng/mL; Complement Technology cat. no. A099) with a full media change in the appropriate media to induce inflammatory reactivity according to Liddelow *et al.*⁸. All assays were performed at 24 hours after cytokine treatment (see Fig. 3.1g) unless otherwise stated.

Astrocyte Maturation Media (AMM) formulation:

DMEM/F12 (+HEPES, +Glutamine) basal media (ThermoFisher Scientific cat. no. 11330032)
1% (v/v) B27 supplement minus Vit. A (ThermoFisher Scientific cat. no. 12587010)

0.5% (v/v) N2 supplement (ThermoFisher Scientific cat. no. 17502048)

1% (v/v) Antibiotic-Antimycotic (ThermoFisher Scientific cat. no. 15240062)

10 ng/mL CNTF (R&D Systems cat. no. 257-NT)

10 ng/mL BMP-4 (R&D Systems cat. no. 314-BP)

CRISPRi-mediated gene knockdown in hiPSC-derived astrocytes using lentiviral sgRNA delivery

For experiments involving CRISPRi-mediated gene knockdown, iAstrocytes were transduced with lentivirus containing single-guide RNAs (sgRNAs) at the time of plating (see Fig. 3.2b). CRISPRi sgRNAs were cloned into pMK1334⁸³ (Addgene cat. no. 127965) digested with BstXI and BlnI as previously described in Gilbert *et al.*⁸⁶. Lentivirus containing sgRNAs was produced by transfecting HEK293T cells with pMK1334 and 3rd generation lentiviral packaging plasmids with TransIT-Lenti Transfection Reagent (Mirus cat. no. MIR6606) according to the manufacturer's instructions. The lentivirus was then precipitated using Lentivirus Precipitation Solution (ALSTEM cat. no. VC150) according to the manufacturer's instructions, resuspended in DPBS at 1/10 of the original volume, and then aliquoted and stored at -80 °C. The functional titer of the lentivirus was then tested on iAstrocytes by serial dilution followed by measurement of BFP+ cells 48 hours after transduction. For all experiments involving CRISPRi-mediated gene knockdown in iAstrocytes, sufficient sgRNA lentivirus was added to transduce >70% of iAstrocytes.

Immunostaining of astrocyte markers

iAstrocytes and hiPSC-derived astrocytes generated according to TCW *et al.*¹⁸ were plated at 20,000 cells per cm² onto a Greiner μ Clear 96-well plate (Greiner Bio-One cat. no. 655087) coated with 1:200 diluted Matrigel, and then treated with vehicle control or IL-1 α +TNF+C1q as

described above. 24 hours after cytokine treatment, the astrocytes were washed with DPBS and then fixed with 4% paraformaldehyde (diluted from a 16% solution; Electron Microscopy Sciences cat. no. 15710) for 15 min at room temperature (RT). After washing three times with DPBS, blocking and permeabilization was performed with DPBS + 3% BSA + 0.1% Triton X-100 (Millipore Sigma cat. no. X100) for 30 min at RT. Primary antibodies against GFAP (1:500, rabbit polyclonal; ThermoFisher Scientific cat. no. PA1-10019), S100 β (1:500, mouse monoclonal; Millipore Sigma cat. no. S2532), GLAST (1:500, mouse monoclonal; Miltenyi Biotec cat. no. 130-095-822), or NFIA (1:200 rabbit polyclonal; Atlas Antibodies cat. no. HPA008884) were then added in blocking buffer and incubated overnight at 4 °C. Afterwards, the samples were washed with DPBS + 0.1% Triton X-100 three times, incubated with pre-adsorbed secondary antibodies (1:500 Goat anti-mouse IgG AF647, 1:500 Goat anti-rabbit IgG AF555; Abcam cat. no. ab150119 and ab150086) for 1 hour at RT, washed two times with DPBS + 0.1% Triton X-100, incubated with 1 μ g/mL Hoechst (ThermoFisher Scientific cat. no. H3570) and 1:10 ActinGreen 488 (ThermoFisher Scientific cat. no. R37110) for 20 min at RT, and then washed two additional times before imaging on an IN Cell Analyzer 6000, using a 20X 0.45 NA objective, 2x2 binning, 100-400 ms exposure, an aperture width of ~1 Airy unit, and 16 fields per well.

Generation of hiPSC-derived brain endothelial-like cells and measurement of barrier integrity

hiPSCs were differentiated to brain endothelial-like cells as previously described⁸⁷. Briefly, hiPSCs were dissociated with Accutase and seeded on Matrigel-coated plates in E8 medium containing 10 μ M Y27632 at a density of 15,000 cells/cm². Differentiation was initiated 24 hours after seeding by changing to E6 medium, with daily medium changes for 4 days. Next, cells were expanded with serum-free basal endothelial cell medium (EC medium) supplemented with

50x diluted B27 (Thermo Fisher Scientific), 1x GlutaMAX (Thermo Fisher Scientific), 10 μ M retinoic acid (Sigma Aldrich), and 20 μ g/ml FGF2 for 2 days without a media change. Following this treatment, cells were collected by a 20-minute incubation in Accutase and seeded onto Transwell filters (1.1 cm² polyethylene terephthalate membranes with 0.4 μ m pores; Fisher Scientific) coated with a mixture of 400 μ g/ml collagen IV (Sigma Aldrich) and 100 μ g/ml fibronectin (Sigma Aldrich). The following day, cells were switched to EC medium lacking FGF2 and RA. For co-culture with iAstrocytes, filters were transferred to 12-well plates containing iAstrocytes and the same medium was utilized. Starting at this time, transendothelial electrical resistance (TEER) was measured using STX2 chopstick electrodes and an EVOM2 voltameter (World precision Instruments) approximately every 24 hours. TEER readings on empty Transwell filteres were subtracted from all measurements to reflect the resistance of only the cultured cells.

Generation of hiPSC-derived neurons (iNeurons) and GCaMP iNeurons

hiPSC-derived neurons (iNeurons) were generated from WTC11 hiPSCs with stably integrated dox-inducible NGN2 (NGN2 iPSCs) according to Fernandopulle *et al.*⁸⁸. To generate GCaMP iNeurons, NGN2 iPSCs were transduced with a lentivirus delivering GCaMP6m (gift from Dr. Michael Ward). To facilitate segmentation of neuron soma, an additional lentivirus transduction was performed to deliver pMK1334 containing a non-targeting sgRNA, which confers BFP expression localized to the nucleus. Clonal lines were then isolated by colony picking, differentiated to neurons according to Fernandopulle *et al.*⁸⁸, and evaluated for homogeneity of GCaMP6m expression and the presence of spontaneous calcium oscillations. A clonal line satisfying the above criteria was selected for GCaMP imaging experiments.

Measurement of calcium activity in GCaMP iNeurons

Briefly, GCaMP iNeurons at day 3 of differentiation (see Fernandopulle *et al.*⁸⁸) were replated onto poly-D-lysine-coated 96-well plates (Corning cat. no. 354640) at 62,5000 cells per cm² in neuron media + 2 µg/mL doxycycline. For co-culture experiments, iAstrocytes were added on day 3 at 10,000 cells per cm² in an equivalent volume of ScienCell Astrocyte Media + 2 µg/mL doxycycline. For mono-culture experiments, an equivalent volume of neuron media + 2 µg/mL doxycycline was added. On day 6, half of the media was replaced with fresh neuron media + 2 µg/mL doxycycline; on day 10, half of the media was replaced with fresh neuron media without doxycycline. On day 17, the cultures were treated with vehicle control or IL-1 α +TNF+C1q (using the same final concentration as described above for astrocyte experiments) by performing a half media change with fresh neuron media. Calcium activity in GCaMP iNeurons was recorded on day 18 and day 20 with an IN Cell Analyzer 6000, using a 20X 0.45 NA objective, 2x2 binning, environmental control set to 37 °C and 5% CO₂, an aperture width of ~1 Airy unit, and 1 frame (800 ms exposure) collected per second for 40 seconds per field (1 field per well).

Isolation of synaptosomes and labeling with pHrodo

Synaptosomes were isolated from fresh Innovative Grade US Origin Rat Sprague Dawley Brains (Innovative Research, Inc.; Cat. No. IGRTSDBR) with the Syn-PER™ Synaptic Protein Extraction Reagent (ThermoFisher Scientific cat. no. 87793) according to the manufacture's protocol with minor changes. Briefly, 10 mL of Syn-PER Reagent supplemented with 1x protease inhibitor cOmplete Mini, EDTA free (Roche cat. no. 11836170001) and 1x phosphatase inhibitor PhosSTOP (Roche cat. no. 4906845001) were added per gram of brain tissue. Dounce homogenization was performed on ice and homogenate was transferred to a conical tube and centrifuged at 1200 × g for 10 minutes at 4°C. The pellet was discarded, the supernatant was transferred to a new tube, and the centrifugation step was repeated. The

supernatant was then centrifuged at $15,000 \times g$ for 20 minutes at 4°C . The supernatant was removed and the wet pellet was weighed. The synaptosome fractions were resuspended at a concentration of 50 mg/ml. $3 \mu\text{M}$ of pHrodo Red, succinimidyl ester (ThermoFisher Scientific cat. no. P36600) was added to the synaptosome fraction and incubated for 45 min at room temperature in the dark. After diluting the solution 1:10 in DPBS, the synaptosomes were spun down at $2500 \times g$ for 5 min. The supernatant was removed and then the synaptosomes were washed two times with DPBS. The pHrodo-labelled synaptosomes were resuspended in DMEM/F12 + 5% DMSO at a stock concentration of 50 mg/ml, aliquoted, and then frozen in liquid nitrogen for later use.

Measurement of synaptosome phagocytosis

For synaptosome phagocytosis experiments, pHrodo-labeled rat synaptosomes were used for iAstrocytes, and pHrodo-labeled iNeuron synaptosomes were used for Li *et al.*¹⁹ and Krencik *et al.*¹⁵ hiPSC-derived astrocytes. Briefly, astrocytes were incubated with pHrodo-labeled synaptosomes resuspended in the appropriate astrocyte media (ScienCell Astrocyte media for iAstrocytes, AMM for Li *et al.* and Krencik *et al.* astrocytes) at 1 mg/mL for 3 hours at 37°C ; for negative controls, some samples were pre-treated with 10 μM cytochalasin D (Millipore Sigma cat. no. C8273) for 15 min and also incubated with synaptosomes in the presence of 10 μM cytochalasin D to inhibit phagocytosis. After incubation with pHrodo-labeled synaptosomes, astrocytes were washed with DPBS, dissociated with Accutase, and pHrodo fluorescence was measured by flow cytometry. The gating strategy to determine the percent of phagocytic cells was based on the separation between the fluorescence histograms of samples treated or not treated with cytochalasin D.

Measurement of iNeuron viability in the presence of astrocyte conditioned media

Conditioned media was collected from iAstrocytes treated with vehicle control or IL-1 α +TNF+C1q for 24 hours, spun down at 300 g for 10 min to remove dead cells, and transferred to day 17 iNeurons after removing the original iNeuron media. Unconditioned ScienCell Astrocyte Media was used as a negative control. After 72 hours, iNeuron viability was assessed by adding 10 ug/mL Hoechst and 1 μ M TO-PRO-3 (ThermoFisher Scientific cat. no. T3605) in DPBS, incubating for 10 min at 37 °C, and then imaging on an IN Cell Analyzer 6000, using a 10X 0.45 NA objective, 2x2 binning, environmental control set to 37 °C and 5% CO₂, an aperture width of ~1 Airy unit, 200 ms exposure, and 4-9 fields per well. The percent of dead neurons (stained by TO-PRO-3) was calculated after image processing and segmentation with CellProfiler (see Data Analysis section).

Bulk RNA-seq library prep

hiPSC-derived astrocytes (iAstrocytes, TCW *et al.*, Li *et al.*, and Krencik *et al.* astrocytes), NPCs, and iNeurons were cultured in their respective media and treated with vehicle control or IL-1 α +TNF+C1q for 24 hours. RNA extraction was then performed with Zymo Quick-RNA Microprep kit (Zymo Research cat. no. R1051). 50-100 ng of RNA was then used to construct bulk RNA-seq libraries using the QuantSeq 3' mRNA-Seq Library Prep Kit FWD for Illumina (Lexogen cat. no. 015.96) following the manufacturer's instructions. The concentration of QuantSeq libraries mRNA-seq library was quantified using the Qubit dsDNA HS Assay Kit (ThermoFisher Scientific cat. no. Q32851) on a Qubit 2.0 Fluorometer. Library fragment-length distributions were quantified with High Sensitivity D5000 Reagents (Agilent Technologies cat. no. 5067-5593) on the 4200 TapeStation System. The libraries were sequenced on an Illumina NextSeq 2000 instrument with single-end reads.

Antibody staining for flow cytometry

For antibody staining of cell-surface proteins (VCAM1, TFRC), hiPSC-derived or primary mouse astrocytes were dissociated with Accutase, washed with DPBS, incubated with conjugated primary antibodies for 20 min on ice in DPBS + 1% BSA, washed with DPBS, and then resuspended in DPBS + 1% BSA for flow cytometry. For antibody staining of intracellular proteins (C3), hiPSC-derived astrocytes were dissociated with Accutase, washed with DPBS, fixed with 2% paraformaldehyde for 10 min at RT, washed twice with DPBS + 0.5% Tween 20 (Millipore Sigma cat. no. P9461), incubated with unconjugated primary antibody for 20 min at RT, washed with DPBS + 0.5% Tween 20, incubated with conjugated secondary antibody for 20 min at RT, washed with DPBS + 0.5% Tween 20, and then resuspended in DPBS + 0.5% Tween 20 for flow cytometry. For dual staining of VCAM1 and C3, the protocol for intracellular protein staining was used.

Conjugated primary antibodies:

PE-Cy7 mouse anti-VCAM1 (1:80 dilution; BioLegend cat. no. 305818)

PE-Cy7 mouse anti-TFRC (1:80 dilution; BioLegend cat. no. 334112)

Unconjugated primary antibodies:

Mouse anti-C3 (1:250 dilution; BioLegend cat. no. 846302)

Rabbit anti-VCAM1 (1:250 dilution; Abcam cat. no. ab134047)

Conjugated secondary antibodies:

AF488 goat anti-mouse IgG (1:1000 dilution; ThermoFisher Scientific cat. no. A-11029)

AF568 goat anti-rabbit IgG (1:1000 dilution; ThermoFisher Scientific cat. no. A-11036)

Pooled CRISPRi screening

To identify transcriptional regulators of inflammatory reactivity, we created a custom sgRNA library targeting the human transcription factors³⁶, using 5 sgRNAs with the highest predicted activity scores from Horlbeck *et al.*³⁹ per gene. The library was created by cloning a pool of sgRNA-containing oligonucleotides custom-synthesized by Agilent Technologies into our optimized sgRNA expression vector as previously described⁸⁶. To screen against the druggable genome, we used the H1 sub-library from Horlbeck *et al.*³⁹. The transcription factor and druggable genome libraries were packaged into lentivirus as previously described⁸³. For each experimental replicate, ~10 million iAstrocytes were plated onto 4 Matrigel-coated 15-cm dishes, transduced with the lentiviral transcription factor or H1 sgRNA library at high multiplicity of infection so that >70% of cells were transduced, treated with vehicle control or IL-1 α +TNF+C1q for 24 hours, and then incubated with pHrodo-labeled rat synaptosomes or stained for cell-surface VCAM1 (using the PE-Cy7 mouse anti-VCAM1 antibody) as shown in Fig. 3.3a. iAstrocytes were sorted into pHrodo high vs. low or VCAM1 high vs. low (top and bottom 30% of cells) using a BD FACSAria Fusion cell sorter at 5,000-10,000 events per second, and then pelleted for genomic DNA extraction. sgRNA abundances were then measured using next-generation sequencing as previously described⁸³. The screens were performed with two experimental replicates per condition.

CROP-seq

sgRNAs targeting the top hits from the CRISPRi screens and also candidate regulators selected based on literature were cloned into pMK1334. The concentration of each sgRNA plasmid was measured using the Qubit dsDNA HS Assay Kit on a Qubit 2.0 Fluorometer, and then the plasmids were pooled. iAstrocytes were transduced with lentivirus generated from the sgRNA pool at low multiplicity of infection so that <30% of cells were transduced, treated with vehicle control or IL-1 α +TNF+C1q for 24 hours, and then sorted for sgRNA-transduced cells via FACS.

Sorted iAstrocytes were then used as input for single-cell RNA-seq using Chromium Next GEM Single Cell 3' v3.1 reagents (10X Genomics cat. no. PN-1000121, PN-1000127, and PN-1000213), loading ~45,000 cells per reaction into four reactions, with two reactions for vehicle control-treated iAstrocytes and two reactions for IL-1 α +TNF+C1q-treated iAstrocytes. To facilitate association of single-cell transcriptomes with sgRNAs, sgRNA-containing transcripts were amplified as described in Tian *et al.*⁸³. The sgRNA-enrichment libraries were separately indexed and sequenced as spike-ins alongside the whole-transcriptome single-cell RNA-seq libraries on a NovaSeq 6000, recovering on average ~29,000 transcriptome reads and ~5,000 sgRNA-containing transcript reads per cell.

Measurement of cytokine concentrations

Conditioned media was collected from iAstrocytes, spun down at 300 g for 10 min to remove debris, and then frozen at -80 °C until analysis. The concentration of selected cytokines (IFN- α 2a, IFN- β , IFN- γ , IL-6, CXCL10, GM-CSF) was measured by multi-array electrochemiluminescence using custom U-PLEX plates from Meso Scale Discovery following the manufacturer's instructions.

Immunostaining of human neuropathological samples

Alzheimer's disease

Brain tissue collection procedures were approved by the Institutional Review Board at Vanderbilt University Medical Center, and written consent for brain donation was obtained from patients or their surrogate decision makers. A diagnostic post-mortem evaluation was performed to confirm the presence of Alzheimer's disease following the National Alzheimer's Coordinating Center (NACC) Neuropathology Data Form. Tissue for this study was flash-frozen in liquid nitrogen at the time of donation. Cryosectioned tissues were fixed with 4% paraformaldehyde,

photobleached with a broad-spectrum LED array for two days, and then processed for immunofluorescence staining. Samples were permeabilized with 0.3% Triton X-100 in PBS, blocked with 10% goat serum in PBS, and incubated at 4°C overnight with the following primary antibodies: mouse anti-C3 (1:200 dilution; Biolegend cat. no. 846302), chicken anti-GFAP (1:300 dilution; Aves Labs cat. no. GFAP), rabbit anti-VCAM1 (1:200 dilution; Abcam cat. no. ab134047). The following day, after washing with PBS, immunostaining was completed by a 1 hour room temperature incubation with secondary antibodies (goat anti-rabbit Alexa Fluor 488, goat anti-mouse Alexa Fluor 546, and goat anti-chicken Alexa Fluor 647; 1:1,000 dilution; ThermoFisher Scientific). After additional washes, tissue sections were mounted with the anti-fade Fluoromount-G medium containing DAPI (Southern Biotechnology). Images were acquired with a Leica DMI8 epifluorescence microscope. 6-8 fields were collected per sample.

Hypoxic ischemic encephalopathy

All human HIE tissue was collected with informed consent and in accordance with guidelines established by UCSF Committee on Human Research (H11170-19113-07) as previously described⁸⁹. Immediately after procurement, all brains were immersed in PBS with 4% paraformaldehyde for 3 d. On day 3, the brain was cut in the coronal plane at the level of the mammillary body and immersed in fresh 4% paraformaldehyde and PBS for an additional 3 d. After fixation, all tissue samples were equilibrated in PBS with 30% sucrose for at least 2 d. After sucrose equilibration, tissue was placed into molds and embedded with optimal cutting temperature medium for 30 min at room temperature followed by freezing in dry ice–chilled ethanol. UCSF neuropathology staff performed brain dissection and its evaluation. The diagnosis of HIE requires clinical and pathological correlation; no widely accepted diagnostic criteria are present for the pathological diagnosis of HIE. HIE cases showed consistent evidence of diffuse white matter gliosis, as evaluated by the qualitative increase in the number of GFAP-positive cells in addition to the increased intensity of GFAP staining. For immunostaining of

reactive astrocyte markers, tissue slides were bleached with UV overnight, rinsed with PBS for 10 minutes, incubated with blocking solution (10% normal goat serum + 0.2% Triton X-100 in PBS) for 1 hour at room temperature, and then incubated with the following primary antibodies overnight at 4 °C: mouse anti-C3 (1:200 dilution; Biolegend cat. no. 846302) + rabbit anti-GFAP (1:500 dilution; Agilent Dako cat. no. Z0334), or mouse anti-GFAP (1:500 dilution; Milipore Sigma cat. no. G3893) + rabbit anti-VCAM1 (1:200 dilution; Abcam cat. no. ab134047). Afterwards, the samples were rinsed three times with PBS + 0.2% Triton X-100 for 10 minutes each time, and then incubated with secondary antibodies for 1 hour at room temperature in the dark.

Data analysis

Pooled CRISPRi screens

We analyzed the data from the pooled CRISPRi screens using the MAGeCK-iNC bioinformatic pipeline previously described in Tian *et al.*⁸³.

Master regulator analysis (MRA)

To collect human astrocyte RNA-seq data for co-expression network reconstruction, we downloaded gene-level counts from samples annotated as “Astrocyte” in ARCHS4⁹⁰. For published human astrocyte RNA-seq datasets not found in ARCHS4, we manually downloaded FASTQ files from GEO, and then processed the FASTQ data using Elysium⁹¹, which implements the alignment pipeline used in ARCHS4. In addition to published human astrocyte RNA-seq datasets, we also used Elysium to process additional human astrocyte RNA-seq datasets from our labs (Ye Zhang lab, UCLA³⁵, and Kampmann lab; all datasets used for MRA available at <https://kampmannlab.ucsf.edu/inflammatory-reactive-astrocyte-analysis>). We merged the gene-level count matrices from the above sources into a single matrix, which was

then used for MRA (see Supplementary Table 11 for the metadata corresponding to all samples used for co-expression network reconstruction). Batch correction was first performed across datasets using ComBat-seq⁹², which is a part of the R (version 4.0.3) package “sva” (version 3.38.0). Gene-level counts were then transformed to log-scale using the variance-stabilizing transformation in DESeq2 (version 1.30.1). A list of human transcription factors (TFs) was obtained from Lambert *et al.*³⁶, and a list of human kinases and phosphatases was obtained from Manning *et al.*³⁷ and Liberti *et al.*³⁸. Genes and regulators (TFs, kinases and phosphatases) with low expression in hiPSC-derived astrocytes used in our study (mean transcripts per million < 1) were removed from the matrix. MRA was then performed using the R package “RTN” (version 2.16.0)³²⁻³⁴, following the RTN vignette available on Bioconductor.

CROP-seq

Alignment and quantification were performed on 10X single-cell RNA-seq libraries and sgRNA-enriched libraries using Cell Ranger (version 5.0.1) with default parameters and reference genome GRCh38-3.0.0. Cellranger aggr was used to aggregate counts belonging to the same sample across different GEM wells. sgRNA unique molecular identifier (UMI) counts for each cell barcode were obtained using the pipeline described in Hill *et al.*⁹³. sgRNAs were assigned to cells using demuxEM⁹⁴. The gene vs. cell barcode matrix outputted by Cell Ranger was converted into a SingleCellExperiment (SCE) object using the read10xCounts function from the DropletUtils R package (version 1.10.388). sgRNA assignments were appended to the SCE metadata and filtered to only include cells with a single sgRNA. The SCE object was then converted into a Seurat object for subsequent analysis. Data normalization, log-transformation, and identification of highly variable genes were performed using Seurat::SCTransform⁹⁵.

For exploratory analysis of the effect of knocking down each regulator targeted in the CROP-seq experiment, a separate Seurat object was created for each regulator consisting of iAstrocytes transduced with a non-targeting (NTC) sgRNA and iAstrocytes transduced with the

sgRNA targeting that regulator. For each of these Seurat objects, the data was renormalized with SCTransform, dimensionality reduction was performed with Seurat::RunPCA (30 PC's retained) and Seurat::RunUMAP, and clustering was performed with Seurat::FindNeighbors and Seurat::FindClusters (resolution = 0.5). Regulators whose knockdown resulted in clear spatial separation between knockdown iAstrocytes and NTC iAstrocytes in UMAP were selected for further analysis. The PCA embeddings from the Seurat objects corresponding to the selected regulators were used for aligned UMAP⁹⁶, which allows the effect of knocking down different regulators to be visualized in the same UMAP embedding. This aligned UMAP embedding was used for Fig. 3.4a,b,d and Fig. 3.5c, which displayed only NTC iAstrocytes. Markers of IRAS1 and IRAS2 in NTC iAstrocytes were identified by performing Student's t-tests on the Pearson residuals from SCTransform using Seurat::FindMarkers.

To find genes whose differential expression induced by IL-1 α +TNF+C1q treatment was changed by regulator knockdown, we used the R package limma (version 3.46.0) to perform linear regression on the Pearson residuals from running SCTransform on the Seurat object containing all iAstrocytes assigned with a single sgRNA. We used the design formula $y \sim \text{regulatorKnockdown} + \text{cytokineTreatment} + \text{regulatorKnockdown}:\text{cytokineTreatment}$, where the interaction term $\text{regulatorKnockdown}:\text{cytokineTreatment}$ reflects the effect of knocking down a given regulator on the differential expression induced by IL-1 α +TNF+C1q treatment. For each regulator knockdown, genes with a statistically significant interaction term were extracted for the analysis presented in Fig. S3.4d-e.

To construct the heatmap in Fig. S3.4e, the log₂-fold-change (LFC) values of the above DEGs were weighted by their associated multiple testing-corrected P -values (P_{adj}) to generate a gene score, where $\text{gene score} = \text{LFC} * (1 - P_{\text{adj}})$. Hierarchical clustering (Ward's method) was then performed on both the rows (genes) and columns (regulators) of the gene score matrix,

using Pearson correlation as the distance metric. The heatmap was drawn using R package ComplexHeatmap (version 2.6.2)⁹⁷.

Integration of iAstrocyte single-cell RNA-seq data with external single-cell RNA-seq datasets

UMI count matrices of single-cell RNA-seq data from Barbar *et al.*²⁶ were downloaded from Synapse (syn21861229). Processed single-cell RNA-seq data objects corresponding to data from Wheeler *et al.*⁶⁶ were requested from Zhaorong Li and Michael Wheeler. UMI count matrices of single-cell RNA-seq data from Hasel *et al.*⁵² were downloaded from GEO (GSE148611). Integration of NTC iAstrocytes from the CROP-seq experiment with the above previously published single-cell RNA-seq datasets was performed by first renormalizing each dataset with Seurat::SCTransform and re-running Seurat::RunPCA, then selecting features for integration using Seurat::SelectIntegrationFeatures (nfeatures = 3000) and Seurat::PrepSCTIntegration, and then performing data integration using reciprocal PCA with Seurat::FindIntegrationAnchors (normalization.method = 'SCT', reduction = 'rpca') and Seurat::IntegrateData (normalization.method = 'SCT'), using NTC iAstrocytes as the reference dataset. The integrated PCA embeddings were then used for clustering (resolution = 0.4) and UMAP. For integration with Barbar *et al.*²⁶, the k.anchor parameter of Seurat::FindAnchors was set to 20; for Wheeler *et al.*⁶⁶, k.anchor was set to 50; for Hasel *et al.*⁵², k.anchor was set to 100. Seurat::AddModuleScore was used to generate module expression scores for IRAS1 vs. IRAS2 markers in astrocytes from external single-cell datasets.

Bulk RNA-seq of hiPSC-derived astrocytes generated in this study

Alignment and quantification were performed using Salmon (version 1.4.082), with the --noLengthCorrection flag and an index generated from the human transcriptome (GRCh38, Gencode release 37). The R package Tximport (version 1.18.083) was used to obtain gene-

level count estimates. Genes with zero counts across all samples were removed from the analysis. Differential gene expression analysis was performed with DESeq2 (version 1.30.1).

Reanalysis of external bulk RNA-seq datasets

For Guttenplan *et al.*⁹, we downloaded the table of DEGs induced by IL-1 α +TNF+C1q in immunopanned astrocytes from wild-type mice provided in GSE143598. We used BioJupies⁹⁸ to reanalyze bulk RNA-seq data and obtain differentially expressed genes from Perriot *et al.*⁹⁹ (GSE120411; hiPSC-derived astrocytes treated with IL1 α +TNF), Barbar *et al.*²⁶ (syn21861229; CD49f+ astrocytes sorted from cerebral organoids treated with vehicle control or IL-1 α +TNF+C1q), and Anderson *et al.*⁴⁵ (GSE76097; astrocyte-specific RNA from *Stat3* cKO vs. wild-type mice subject to spinal cord injury). For Anderson *et al.*, sample GSM1974209 was removed because it was an outlier in PCA visualization of the samples.

Pathway enrichment analysis

We used Enrichr¹⁰⁰⁻¹⁰² to perform enrichment analysis of gene lists. For display of enrichment results against the TRRUST gene set library, terms corresponding to mouse gene sets were removed for genes lists derived from human astrocytes; for genes lists derived from mouse astrocytes, terms corresponding to human gene sets were removed.

Flow cytometry

Data from flow cytometry experiments were analyzed using FlowJo (version 10.7.1). Live cells were gated by plotting SSC-A vs. FSC-A and then single cells were gated by plotting FSC-H vs. FSC-A. For experiments involving CRISPRi knockdown, analysis was restricted to sgRNA-transduced cells (gating on the histogram of BFP fluorescence values). For antibody staining

experiments where median fluorescence intensity (MFI) values were reported, the average MFI of unstained control samples were subtracted from the MFI of stained samples.

Image segmentation and analysis

We used CellProfiler (v3.15)¹⁰³ to segment and quantify neuron viability, neuron GCaMP recordings, and iAstrocyte immunostaining images. For neuron viability, monochrome images of Hoechst and TO-PRO3 were segmented to nuclei and TO-PRO3+ objects, respectively; TO-PRO3+ neurons (i.e. dead neurons) were determined by overlap of nuclei with TO-PRO3+ objects using the RelateObjects module in CellProfiler. For neuron GCaMP recordings, neuronal soma were segmented on the maximum intensity projection of all GCaMP images in the recording, nuclei were segmented on a single BFP image collected at the end of recording, and only nuclei that were contained within a GCaMP+ soma were retained using the RelatedObjects and FilterObjects modules in CellProfiler. The median GCaMP intensity per soma at each time point was then extracted for analysis. For each neuronal soma, ΔF was calculated as $F_t - F_{t-1}$ and F_0 was calculated as the average of a 10-second rolling window around F_t .

For iAstrocyte immunostaining, the total image intensity of GFAP, S100 β , GLAST, and NFIA was calculated and divided by the total image intensity of Hoechst to normalize for cell number. For analysis of images from immunostaining of human neuropathological tissue, monochrome images of DAPI, VCAM1, C3, and GFAP staining were converted to probability maps of nuclei, VCAM1+ objects, C3+ objects, and GFAP+ objects respectively using ilastik¹⁰⁴; annotations for representative nuclei, VCAM1+ objects, C3+ objects, and GFAP+ objects were inputted manually to train the classifier. The probability maps were then inputted into CellProfiler to segment nuclei, VCAM1+ objects, C3+ objects, and astrocytes (defined as nuclei-containing GFAP+ objects), and the VCAM1 or C3 staining status of astrocytes was determined by overlap of astrocytes with VCAM1+ or C3+ objects using the RelateObjects module in CellProfiler.

Statistics and reproducibility

Sample sizes were determined by referencing existing studies in the field. Major findings were validated using independent samples and orthogonal approaches. Numbers of replicates are listed in each figure. Randomization was not relevant to our study because no animals or human subjects were involved.

REFERENCES

1. Sofroniew, M.V. & Vinters, H.V. Astrocytes: biology and pathology. *Acta Neuropathol* **119**, 7-35 (2010).
2. Escartin, C., *et al.* Reactive astrocyte nomenclature, definitions, and future directions. *Nat Neurosci* **24**, 312-325 (2021).
3. Wang, Q., Tang, X.N. & Yenari, M.A. The inflammatory response in stroke. *J Neuroimmunol* **184**, 53-68 (2007).
4. Hausmann, O.N. Post-traumatic inflammation following spinal cord injury. *Spinal Cord* **41**, 369-378 (2003).
5. Ponath, G., Park, C. & Pitt, D. The Role of Astrocytes in Multiple Sclerosis. *Front Immunol* **9**, 217 (2018).
6. Heneka, M.T., *et al.* Neuroinflammation in Alzheimer's disease. *Lancet Neurol* **14**, 388-405 (2015).
7. Han, R.T., Kim, R.D., Molofsky, A.V. & Liddelow, S.A. Astrocyte-immune cell interactions in physiology and pathology. *Immunity* **54**, 211-224 (2021).
8. Liddelow, S.A., *et al.* Neurotoxic reactive astrocytes are induced by activated microglia. *Nature* **541**, 481-487 (2017).
9. Guttenplan, K.A., *et al.* Knockout of reactive astrocyte activating factors slows disease progression in an ALS mouse model. *Nat Commun* **11**, 3753 (2020).
10. Guttenplan, K.A., *et al.* Neurotoxic Reactive Astrocytes Drive Neuronal Death after Retinal Injury. *Cell Rep* **31**, 107776 (2020).
11. Yun, S.P., *et al.* Block of A1 astrocyte conversion by microglia is neuroprotective in models of Parkinson's disease. *Nat Med* **24**, 931-938 (2018).
12. Clarke, L.E., *et al.* Normal aging induces A1-like astrocyte reactivity. *Proc Natl Acad Sci U S A* **115**, E1896-E1905 (2018).
13. Herrmann, J.E., *et al.* STAT3 is a critical regulator of astrogliosis and scar formation after spinal cord injury. *J Neurosci* **28**, 7231-7243 (2008).
14. Liu, Z., *et al.* Beneficial effects of gfap/vimentin reactive astrocytes for axonal remodeling and motor behavioral recovery in mice after stroke. *Glia* **62**, 2022-2033 (2014).
15. Krencik, R. & Zhang, S.C. Directed differentiation of functional astroglial subtypes from human pluripotent stem cells. *Nat Protoc* **6**, 1710-1717 (2011).
16. Zamanian, J.L., *et al.* Genomic analysis of reactive astrogliosis. *J Neurosci* **32**, 6391-6410 (2012).
17. Kampmann, M. CRISPR-based functional genomics for neurological disease. *Nat Rev Neurol* **16**, 465-480 (2020).

18. Tcw, J., *et al.* An Efficient Platform for Astrocyte Differentiation from Human Induced Pluripotent Stem Cells. *Stem Cell Reports* **9**, 600-614 (2017).
19. Li, X., *et al.* Fast Generation of Functional Subtype Astrocytes from Human Pluripotent Stem Cells. *Stem Cell Reports* **11**, 998-1008 (2018).
20. Abbott, N.J. Astrocyte-endothelial interactions and blood-brain barrier permeability. *J Anat* **200**, 629-638 (2002).
21. Allen, N.J. & Eroglu, C. Cell Biology of Astrocyte-Synapse Interactions. *Neuron* **96**, 697-708 (2017).
22. Verstraelen, P., *et al.* Pharmacological characterization of cultivated neuronal networks: relevance to synaptogenesis and synaptic connectivity. *Cell Mol Neurobiol* **34**, 757-776 (2014).
23. Nakanishi, K., *et al.* Astrocytic contribution to functioning synapse formation estimated by spontaneous neuronal intracellular Ca²⁺ oscillations. *Brain Res* **659**, 169-178 (1994).
24. Allen, N.J., *et al.* Astrocyte glypicans 4 and 6 promote formation of excitatory synapses via GluA1 AMPA receptors. *Nature* **486**, 410-414 (2012).
25. Körber, N. & Stein, V. In vivo imaging demonstrates dendritic spine stabilization by SynCAM 1. *Sci Rep* **6**, 24241 (2016).
26. Barbar, L., *et al.* CD49f Is a Novel Marker of Functional and Reactive Human iPSC-Derived Astrocytes. *Neuron* **107**, 436-453.e412 (2020).
27. Williams, J.L., *et al.* Astrocyte-T cell crosstalk regulates region-specific neuroinflammation. *Glia* **68**, 1361-1374 (2020).
28. Gimenez, M.A., Sim, J.E. & Russell, J.H. TNFR1-dependent VCAM-1 expression by astrocytes exposes the CNS to destructive inflammation. *J Neuroimmunol* **151**, 116-125 (2004).
29. Rosenman, S.J., Shrikant, P., Dubb, L., Benveniste, E.N. & Ransohoff, R.M. Cytokine-induced expression of vascular cell adhesion molecule-1 (VCAM-1) by astrocytes and astrocytoma cell lines. *J Immunol* **154**, 1888-1899 (1995).
30. Rubio, N., Sanz-Rodriguez, F. & Arevalo, M.A. Up-regulation of the vascular cell adhesion molecule-1 (VCAM-1) induced by Theiler's murine encephalomyelitis virus infection of murine brain astrocytes. *Cell Commun Adhes* **17**, 57-68 (2010).
31. Kampmann, M. CRISPRi and CRISPRa Screens in Mammalian Cells for Precision Biology and Medicine. *ACS Chem Biol* **13**, 406-416 (2018).
32. Castro, M.A., *et al.* Regulators of genetic risk of breast cancer identified by integrative network analysis. *Nat Genet* **48**, 12-21 (2016).
33. Fletcher, M.N., *et al.* Master regulators of FGFR2 signalling and breast cancer risk. *Nat Commun* **4**, 2464 (2013).
34. Campbell, T.M., *et al.* FGFR2 risk SNPs confer breast cancer risk by augmenting oestrogen responsiveness. *Carcinogenesis* **37**, 741-750 (2016).

35. Krawczyk, M.C., *et al.* Human Astrocytes Exhibit Tumor Microenvironment-, Age-, and Sex-Related Transcriptomic Signatures. *bioRxiv*, 2021.2002.2025.432948 (2021).
36. Lambert, S.A., *et al.* The Human Transcription Factors. *Cell* **172**, 650-665 (2018).
37. Manning, G., Whyte, D.B., Martinez, R., Hunter, T. & Sudarsanam, S. The protein kinase complement of the human genome. *Science* **298**, 1912-1934 (2002).
38. Liberti, S., *et al.* HuPho: the human phosphatase portal. *FEBS J* **280**, 379-387 (2013).
39. Horlbeck, M.A., *et al.* Compact and highly active next-generation libraries for CRISPR-mediated gene repression and activation. *Elife* **5** (2016).
40. Shih, V.F., Tsui, R., Caldwell, A. & Hoffmann, A. A single NF κ B system for both canonical and non-canonical signaling. *Cell Res* **21**, 86-102 (2011).
41. Basak, S., *et al.* A fourth I κ B protein within the NF- κ B signaling module. *Cell* **128**, 369-381 (2007).
42. Liu, T., Zhang, L., Joo, D. & Sun, S.C. NF- κ B signaling in inflammation. *Signal Transduct Target Ther* **2** (2017).
43. Cardinaux, J.R., Allaman, I. & Magistretti, P.J. Pro-inflammatory cytokines induce the transcription factors C/EBP β and C/EBP δ in astrocytes. *Glia* **29**, 91-97 (2000).
44. Alonzi, T., *et al.* Essential role of STAT3 in the control of the acute-phase response as revealed by inducible gene inactivation [correction of activation] in the liver. *Mol Cell Biol* **21**, 1621-1632 (2001).
45. Anderson, M.A., *et al.* Astrocyte scar formation aids central nervous system axon regeneration. *Nature* **532**, 195-200 (2016).
46. Ben Haim, L., *et al.* The JAK/STAT3 pathway is a common inducer of astrocyte reactivity in Alzheimer's and Huntington's diseases. *J Neurosci* **35**, 2817-2829 (2015).
47. Wang, Z.H., *et al.* C/EBP β regulates delta-secretase expression and mediates pathogenesis in mouse models of Alzheimer's disease. *Nat Commun* **9**, 1784 (2018).
48. Strohmeyer, R., Shelton, J., Loughheed, C. & Breitkopf, T. CCAAT-enhancer binding protein- β expression and elevation in Alzheimer's disease and microglial cell cultures. *PLoS One* **9**, e86617 (2014).
49. Feng, H., Zhang, Y.B., Gui, J.F., Lemon, S.M. & Yamane, D. Interferon regulatory factor 1 (IRF1) and anti-pathogen innate immune responses. *PLoS Pathog* **17**, e1009220 (2021).
50. Lehtonen, A., Matikainen, S. & Julkunen, I. Interferons up-regulate STAT1, STAT2, and IRF family transcription factor gene expression in human peripheral blood mononuclear cells and macrophages. *J Immunol* **159**, 794-803 (1997).
51. Ng, S.L., *et al.* I κ B kinase epsilon (IKK(ϵ)) regulates the balance between type I and type II interferon responses. *Proc Natl Acad Sci U S A* **108**, 21170-21175 (2011).

52. Hasel, P., Rose, I.V.L., Sadick, J.S., Kim, R.D. & Liddelov, S.A. Neuroinflammatory astrocyte subtypes in the mouse brain. *Nat Neurosci* (2021).
53. Gan, W., *et al.* LATS suppresses mTORC1 activity to directly coordinate Hippo and mTORC1 pathways in growth control. *Nat Cell Biol* **22**, 246-256 (2020).
54. He, L., *et al.* mTORC1 Promotes Metabolic Reprogramming by the Suppression of GSK3-Dependent Foxk1 Phosphorylation. *Mol Cell* **70**, 949-960.e944 (2018).
55. Datlinger, P., *et al.* Pooled CRISPR screening with single-cell transcriptome readout. *Nat Methods* **14**, 297-301 (2017).
56. Banks, T.A., *et al.* A lymphotoxin-IFN-beta axis essential for lymphocyte survival revealed during cytomegalovirus infection. *J Immunol* **174**, 7217-7225 (2005).
57. Weichhart, T., Hengstschläger, M. & Linke, M. Regulation of innate immune cell function by mTOR. *Nat Rev Immunol* **15**, 599-614 (2015).
58. Balamurugan, K., *et al.* The tumour suppressor C/EBP δ inhibits FBXW7 expression and promotes mammary tumour metastasis. *EMBO J* **29**, 4106-4117 (2010).
59. Heinrich, P.C., Castell, J.V. & Andus, T. Interleukin-6 and the acute phase response. *Biochem J* **265**, 621-636 (1990).
60. Sonderegger, I., *et al.* GM-CSF mediates autoimmunity by enhancing IL-6-dependent Th17 cell development and survival. *J Exp Med* **205**, 2281-2294 (2008).
61. Metzemaekers, M., Vanheule, V., Janssens, R., Struyf, S. & Proost, P. Overview of the Mechanisms that May Contribute to the Non-Redundant Activities of Interferon-Inducible CXC Chemokine Receptor 3 Ligands. *Front Immunol* **8**, 1970 (2017).
62. Wang, Y., van Boxel-Dezaire, A.H., Cheon, H., Yang, J. & Stark, G.R. STAT3 activation in response to IL-6 is prolonged by the binding of IL-6 receptor to EGF receptor. *Proc Natl Acad Sci U S A* **110**, 16975-16980 (2013).
63. Au-Yeung, N., Mandhana, R. & Horvath, C.M. Transcriptional regulation by STAT1 and STAT2 in the interferon JAK-STAT pathway. *JAKSTAT* **2**, e23931 (2013).
64. Hungness, E.S., *et al.* Transcription factors C/EBP-beta and -delta regulate IL-6 production in IL-1beta-stimulated human enterocytes. *J Cell Physiol* **192**, 64-70 (2002).
65. Stuart, T., *et al.* Comprehensive Integration of Single-Cell Data. *Cell* **177**, 1888-1902.e1821 (2019).
66. Wheeler, M.A., *et al.* MAFG-driven astrocytes promote CNS inflammation. *Nature* **578**, 593-599 (2020).
67. Heppner, F.L., Ransohoff, R.M. & Becher, B. Immune attack: the role of inflammation in Alzheimer disease. *Nat Rev Neurosci* **16**, 358-372 (2015).

68. Eikelenboom, P., Hack, C.E., Rozemuller, J.M. & Stam, F.C. Complement activation in amyloid plaques in Alzheimer's dementia. *Virchows Arch B Cell Pathol Incl Mol Pathol* **56**, 259-262 (1989).
69. Abraham, C.R., Selkoe, D.J. & Potter, H. Immunochemical identification of the serine protease inhibitor alpha 1-antichymotrypsin in the brain amyloid deposits of Alzheimer's disease. *Cell* **52**, 487-501 (1988).
70. Habib, N., *et al.* Disease-associated astrocytes in Alzheimer's disease and aging. *Nat Neurosci* **23**, 701-706 (2020).
71. Liu, F. & McCullough, L.D. Inflammatory responses in hypoxic ischemic encephalopathy. *Acta Pharmacol Sin* **34**, 1121-1130 (2013).
72. Reichenbach, N., *et al.* Inhibition of Stat3-mediated astrogliosis ameliorates pathology in an Alzheimer's disease model. *EMBO Mol Med* **11** (2019).
73. Clarke, P., Zhuang, Y., Berens, H.M., Leser, J.S. & Tyler, K.L. Interferon Beta Contributes to Astrocyte Activation in the Brain following Reovirus Infection. *J Virol* **93** (2019).
74. Sanmarco, L.M., *et al.* Gut-licensed IFN γ . *Nature* **590**, 473-479 (2021).
75. Rothhammer, V., *et al.* Type I interferons and microbial metabolites of tryptophan modulate astrocyte activity and central nervous system inflammation via the aryl hydrocarbon receptor. *Nat Med* **22**, 586-597 (2016).
76. Hindinger, C., *et al.* IFN- γ signaling to astrocytes protects from autoimmune mediated neurological disability. *PLoS One* **7**, e42088 (2012).
77. Miyaoka, Y., *et al.* Isolation of single-base genome-edited human iPS cells without antibiotic selection. *Nat Methods* **11**, 291-293 (2014).
78. Tian, R., *et al.* CRISPR Interference-Based Platform for Multimodal Genetic Screens in Human iPSC-Derived Neurons. *Neuron* **104**, 239-255 e212 (2019).
79. Li, X.L., *et al.* Highly efficient genome editing via CRISPR-Cas9 in human pluripotent stem cells is achieved by transient BCL-XL overexpression. *Nucleic Acids Res* **46**, 10195-10215 (2018).
80. Cheng, C., Fass, D.M., Folz-Donahue, K., MacDonald, M.E. & Haggarty, S.J. Highly Expandable Human iPS Cell-Derived Neural Progenitor Cells (NPC) and Neurons for Central Nervous System Disease Modeling and High-Throughput Screening. *Curr Protoc Hum Genet* **92**, 21.28.21-21.28.21 (2017).
81. Gilbert, L.A., *et al.* Genome-Scale CRISPR-Mediated Control of Gene Repression and Activation. *Cell* **159**, 647-661 (2014).
82. Neal, E.H., *et al.* A Simplified, Fully Defined Differentiation Scheme for Producing Blood-Brain Barrier Endothelial Cells from Human iPSCs. *Stem Cell Reports* **12**, 1380-1388 (2019).

83. Fernandopulle, M.S., *et al.* Transcription Factor-Mediated Differentiation of Human iPSCs into Neurons. *Curr Protoc Cell Biol* **79**, e51 (2018).
84. Niu, J., *et al.* Oligodendroglial ring finger protein Rnf43 is an essential injury-specific regulator of oligodendrocyte maturation. *Neuron* (2021).
85. Lachmann, A., *et al.* Massive mining of publicly available RNA-seq data from human and mouse. *Nat Commun* **9**, 1366 (2018).
86. Lachmann, A., Xie, Z. & Ma'ayan, A. Elysium: RNA-seq Alignment in the Cloud. *bioRxiv*, 382937 (2018).
87. Zhang, Y., Parmigiani, G. & Johnson, W.E.: batch effect adjustment for RNA-seq count data. *NAR Genom Bioinform* **2**, lqaa078 (2020).
88. Hill, A.J., *et al.* On the design of CRISPR-based single-cell molecular screens. *Nat Methods* **15**, 271-274 (2018).
89. Gaublomme, J.T., *et al.* Nuclei multiplexing with barcoded antibodies for single-nucleus genomics. *Nat Commun* **10**, 2907 (2019).
90. Hafemeister, C. & Satija, R. Normalization and variance stabilization of single-cell RNA-seq data using regularized negative binomial regression. *Genome Biol* **20**, 296 (2019).
91. McInnes, L., Healy, J. & Melville, J. UMAP: Uniform Manifold Approximation and Projection for Dimension Reduction. *arXiv*, 1802.03426 (2020).
92. Gu, Z., Eils, R. & Schlesner, M. Complex heatmaps reveal patterns and correlations in multidimensional genomic data. *Bioinformatics* **32**, 2847-2849 (2016).
93. Torre, D., Lachmann, A. & Ma'ayan, A. BioJupies: Automated Generation of Interactive Notebooks for RNA-Seq Data Analysis in the Cloud. *Cell Syst* **7**, 556-561.e553 (2018).
94. Perriot, S., *et al.* Human Induced Pluripotent Stem Cell-Derived Astrocytes Are Differentially Activated by Multiple Sclerosis-Associated Cytokines. *Stem Cell Reports* **11**, 1199-1210 (2018).
95. Chen, E.Y., *et al.* Enrichr: interactive and collaborative HTML5 gene list enrichment analysis tool. *BMC Bioinformatics* **14**, 128 (2013).
96. Kuleshov, M.V., *et al.* Enrichr: a comprehensive gene set enrichment analysis web server 2016 update. *Nucleic Acids Res* **44**, W90-97 (2016).
97. Xie, Z., *et al.* Gene Set Knowledge Discovery with Enrichr. *Curr Protoc* **1**, e90 (2021).
98. McQuin, C., *et al.* CellProfiler 3.0: Next-generation image processing for biology. *PLoS Biol* **16**, e2005970 (2018).
99. Berg, S., *et al.* ilastik: interactive machine learning for (bio)image analysis. *Nat Methods* **16**, 1226-1232 (2019).

100. Liberzon, A., *et al.* The Molecular Signatures Database (MSigDB) hallmark gene set collection. *Cell Syst* **1**, 417-425 (2015).
101. Han, H., *et al.* TRRUST v2: an expanded reference database of human and mouse transcriptional regulatory interactions. *Nucleic Acids Res* **46**, D380-D386 (2018).
102. Kelley, K.W., Nakao-Inoue, H., Molofsky, A.V. & Oldham, M.C. Variation among intact tissue samples reveals the core transcriptional features of human CNS cell classes. *Nat Neurosci* **21**, 1171-1184 (2018).
103. Huang, R., *et al.* The NCATS BioPlanet - An Integrated Platform for Exploring the Universe of Cellular Signaling Pathways for Toxicology, Systems Biology, and Chemical Genomics. *Front Pharmacol* **10**, 445 (2019).
104. Cao, J., *et al.* A human cell atlas of fetal gene expression. *Science* **370** (2020).

Chapter 4

mTOR controls neurotoxic lysosome exocytosis in inflammatory reactive astrocytes

This chapter is a manuscript in submission and is reproduced from the following preprint:

Rooney B.*, **Leng K.***, McCarthy F., Rose I.L.V., Herrington K.A., Bax S., Chin M.Y., Fathi S., Leonetti M., Kao A.W., Elias J.E. & Kampmann M. mTOR controls neurotoxic lysosome exocytosis in inflammatory reactive astrocytes. *bioRxiv*. <https://doi.org/10.1101/2021.09.11.459904>.

*Co-first authorship

ABSTRACT

Inflammatory reactive astrocytes lose homeostatic functions and can be neurotoxic, potentially contributing to neurodegenerative diseases. However, the underlying cell biological mechanisms are not fully understood. Here, we demonstrate that lysosomes are remodeled and alkalized in inflammatory reactive astrocytes, and that lysosome exocytosis drives astrocyte-mediated neurotoxicity. CRISPRi screens uncover mTOR as a regulator of neurotoxic lysosome exocytosis. These results pinpoint lysosome remodeling and exocytosis in inflammatory reactive astrocytes as a potential therapeutic target.

MAIN

Reactive astrocytes are prevalent in many neurodegenerative diseases¹⁰⁵. Mounting evidence suggests that inflammatory reactive astrocytes contribute to disease progression by losing their normal homeostatic functions and secreting factors that are neurotoxic under certain conditions^{2,8,105,106}. However, the mechanisms that drive these functional changes in inflammatory reactive astrocytes remain unknown.

To identify the cellular pathways responsible for the functional changes that accompany inflammatory astrocyte reactivity, we re-analyzed our previously collected RNA-sequencing dataset of hiPSC-derived astrocytes (iAstrocytes)¹⁰⁷ treated with the microglia-derived cytokines IL1 α , TNF, and C1q (hereafter referred to as ITC) which induce inflammatory reactivity *in vitro*⁸ (**Fig. 4.1a**). As expected, many genes and pathways previously associated with inflammatory astrocyte reactivity^{2,16,108} were upregulated after ITC treatment, including *SERPINA3* and *C3*, along with cellular pathways involved in NF- κ B signaling, antigen presentation, and cellular response to cytokines. Interestingly, many genes encoding lysosome-localized proteins were downregulated after ITC treatment (**Fig. 4.1b-c**). These included many subunits of the vacuolar ATPase (V-ATPase) complex and lysosomal degradative enzymes, which coordinate the proper

acidification of lysosomes and hydrolysis of autophagic substrates (**Fig. 4.1c**). We validated that many of these genes were also downregulated at the protein level in ITC-treated iAstrocytes via proteomics (**Fig. S4.1a,b**). Further analysis of published RNA-sequencing datasets of hiPSC-derived reactive astrocytes confirmed that this lysosomal signature was broadly conserved across models of inflammatory reactivity (**Fig. 4.1c**), including those that use different differentiation protocols (Barbar *et al.*)¹⁰⁶ and cytokine treatments (Perriot *et al.*)¹⁰⁹. We also noted that a small subset of genes encoding lysosome-localized proteins involved in antigen presentation and inflammation (e.g. *CTSS*, *HLA* family) were strongly upregulated across models (**Fig. 4.1c**).

To determine if this lysosome signature is associated with changes in lysosome levels and function in inflammatory reactive astrocytes, we quantified levels of the lysosomal marker LAMP2 by immunoblotting, and found no significant difference after ITC treatment (**Fig. 4.1d**). Similarly, quantification of the lysosomal markers LAMP1 and LAMP2 by immunofluorescence did not show significant changes in response to ITC (**Fig. 4.1e**). However, there was a dramatic decrease in the fluorescent signal of LysoTracker Green, a cell-permeable, pH-dependent dye that accumulates in lysosomes (**Fig. 4.1e**). We hypothesized that ITC-treated iAstrocytes were deficient in lysosomal acidification, thereby preventing LysoTracker from accumulating in lysosomes. Using the genetically encoded lysosome pH sensor FIRE-pHLy¹¹⁰, we found that the lysosomes of ITC-treated iAstrocytes were indeed less acidic than those of control iAstrocytes (**Fig. 4.1f**). Furthermore, ITC-treated iAstrocytes accumulated puncta of LC3B, an autophagosome marker degraded in the lysosome by acid-activated hydrolases (**Fig. 4.1e**). Using a GFP-LC3-RFP-LC3ΔG reporter¹¹¹, we verified that this accumulation in ITC-treated iAstrocytes reflected an impairment in degradative autophagic flux rather than an increase in the steady-state level of autophagic components (**Fig. 4.1g**).

To gain a more detailed understanding of lysosome remodeling in inflammatory reactive astrocytes, we investigated the lysosomal proteome by immunoprecipitating a LAMP1-3xHA

lysosome tag (lyso-IP)¹¹² introduced into iAstrocytes via lentiviral transduction (**Fig. 4.1h**, **Fig. S4.1c,d**). In agreement with our RNA-sequencing and whole-cell proteomics data, we found that many proteins required for lysosomal degradation, including V-ATPase subunits and lysosomal hydrolases, were less abundant in the lyso-IP fraction of ITC-treated iAstrocytes compared to vehicle-treated iAstrocytes (**Fig. 4.1i**). We also found that CST3, a potent inhibitor of lysosomal proteinases, was highly enriched in the lyso-IP fraction of ITC-treated iAstrocytes. In addition to the above signature of decreased degradative capacity, we found that several mediators of inflammatory signaling – CCL2, TNFAIP3, and IL32 – were more enriched in the lyso-IP fraction compared to whole-cell proteomics in ITC-treated vs. vehicle-treated iAstrocytes (**Fig. 4.1j**). Given that IL32 has previously been reported to undergo likely lysosome-mediated secretion¹¹³ and that many proteins traditionally involved in exocytosis (eg. RAB11A, RAB27A, RAB3A) were enriched in the lyso-IP fraction upon ITC treatment (**Fig. 4.1i,j**), we hypothesized that inflammatory reactive astrocytes execute lysosome exocytosis, potentially as a mechanism to counteract the accumulation of autophagic substrates and/or as part of a non-canonical secretory pathway.

To test this hypothesis, we used TIRF microscopy to visualize lysosomes in iAstrocytes loaded with LysoTracker Green and expressing a lysosome membrane-targeted mCherry construct (**Fig. 4.2a**). Indeed, likely lysosome exocytosis events were observed as the trafficking of mCherry+/LysoTracker+ vesicles to the plasma membrane followed by an uncoupling of the mCherry and LysoTracker signals upon contact with the plasma membrane, after which the LysoTracker signal rapidly diffused, while the mCherry signal remained at the cell surface, suggesting the ejection of lysosomal contents (**Fig. 4.2a-b**).

As an alternative and scalable approach to quantify lysosome exocytosis, we adopted a published flow cytometry-based protocol^{114,115} in which we stained non-permeabilized iAstrocytes with a fluorophore-conjugated antibody targeting a luminal epitope of LAMP1 that is exposed to the extracellular environment upon lysosome exocytosis (**Fig. S4.2a**). With this

approach, we found that ITC-treated iAstrocytes had almost twice the amount of cell-surface LAMP1 relative to vehicle-treated controls, despite equivalent levels of total LAMP1 protein between the two conditions (**Fig. 4.2c,d**). To test our hypothesis that the increased lysosome exocytosis in ITC-treated iAstrocytes was related to their deficit in lysosomal acidification, we treated iAstrocytes with bafilomycin A, a small molecule inhibitor of the V-ATPase complex. We observed a dose-dependent increase in lysosome exocytosis and concomitant decrease in lysosome acidification with increasing concentration of bafilomycin A (**Fig. 4.2e**). Together, these results suggest that lysosome remodeling involving decreased acidification and degradative capacity is associated with lysosome exocytosis in inflammatory reactive astrocytes.

Next, we turned our attention to understanding if lysosome exocytosis is involved in the known deleterious functions of inflammatory reactive astrocytes. Given that lysosome exocytosis contributes to the astrocyte secretome, we reasoned that lysosome exocytosis may play a role in the neurotoxicity of inflammatory reactive astrocytes. To test this hypothesis, we transferred astrocyte conditioned media (ACM) from vehicle-treated and ITC-treated iAstrocytes to hiPSC-derived neurons¹¹⁶ (iNeurons), and subsequently assayed the levels of both lysosome exocytosis (measured by cell-surface LAMP1 in the astrocytes) and neurotoxicity (measured using caspase 3/7 activity reporter dye in the ACM-receiving iNeurons) (**Fig. 4.2f**). Consistent with previous reports^{8,106}, the ITC-induced increase in cell-surface LAMP1 was mirrored by a strong increase in apoptosis in iNeurons receiving ACM derived from ITC-treated astrocytes (**Fig. 4.2g,h**). When we treated astrocytes with vacuolin-1, a small molecule inhibitor of lysosome exocytosis, there was a dose-dependent decrease in both lysosome exocytosis in astrocytes and apoptosis in iNeurons (**Fig. 4.2g**). Importantly, unconditioned media supplemented with ITC or vacuolin-1 did not substantially affect apoptosis in iNeurons, ruling out the possibility that residual amounts of these compounds were causing the apoptosis effects in ACM experiments (**Fig. S4.2b**). In addition, vacuolin-1 did not induce excess cell death in

iAstrocytes, ruling out the possibility that decreased astrocyte viability could explain the blunted neurotoxic activity (**Fig. S4.2c**). Furthermore, to confirm that vacuolin-1 specifically inhibited lysosome exocytosis in astrocytes and did not perturb general vesicular trafficking to the plasma membrane, we co-stained astrocytes with an antibody against TFRC, a constitutively expressed plasma membrane receptor. We found no substantial effect of vacuolin-1 on cell-surface TFRC levels (**Fig. S4.2d**). Lastly, we knocked down of genes reported to mediate lysosome exocytosis (*SYT11* and *VAMP7*)^{117,118}. While *SYT11* and *VAMP7* knockdown resulted in only a small decrease in cell-surface LAMP1, this was sufficient to reduce ITC-induced neurotoxicity by ~50% relative to control iAstrocytes (**Fig. 4.2i,j**).

To test if increasing lysosome exocytosis would also increase astrocyte-mediated neurotoxicity, we treated iAstrocytes receiving vehicle or ITC with a low dose of bafilomycin A (10 nM) to induce lysosome alkalization and lysosome exocytosis, and transferred the conditioned media to iNeurons as before. Bafilomycin A treatment resulted in a robust increase in cell-surface LAMP1 in both astrocytes treated with ITC or vehicle (**Fig. 4.2k**). Astrocytes treated with ITC and bafilomycin A were approximately twice as neurotoxic compared to astrocytes treated with ITC and DMSO (**Fig. 4.2l**). Interestingly, although bafilomycin A itself induced roughly the same level of lysosome exocytosis in vehicle-treated iAstrocytes as ITC-treated iAstrocytes, it did not cause a corresponding increase in neurotoxicity for iAstrocytes that were not treated with ITC, suggesting that ITC treatment alters the content of lysosomes in a way that increases neurotoxicity of lysosomal exocytosis. Neither ITC nor bafilomycin A (10 nM) induced apoptosis in iAstrocytes (**Fig. S4.2e**) or iNeurons (**Fig. S4.2f**). In summary, the above results suggest that lysosome exocytosis is a major mechanism underlying neurotoxicity of inflammatory reactive astrocytes.

To identify potential therapeutic targets to inhibit the lysosome alkalization-exocytosis-neurotoxicity axis in inflammatory reactive astrocytes, we performed targeted CRISPRi screens in iAstrocytes (**Fig. 4.3a**). Briefly, we transduced iAstrocytes expressing CRISPRi machinery¹⁰⁷

with a lentiviral sgRNA library targeting the “druggable genome”³⁹. After treating with ITC or vehicle control, we stained iAstrocytes with either LysoTracker or a fluorophore-conjugated LAMP1 antibody to monitor lysosomal alkalization and exocytosis, respectively, and used fluorescence-activated cell sorting (FACS) to collect sgRNA-transduced astrocytes with low or high levels of LysoTracker or LAMP1. We then conducted next-generation sequencing to identify sgRNAs that were over- or under-represented within their respective cell population relative to non-targeting control (NTC) sgRNAs (see Methods). Based on this analysis, we identified candidate regulators (FDR < 0.05, see Methods) of lysosomal pH (and also potentially mass; LysoTracker screen) or lysosome exocytosis (LAMP1 screen).

In agreement with our hypothesis that lysosomal alkalization drives lysosome exocytosis, we found a strong inverse correlation between the LysoTracker and LAMP1 phenotypes for many hit genes (**Fig. 4.3b, Fig. S4.3**). Across all screens, genes involved in mTOR signaling were highly enriched among hit genes, including *MTOR* itself as one of our strongest hits (**Fig. 4.3c,d**). To validate our screening results, we transduced iAstrocytes with an sgRNA targeting *MTOR* or a non-targeting sgRNA. As expected, *MTOR* knockdown dramatically increased LysoTracker staining (**Fig. 4.3e**). Importantly, *MTOR* knockdown specifically decreased lysosome exocytosis in ITC-treated but not vehicle-treated iAstrocytes (**Fig. 4.3f**), suggesting that mTOR activity may control lysosome exocytosis specifically in inflammatory reactive astrocytes. Consistent with our finding that suppressing lysosome exocytosis prevents inflammatory reactive astrocyte neurotoxicity, *MTOR* knockdown in iAstrocytes also rescued the neurotoxicity of ITC-treated iAstrocytes (**Fig. 4.3g**).

mTOR is a member of both mTORC1 and mTORC2 complexes, which regulate their downstream targets via phosphorylation¹¹⁹. Given that *MTOR* knockdown specifically blocked the ITC-induced increase of cell-surface LAMP1, we hypothesized that there would be increased mTOR activity in inflammatory reactive astrocytes. Immunoblots revealed that there were no significant changes in the levels of mTOR itself, but a clear trend towards increased

phosphorylation of mTORC1 targets (p-S6 S235/236 and p-ULK1 S757) and to a lesser extent mTORC2 targets (p-Akt S473) in ITC-treated iAstrocytes (**Fig. 4.3h-l**).

To validate that mTOR activity is responsible for lysosomal changes in inflammatory reactive astrocytes using an orthogonal approach, we treated iAstrocytes with several mTOR inhibitors, including the pan-mTOR inhibitor PP242, in combination with vehicle and ITC. We found that PP242 suppressed mTOR activity (**Fig. 4.3h**), acidified lysosomes (**Fig. 4.3m**), decreased cell-surface LAMP1 (**Fig. 4.3n**), and blocked ITC-induced neurotoxicity (**Fig. 4.3o**) in a dose-dependent manner.

In summary, we uncovered lysosome remodeling – consisting of increased lysosome pH, altered lysosomal content, and increased lysosome exocytosis – as a novel functional phenotype of inflammatory reactive astrocytes and a key pathological process mediating their neurotoxic activity. Furthermore, we used pooled CRISPRi screens to identify mTOR as a central upstream regulator of the lysosome alkalinization-exocytosis-neurotoxicity axis in inflammatory reactive astrocytes (**Fig. 4.3p**).

Our model is consistent with recent findings by other groups: First, *in vivo* reports that Lamp1 is the most strongly upregulated astrocyte cell-surface protein in a mouse model of multiple sclerosis (MS)¹²⁰. Second, the fact that mTOR inhibition blunts disease progression in mouse models of amyotrophic lateral sclerosis¹²¹ and MS¹²² that are driven by inflammatory reactive astrocytes. Last, *in vitro* data suggesting a role for astrocyte lysosome exocytosis in HIV-Tat-mediated neurotoxicity¹²³. Mechanistically, we have not yet resolved if the relationship between lysosome exocytosis and astrocyte-mediated neurotoxicity stems from direct toxicity of astrocyte lysosome contents, or whether these contents contribute to autocrine-paracrine signaling in astrocytes to induce neurotoxicity through an indirect mechanism (**Fig. 4.3p**).

We hope that future work will bring clarity to how lysosome remodeling in astrocytes influences neurodegenerative diseases, particularly with respect to the disease-, region-, and

context-specific functions of reactive astrocytes *in vivo*. Given our *in vitro* results, we envision that these studies could inform novel therapeutic approaches.

ACKNOWLEDGEMENTS

We thank Greg Mohl, Avi Samelson, Olivia Teter, Biswa Ramani, Brandon Desousa, Emmy Li, Vukasin Jovanovic, Zuzana Krejciova, and Nawei Sun for contributions to preliminary studies and discussions. We thank members of the Kampmann lab for discussions and feedback on the manuscript. This research was supported by NIH grants F30 AG066418 to K.L., T32 NS115706 to I.V.L.R., R01 AG057342 and P30 AG062422 to A.W.K., and R01 AG062359 to M.K., a Chan Zuckerberg Initiative Award to A.W.K., and a Chan Zuckerberg Initiative Ben Barres Early Career Acceleration Award to M.K.

AUTHOR CONTRIBUTIONS

B.R., K.L., and M.K. conceptualized and led the overall project, and wrote the manuscript with input from all co-authors. B.R. performed the majority of experiments and data analysis. K.L. developed the iAstrocyte platform, performed preliminary studies, and conducted the RNA-seq experiments. In consultation with J.E., F.M. aided with sample preparation for whole-cell and lysosome-specific proteomics experiments, and performed mass spectrometry and preliminary computational analysis. I.V.L.R. performed sample prep for the cell-surface LAMP1 CRISPRi screens. K.A.H. guided TIRF experiments. M.L. and S.B. aided with design and sample preparation for whole-cell and lysosome-specific proteomics experiments, respectively. M.Y.C. and A.W.K. provided FIRE-pHLy reagents and guidance on lysosome pH experiments. S.F. conducted LAMP2 immunofluorescence experiments and data analysis.

COMPETING INTERESTS STATEMENT

A.W.K is a member of the Scientific Advisory Board for Nine Square Therapeutics, Inc. J.E. is an advisor to Seer, Inc. M. K. has filed a patent application related to CRISPRi and CRISPRa screening (PCT/US15/40449) and serves on the Scientific Advisory Board of Engine Biosciences, Casma Therapeutics, and Cajal Neuroscience, and is an advisor to Modulo Bio and Recursion Therapeutics. None of the other authors declare competing interests.

DATA AVAILABILITY STATEMENT

Bulk RNA-seq data of hiPSC-derived astrocytes analyzed in this study were generated previously¹⁰⁷ and are available on the Gene Expression Omnibus (GEO) under accession code GSE182307. Mass spectrometry results are in the process of submission to PRIDE.

CODE AVAILABILITY STATEMENT

The code used to analyze the data presented in this study will be shared upon request.

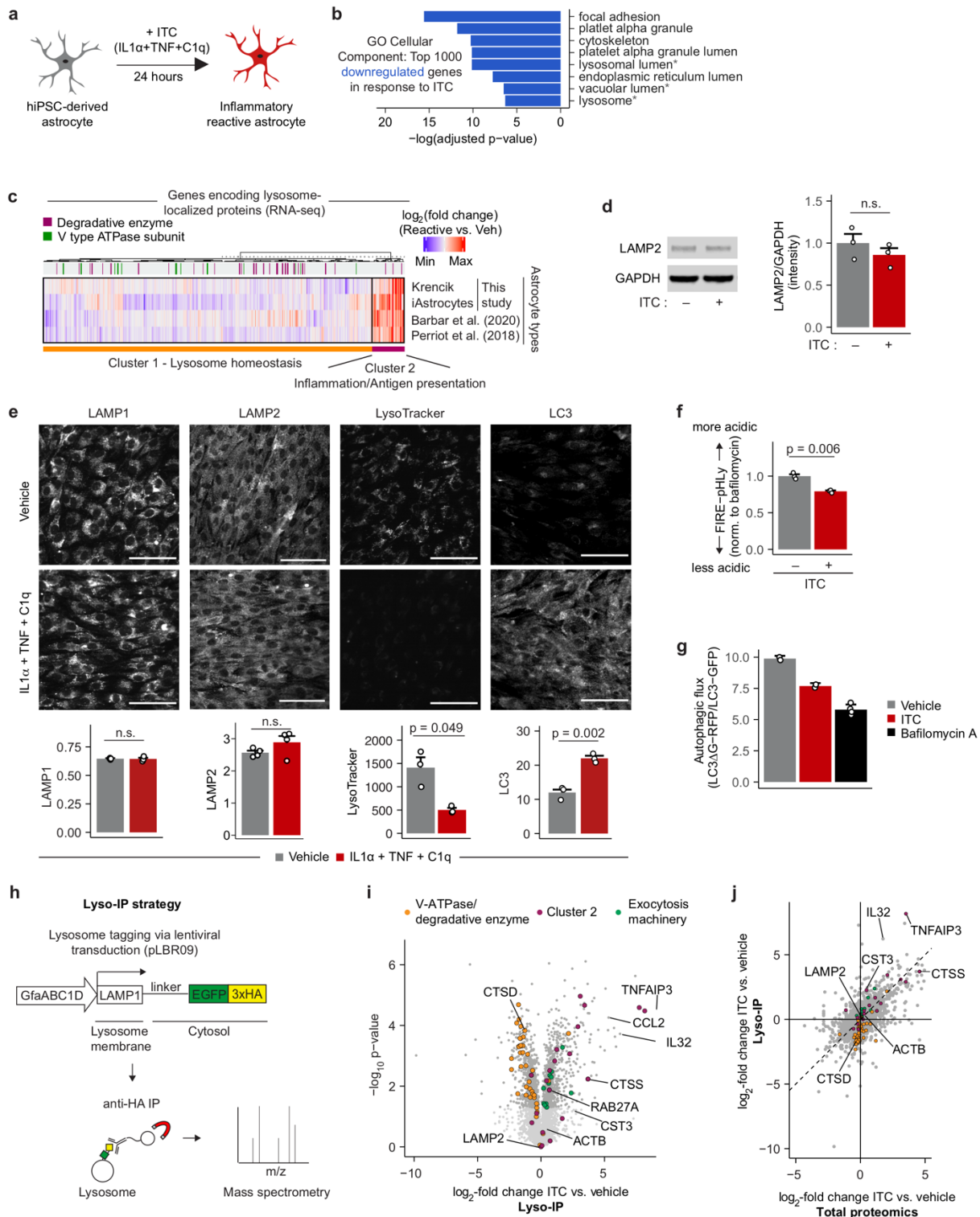


Fig. 4.1 | Lysosomes are remodelled in inflammatory reactive astrocytes. **a**, Schematic of the *in vitro* model of inflammatory astrocyte reactivity used in this study. **b**, Bar graph of Gene Ontology (GO) terms enriched among the top 1000 genes with decreased expression in iAstrocytes treated with IL1 α +TNF+C1q (ITC) compared to vehicle control from RNA-Seq (n = 3 per condition). **c**, Heatmap of the mean log₂(fold change) of gene transcripts with GO

annotations of lysosome, lysosomal membrane, or lysosomal lumen in response to inflammatory stimuli for astrocytes derived using protocols described in Leng *et al.*¹⁰⁷ (iAstrocytes), Krencik *et al.*¹⁵ and published datasets from Barbar *et al.*¹⁰⁶ and Perriot *et al.*¹⁰⁹ (see Methods). **d**, *left*, representative immunoblot of total LAMP2 protein in iAstrocytes treated with ITC or a vehicle control; *right*, quantification of blots from $n = 3$ independent wells. **e**, Representative images of vehicle- (*top*) and ITC-treated (*middle*) iAstrocytes stained for the indicated lysosome/autophagosome markers, with corresponding quantification (*bottom*, see Methods; $n = 3$ independent wells per condition; scale bar = 75 μm). **f**, Lysosome acidity of FIRE-pHLy-expressing iAstrocytes (measured by flow cytometry) treated with ITC relative to vehicle-treated controls ($n = 3$ (for LAMP2, $n = 4$) independent wells for each condition). **g**, Autophagic flux (measured with GFP-LC3-RFP-LC3 Δ G reporter-expressing iAstrocytes) treated with vehicle, ITC, or 100 nM bafilomycin A ($n = 3$ independent wells for each condition). **h**, Workflow of lysosome proteomics (lyso-IP, see Methods). **i**, Volcano plot of the \log_2 (fold change) and associated log-scaled p-values of protein abundances detected by lyso-IP from astrocytes treated with ITC relative to vehicle-treated controls (see Methods; $n = 3$ per condition). **j**, Scatter plot of the \log_2 (fold change) of proteins detected by lyso-IP versus whole-cell proteomics from astrocytes treated with ITC relative to vehicle-treated controls (see Methods; $n = 3$ per condition). For bar graphs, individual data points represent individual wells, while error bars represent the standard error of the mean (s.e.m.). The two-sided Student's t-test was used in panels **d-f**.

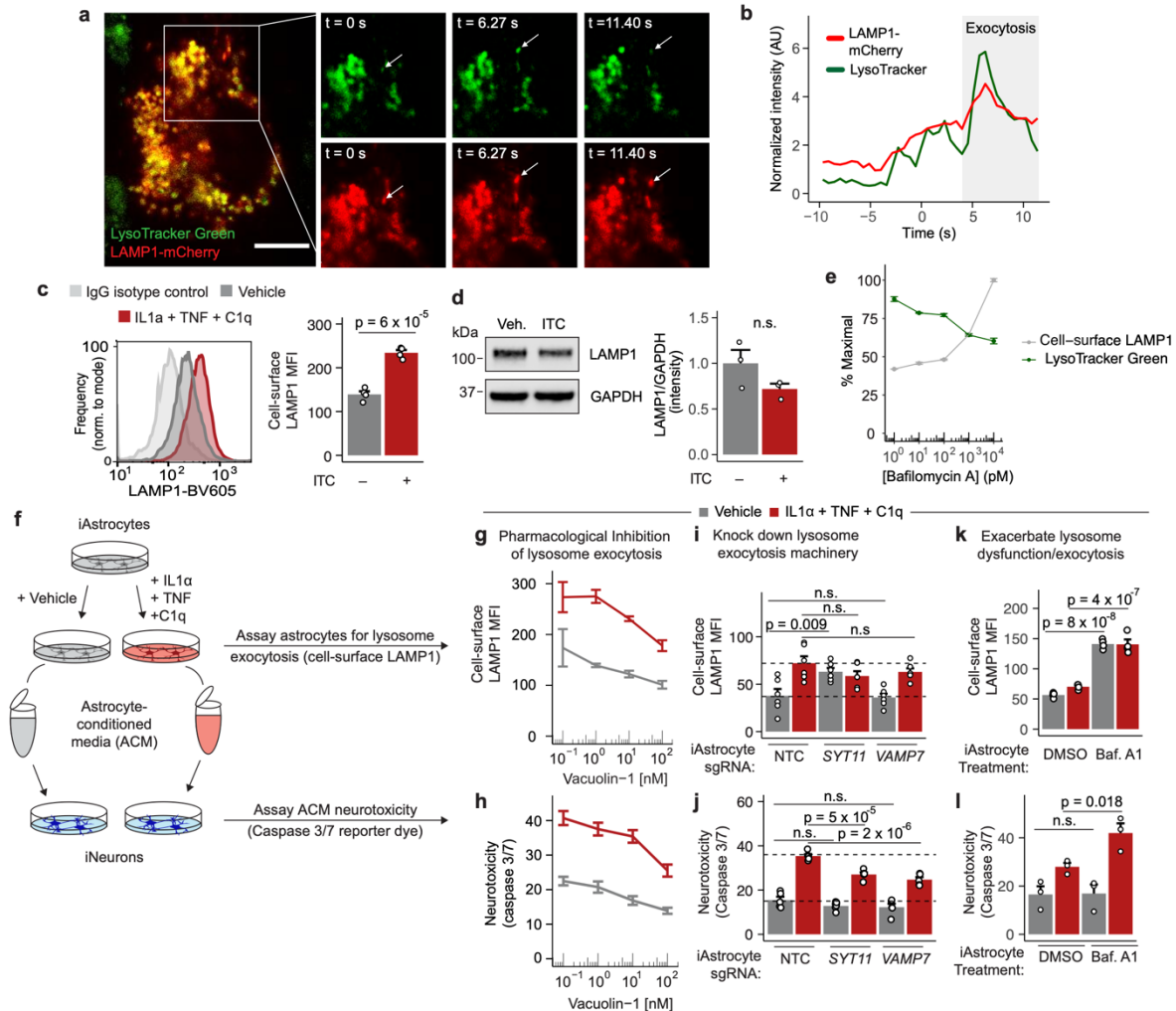


Fig. 4.2 | Lysosome exocytosis controls neurotoxicity of inflammatory reactive astrocytes. **a**, Representative TIRF microscopy images of a lysosome exocytosis event (arrows) in iAstrocytes. **b**, Quantification of LAMP1-mCherry (lysosomal membrane) and LysoTracker (lysosomal lumen) fluorescence intensity over the course of the lysosome exocytosis event depicted in **a**. **c**, Cell-surface LAMP1 for iAstrocytes treated with ITC or a vehicle control measured by flow cytometry. *Left*, representative flow cytometry results, including isotype control staining; *right*, Quantification of replicates, with the average median fluorescence intensity (MFI) value of IgG isotype controls ($n = 2$ for each condition) subtracted from the LAMP1 MFI values ($n = 4$ for each condition). **d**, Total LAMP1 protein in ITC and vehicle-treated iAstrocytes. *Left*, Representative immunoblot; *right*, quantification of independent wells ($n = 3$ for each condition). **e**, Bafilomycin A dose-response curves of LysoTracker and cell-surface LAMP1 measured by flow cytometry in iAstrocytes ($n = 3$ wells per condition). Values are quantified as the percent of the maximal value obtained in each individual experiment (LysoTracker or cell-surface LAMP1). **f**, Experimental strategy for parallel measurement of lysosome exocytosis and neurotoxicity of astrocyte conditioned media (ACM) (see Methods). **g**–**l**, Quantification of lysosome exocytosis in iAstrocytes (**g**, **i**, and **k**) and neurotoxicity of astrocyte (measured by caspase 3/7 activity reporter dye intensity) in iNeurons (**h**, **j**, and **l**) after treating iAstrocytes with the lysosome exocytosis inhibitor vacuolin-1 (**g**, **h**), knocking down

lysosome exocytosis machinery in iAstrocytes with sgRNAs targeting *SYT11* and *VAMP7* (**i,j**), or treating iAstrocytes the lysosome exocytosis-inducing compound bafilomycin A (**k,l**). For bar graphs, data points represent individual wells with error bars representing the s.e.m. The two-sided Student's t-test was used in panels **c-d** and linear regression was used in panels **i-l** to compute p-values; for linear regression, p-values were corrected for multiple testing using Holm's method.

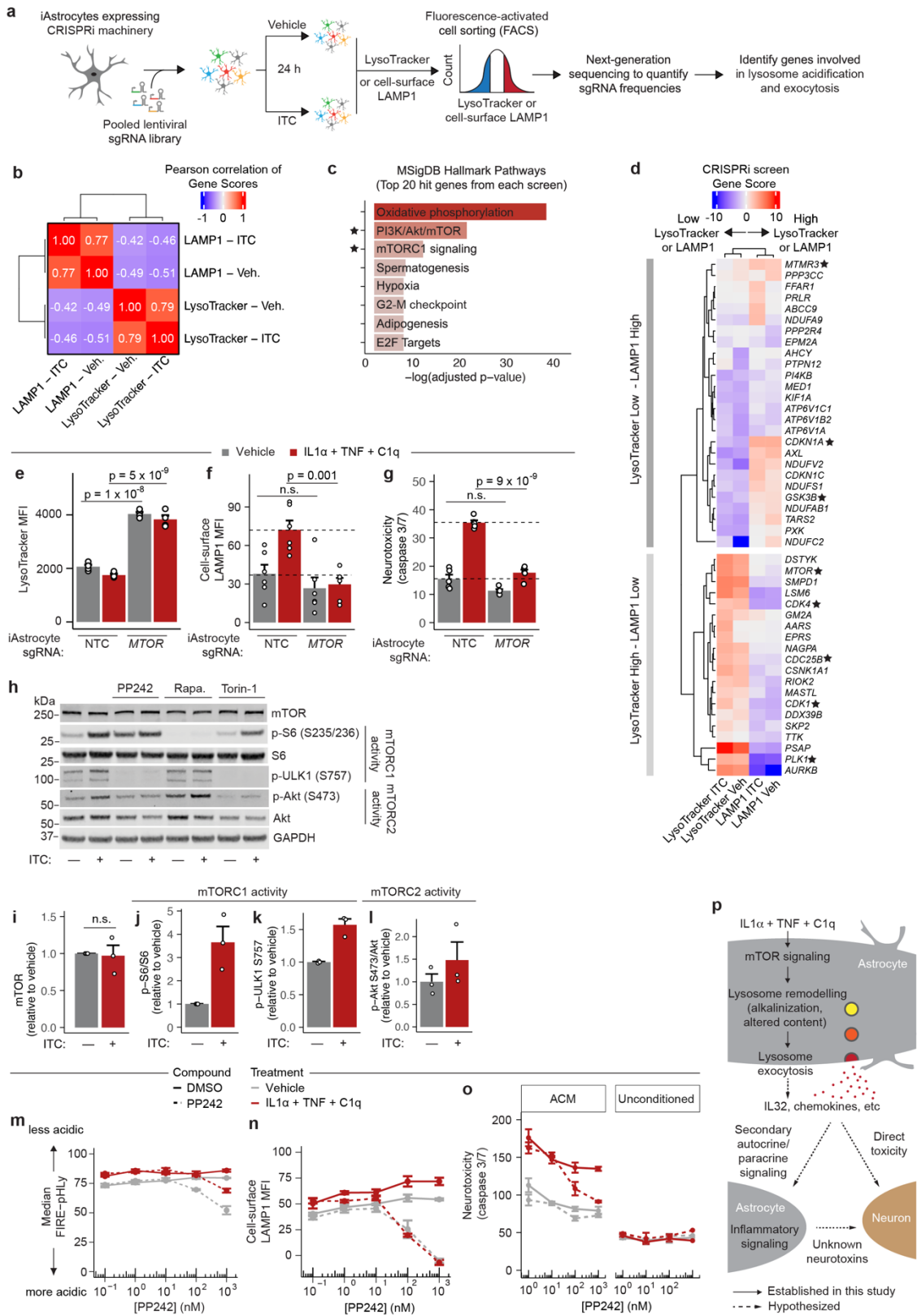


Fig. 4.3 (Legend overleaf)

Fig. 4.3 | CRISPRi screens uncover mTOR as a regulator of lysosome exocytosis and inflammatory reactive astrocyte-mediated neurotoxicity. **a**, Workflow of FACS-based CRISPRi screens in iAstrocytes (see Methods). **b**, Pearson correlations of the gene scores (see Methods) of hit genes from the 4 CRISPRi screens completed ($n = 2$ per condition). **c**, Bar graph of Molecular Signature Database (MSigDB) terms whose constituent genes are most significantly enriched among the 20 strongest hit genes of any CRISPRi screen (46 genes total, see Methods). **d**, Heatmap of gene scores across all CRISPRi screens for genes from **c**, with mTOR-related hits starred. **e-g**, iAstrocytes were transduced with non-targeting control (NTC) or *MTOR* sgRNA and treated with IL1a + TNF + C1q (ITC) or vehicle as indicated ($n = 3$ independent wells per condition), and (e) LysoTracker staining (f) cell-surface LAMP1, and (g) neurotoxicity of astrocyte-conditioned media were quantified. **h**, Representative immunoblots of mTOR levels and activity in iAstrocytes treated with a panel of mTOR inhibitors in combination with ITC or vehicle control. **i-l**, Quantification of immunoblots (from $n = 3$ independent wells for each condition). **m-o**, Dose-response curves of (m) lysosome acidification (measured by flow cytometry of FIRE-pHLY-expressing iAstrocytes, (n) lysosome exocytosis (flow cytometry measurement of cell-surface LAMP1, and (o) astrocyte-mediated neurotoxicity (measured by caspase 3/7 activity reporter dye intensity) upon treatment of iAstrocytes with the pan-mTORC inhibitor PP242 in conjunction with vehicle vs. ITC ($n = 3$ independent wells for each condition). **p**, Model for a potential role of mTOR-dependent lysosomal remodelling and exocytosis in astrocyte-mediated neurotoxicity. For bar graphs, data points represent individual wells with error bars representing the s.e.m. Linear regression was used to compute p-values in all panels; p-values were corrected for multiple testing using Holm's method.

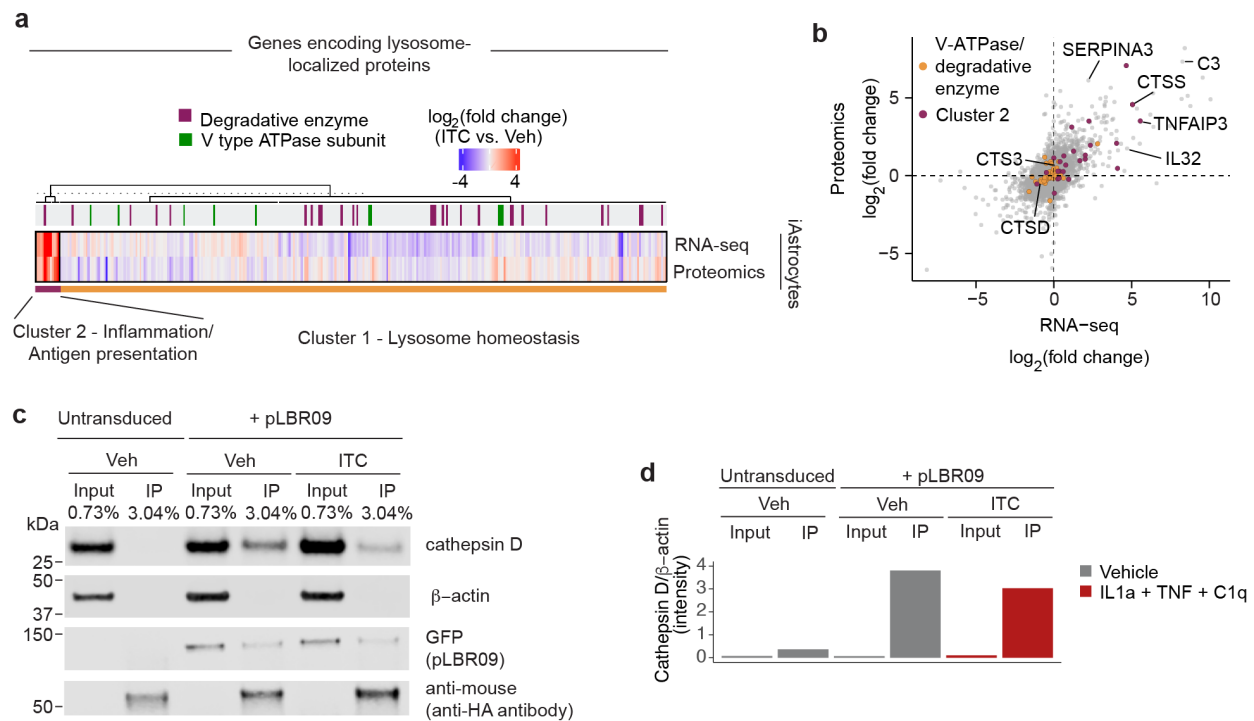


Fig. S4.1 | Further characterization of lysosome remodeling in inflammatory reactive astrocytes. **a**, Heatmap of the mean $\log_2(\text{fold change})$ (ITC-treated astrocytes relative to vehicle-treated astrocytes) of genes or proteins with GO annotations of lysosome, lysosomal membrane, or lysosomal lumen from RNA-seq or whole-cell proteomics. **c**, Representative immunoblot of vehicle and ITC-treated samples obtained for lysosome immunoprecipitation (lyso-IP) experiment (+pLBR09, IP) with untransduced and non-immunoprecipitated (+pLBR09, Input) negative controls. **d**, Quantification of the cathepsin D (lysosomal lumen to β -actin (cytosol) ratio from immunoblots shown in **c**.

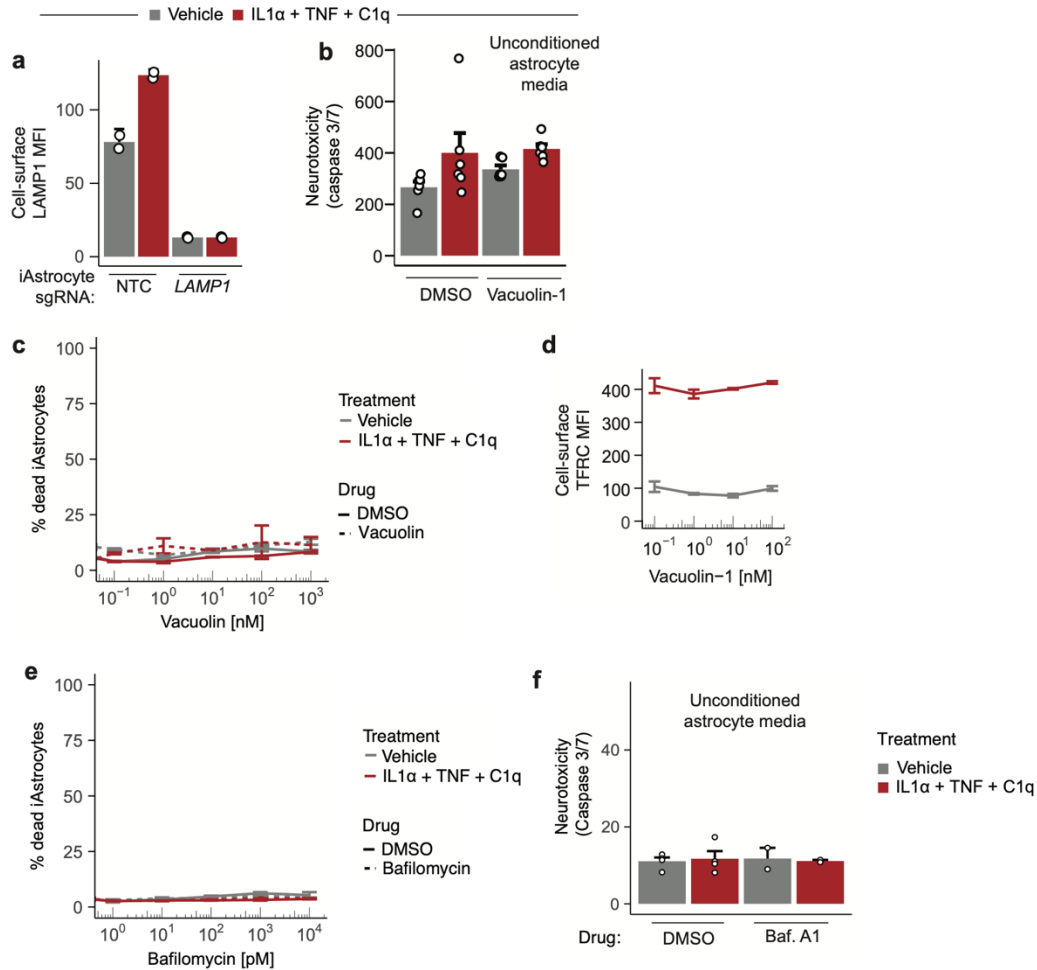


Fig. S4.2 | Further characterization of the lysosome alkalization-exocytosis-neurotoxicity axis in iAstrocytes. **a**, Cell-surface LAMP1 levels (median fluorescence intensity – MFI; measured by flow cytometry) in vehicle and ITC-treated iAstrocytes transduced with NTC or *LAMP1* sgRNA. **b**, Apoptosis of iNeurons treated with unconditioned astrocyte media containing the maximum concentration of vacuolin used in this study (100 nM). **c**, Percentage of dead iAstrocytes (measured by flow cytometry as DAPI+ cells) in response to concentrations of vacuolin used in this study. **d**, Cell-surface TFRC levels (MFI; measured by flow cytometry) of the iAstrocytes shown in Fig. 4.2g,h. **e**, Percentage of dead iAstrocytes (measured by flow cytometry as DAPI+ cells) in response to concentrations of bafilomycin A used in this study. **f**, Apoptosis of iNeurons treated with unconditioned astrocyte media containing the maximum concentration of bafilomycin A used in conditioned media experiments (10 nM).

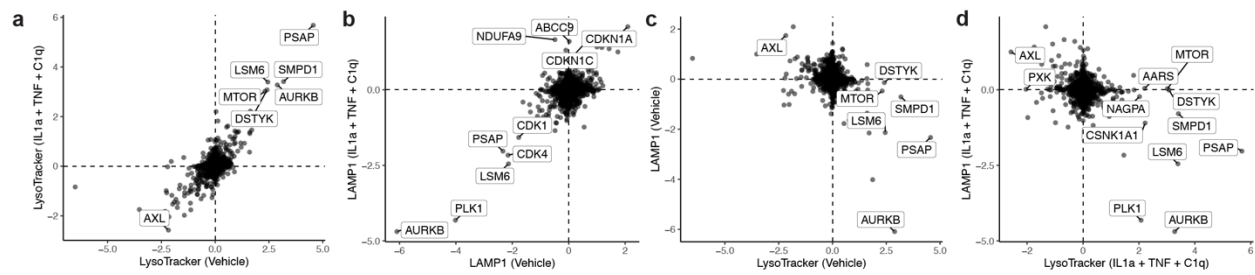


Fig. S4.3 | LysoTracker and LAMP1 CRISPRi screening results. Scatterplots comparing gene scores (see Methods) between screens for (a) LysoTracker, (b) LAMP1, (c) vehicle-treated screens, and (d) ITC-treated screens.

METHODS

hiPSC culture

Human iPSCs (male WTC11 background⁸²) were cultured in Essential 8 (E8) Medium (ThermoFisher Scientific cat. no. A1517001) on BioLite Cell Culture Treated Dishes (ThermoFisher Scientific) coated with Growth Factor Reduced, Phenol Red-Free, LDEV-Free Matrigel Basement Membrane Matrix (Corning cat. no. 356231) diluted 1:100 in DMEM/F12 (ThermoFisher Scientific cat. no. 11330032). Essential 8 Medium was replaced daily. When hiPSC colonies demonstrated mature morphology, the hiPSCs were either clump passaged with EDTA for routine maintenance or dissociated to a near single-cell suspension with Accutase Cell Dissociation Reagent (ThermoFisher Scientific cat. no. A11105-01) for applications requiring cell counting. For clump passaging with EDTA, hiPSCs were washed with Dulbecco's phosphate buffered saline (DPBS; Milipore Sigma cat. no. D8537) and then incubated with Versene (ThermoFisher Scientific cat. no. 15040066) for 5-7 min at room temperature; the Versene solution was then aspirated and replaced with E8 + 10 nM Y-27632 dihydrochloride ROCK inhibitor (Tocris cat. no. 125410); hiPSC colonies were then gently detached mechanically using a cell scraper, resuspended gently, and passaged at 1:10-1:30 dilution in E8 + Y-27632, with Y-27632 removed the next day. For near single-cell dissociation, hiPSCs were washed with DPBS, incubated with Accutase for 5-10 min at 37 °C, and then gently triturated with a P1000 pipette tip; the cell suspension was then diluted with PBS, collected into conical tubes, and spun down at 300 g for 3 min; hiPSCs were then resuspended in E8 + Y-27632, counted, and plated onto Matrigel-coated plates at the desired density in E8 + Y-27632; Y-27632 would be maintained until the hiPSC colonies reached the appropriate size (> ~40 cells). Studies with hiPSCs at UCSF were approved by the The Human Gamete, Embryo and Stem Cell Research (GESCR) Committee. Informed consent was obtained from the human subject when the WTC11 line was originally derived⁸².

Generation of iAstrocytes

iAstrocytes were generated as detailed in Leng *et al.*¹⁰⁷. Briefly, we generated hiPSCs (male WTC11 background) used for iAstrocyte differentiation by inserting a CRISPRi machinery cassette (pC13N-dCas9-BFP-KRAB, Addgene plasmid no. 127968) into the CLYBL safe-harbor locus and a doxycycline-inducible *NFIA* and *SOX9* cDNA cassette into the AAVS1 safe-harbor locus using TALEN-based editing. After recovering a monoclonal CRISPRi-*NFIA*-*SOX9* line, we differentiated hiPSCs to the neuroectoderm lineage via an embryoid body (EB)-based neural induction protocol. After dissociating plating EB-derived cells, we selected and expanded those forming neural rosettes. We used fluorescence activated cell sorting (FACS) to enrich for pure CD133+/CD271- neural progenitor cell (NPC) populations for expansion.

For iAstrocyte differentiation, these NPCs were re-plated on 1:200 Matrigel-coated dishes and cultured with ScienCell Astrocyte Media (ScienCell Research Laboratories cat. no. 1801) + 2 μ g/mL doxycycline (Millipore Sigma cat. no. D9891) to initiate iAstrocyte differentiation. A full media change was completed every other day (maintaining doxycycline at 2 μ g/mL) until NPCs reached confluency, at which time they were dissociated with Accutase and split 1:10 onto new Matrigel coated dishes (or cryopreserved) for continued differentiation and expansion. Expansion was continued until day 20 (d20) of differentiation, yielding iAstrocytes. See Leng *et al.*¹⁰⁷ for full details of iAstrocyte hiPSC generation and differentiation protocols.

Induction of inflammatory reactivity in iAstrocytes

For all iAstrocyte experiments in this study, d20 iAstrocytes were plated at 20,000 cells/cm² on 1:200 Matrigel-coated BioLite Cell Culture Treated Dishes (ThermoFisher Scientific) in ScienCell Astrocyte Media (without doxycycline) on d0. Full media changes were completed on d1, d3, and d5. On d5, media was supplemented with IL-1 α (3 ng/mL; Peprotech cat. no. AF-

200-01A), TNF (30 ng/mL; Peprotech cat. no. AF-300-01A), and C1q (400 ng/mL; Complement Technology cat. no. A099) to induce inflammatory reactivity according to Liddelow *et al.*⁸. All experiments were conducted 24 hours after cytokine treatment (d6).

CRISPRi-mediated gene knockdown using lentiviral transduction of individual sgRNAs

To knock down genes with individual sgRNAs, we cloned CRISPRi sgRNAs into pMK1334⁸³ (Addgene cat. no. 127965), as previously described⁸⁶. We generated lentivirus of the resulting constructs by co-transfecting them with 3rd generation lentiviral packaging plasmids with TransIT-Lenti Transfection Reagent (Mirus cat. no. MIR6606) according to the manufacturer's protocol. The next day, lentivirus was precipitated using Lentivirus Precipitation Solution (ALSTEM cat. no. VC150) according to the manufacturer's protocol, resuspended in DPBS, and aliquoted and stored at -80 °C. iAstrocytes were transduced with lentivirus at the time of plating. When necessary, the functional titer of the lentivirus was determined by measuring BFP+ cells 48 hours after transducing iAstrocytes with a serial dilution of lentivirus. The protospacer sequences of the sgRNAs used in this study were designed based on our next-generation CRISPRi algorithm³⁹ and are listed below:

NTC – GAGACGAGGACATGTGTAGC

MTOR – GGGACAGCGGGGAAGGCGGG

SYT11 – GGAAGGGGGAAGGTATCCAG

VAMP7 – GAGGGACGCGGGTCAGTGCA

Generation and lentiviral transduction of reporter constructs

To subclone the original FIRE-pHLy construct (pLBR10, Ubc:FIRE-pHLy)¹¹⁰ to make pLBR11 (GfaABC1D:FIRE-pHLy), we excised the FIRE-pHLy cassette from pLBR10 and linearized the backbone vector (pKL20; pHIV gfaABC1D:mRuby:WPRE) with BamH1-HF (New

England BioLabs, cat. no. R3136) and ClaI (New England BioLabs cat. no. R0197). We then ran these reactions on a 1% agarose gel, gel extracted the relevant fragments, and ligated them together with T4 DNA Ligase (New England BioLabs cat. no. M0202) per manufacturer's protocol to generate pLBR11.

Both pLBR11 (all FIRE-pHLy experiments), and GFP-LC3-RFP-LC3 Δ G (reporter cassette from Addgene plasmid #84572)¹¹¹ reporters were transduced into iAstrocytes with lentivirus at low multiplicity of infection (MOI) during plating to prevent high expression of exogenous lysosomal proteins.

Immunofluorescence imaging

For immunofluorescence imaging experiments, iAstrocytes plated in Greiner μ Clear 96-well plates (Greiner Bio-One cat. no. 655087) were fixed with 4% paraformaldehyde (diluted from a 16% solution; Electron Microscopy Sciences cat. no. 15710) for 15 min at RT. After washing three times with DPBS, we blocked and permeabilized cells with DPBS (Millipore Sigma cat. no. D8537) + 3% BSA (Millipore Sigma cat. no. A9647) + 0.1% Triton X-100 (Millipore Sigma cat. no. X100) for 30 min at RT. Primary antibodies against LC3 (1:50; rabbit polyclonal; Cell Signaling Technology cat. no. 2775), LAMP1 (1:50; mouse monoclonal; Abcam cat. no. ab25630), or LAMP2 (1:500, Abcam cat. no. ab25631) were added to blocking buffer and incubated with iAstrocytes overnight at 4 °C. Afterwards, the samples were washed with DPBS three times, incubated with pre-adsorbed secondary antibodies (1:500 goat anti-mouse IgG Alexa Fluor 488, 1:500 goat anti-rabbit IgG Alexa Fluor 555; Abcam cat. no. ab150119 and ab150086) for 1 hour at RT, washed three times with DPBS, incubated with 1 μ g/mL Hoechst 33342 (ThermoFisher Scientific cat. no. H3570) and then washed two additional times before imaging on an IN Cell Analyzer 6000, using a 60X 0.7 NA objective, 2x2 binning, 100-400 ms exposure, an aperture width of \sim 1 Airy unit, and 9-16 fields per well.

LysoTracker staining and imaging

iAstrocytes were washed with DPBS and incubated with a 50 nM solution of LysoTracker Green DND-26 (ThermoFisher Scientific cat. no. L7526) in DPBS for 5 minutes at 37°C, washed two times with DPBS, and processed for downstream experiments. For imaging (Fig. 4.1e), iAstrocytes were imaged at 37°C and 5% CO₂ using an IN Cell Analyzer 6000 as above. For flow cytometry (CRISPRi screens), iAstrocytes were dissociated with Accutase for 10 mins at 37°C after LysoTracker staining, and resuspended in FACS buffer (DPBS + 1% BSA + 2 mM EDTA (Milipore Sigma cat. no. 324506)).

TIRF imaging

iAstrocytes were plated at 20,000 cells/cm² in 35 mm imaging dishes (Ibidi, cat. no. 81156) and simultaneously transduced with pLBR11 (GfaABC1D:FIRE-pHLy). Prior to imaging, the conditioned media of iAstrocytes was collected. iAstrocytes were then stained with LysoTracker as detailed above and re-incubated with the collected conditioned media for the duration of imaging. TIRF was performed on a Nikon Ti-E inverted microscope equipped with a Nikon TIRF illuminator, Nikon motorized stage with piezo Z inset, Andor iXon Ultra DU897 camera, and run by NIS-Elements (v5.20.00 build 1423). iAstrocytes were imaged using an Apo TIRF 100x/1.49 oil (DIC N2/ 100X I) objective, 488nm and 561nm lasers (Agilent MLC400 monolithic laser combiner) and Sutter Lambda 10-B with ET525/50m and ET600/60m emission filters (Chroma), respectively, for 120 seconds with 100 ms exposure (per channel).

Measurement of apoptosis in iNeurons treated with astrocyte-conditioned media

hiPSC-derived neurons (iNeurons) were generated from WTC11 hiPSCs with a stably integrated dox-inducible NGN2 cassette (i3N iPSCs) as previously described¹¹⁶. Conditioned media was collected from iAstrocytes and spun down at 300 x g for 5 min to remove dead cells,

supplemented with CellEvent Caspase 3/7 Detection Reagent (ThermoFisher Scientific, cat. no. C10423) to a final concentration of 2 μ M, and transferred to day 17 iNeurons after removing the original iNeuron media. As an unconditioned media control, we incubated ScienCell Astrocyte Media in identical conditions (37 °C, 5% CO₂, cytokine and/or small-molecule compounds) as their respective experimental groups but without iAstrocytes. After a ~24 hour incubation period, iNeuron viability was assessed by imaging on an IN Cell Analyzer 6000, using a 20X 0.45 NA objective, 2x2 binning, environmental control set to 37 °C and 5% CO₂, an aperture width of ~1 Airy unit, 200 ms exposure, and 4-9 fields per well. The level of apoptosis in iNeurons was quantified relative to an unstained negative control with CellProfiler (see Data Analysis section).

Antibody staining for flow cytometry

To measure cell-surface protein levels (i.e. LAMP1, TFRC), iAstrocytes were dissociated with Accutase for 10 mins at 37 °C, diluted with ice-cold DPBS + 1% BSA, and spun down at 300 x g for 5 minutes at 4 °C. After aspirating the supernatant, all cells were incubated in 1:20 Fc block (BD Bioscience cat. no. 564220) diluted in DPBS + 3% BSA for 10 minutes on ice, followed by the addition of 1:20 (1:40 final) primary antibodies against LAMP1 (AF488- or BV605-conjugated; BioLegend cat. no. 328610 and 328634), and/or TFRC (FITC-conjugated, Biolegend, cat. no. 334104) for an additional 30 minute incubation on ice in the dark. iAstrocytes were then washed with ice-cold DPBS + 1% BSA, spun down at 300 x g for 5 mins at 4 °C, and resuspended in DPBS + 1% BSA for flow cytometry.

Pooled CRISPRi screening

CRISPRi screens were conducted as described in Leng *et al.*¹⁰⁷. Both LysoTracker and LAMP1 screens were conducted with the H1 (i.e. “druggable genome”) sgRNA sub-library from our next-generation CRISPRi library³⁹. We generated lentivirus for the pooled H1 sgRNA library as previously described⁸³. For each screen (i.e. LysoTracker or cell-surface LAMP1, vehicle or

ITC), iAstrocytes were plated at 20,000 cells/cm² onto 4 Matrigel-coated 15-cm dishes, transduced with the H1 lentiviral sgRNA library with >70% transduction efficiency, treated with vehicle control or IL-1 α +TNF+C1q for 24 hours, stained for LysoTracker or cell-surface LAMP1, and then sorted into LysoTracker high vs. low or cell-surface LAMP1 high vs. low (top and bottom 35% of cells on fluorescence histogram) populations. iAstrocytes were sorted with a BD FACSAria Fusion cell sorter at 5,000-10,000 events per second, and then pelleted via centrifugation at 300 x g for 10 minutes for genomic DNA extraction. sgRNA abundances were then measured using next-generation sequencing as previously described⁸³. LysoTracker screens were performed with two experimental replicates per condition, while LAMP1 screens were done with one replicate. Results from all CRISPRi screens in this study can be interactively explored at www.crisprbrain.org.

Western blots

iAstrocytes were dissociated with Accutase for 10 mins at 37°C, spun down at 300 x g for 5 mins, washed with ice-cold DPBS, lysed in RIPA buffer (Thermo Fisher Scientific, cat. no. 89900) with protease (Roche, cat. no. 04693159001) and phosphatase inhibitors (Sigma-Aldrich, cat. no. PHOSS-RO), and incubated on ice for 45 minutes with brief vortexing every 15 minutes. Samples were centrifuged at 18,000 x g for 20 mins at 4°C to pellet insoluble components of lysate. After the total protein was quantified using the Pierce BCA Protein Assay Kit (ThermoFisher Scientific, cat. no. 23225) in the supernatant, each sample was diluted to the same concentration, and denatured with NuPAGE LDS Sample Buffer (4X) (ThermoFisher Scientific, cat. no. NP0007) and reduced with DTT.

Equivalent protein amounts (20-40 ug) were run on 10% NuPAGE Bis-Tris gels (ThermoFisher Scientific, cat. no. NP0301) and transferred to nitrocellulose membranes (Bio-Rad, 1704271). We performed ponceau staining (Milipore Sigma, cat. no. P7170) to validate equivalent loading between lanes. Membranes were blocked with TBST (TBS + 0.1% Tween-

20) + 5% BSA for 1 hour at RT on a shaker, after which they were incubated with primary antibodies against phospho-S6 (1:500; polyclonal rabbit; Cell Signaling Technology cat. no. 2211), S6 (1:1000; monoclonal rabbit; Cell Signaling Technology cat. no. 2217), phospho-ULK1 (1:500; polyclonal rabbit; Cell Signaling Technology cat. no. 14202), phospho-Akt (1:500; monoclonal rabbit; Cell Signaling Technology cat. no. 4060), pan-Akt (1:1000; monoclonal mouse; Cell Signaling Technology cat. 2920), LAMP1 (1:1000; mouse monoclonal; Abcam cat. no. ab25630), LAMP2 (1:1000; mouse monoclonal; Abcam cat. no. ab25631), CTSD (1 ug/mL, R&D Systems cat. no. AF1014), β -actin (1:1000, rabbit monoclonal; Cell Signaling Technology cat. no. 4970), or EGFP (1:200; mouse monoclonal; Santa Cruz Biotechnology cat. no. sc-9996) at 4°C overnight on a shaker. Blots were washed with TBS and incubated with secondary antibodies goat anti-mouse IRDye 800CW (1:10,000; LI-COR cat. no. 926-32210) and goat anti-rabbit IRDye 680RD (1:10,000; LI-COR cat. no. 926-68071) in blocking buffer (see above) for 1 hour at RT on a shaker. Afterwards, blots were washed with TBS, and imaged using an Odyssey Fc Imaging system (LI-COR, cat. no. 2800). To re-probe blots, we incubated membranes with 1X NewBlot Nitro Stripping Buffer (LI-COR, cat. no. 928-40030) for 5 minutes at RT on a shaker before re-blocking and probing as above. Immunoblot bands were quantified with LI-COR ImageStudio software.

Source data for immunoblots is provided in Supplementary Figures 2-5.

Whole-cell proteomics sample preparation

iAstrocytes were washed and collected (detached gently using a cell scraper) in ice-cold DPBS, spun down at 300 x g for 5 mins at 4 °C, and stored at -80 °C. Cell pellets were lysed in 2.5% sodium dodecyl sulfate (SDS) 50mM Tris pH 8 and heated to 95 °C for 5min, then subjected to probe sonication. Lysates were centrifuged at 14000g for 15 min before protein quantification using BCA assay (Pierce, Thermo Fisher Scientific) according to manufacturer's

instructions. Protein lysates were acetone precipitated by adding 5 volumes of ice-cold acetone, vortexed, incubated at -20 °C for 1 hr and pelleted by centrifugation at 21000g and 4 °C for 15 min. Protein pellets were resuspended in 1% sodium deoxycholate (SDC) 50 mM EPPS pH 8.5 and reduced by incubating at 37 °C for 20 min with rotation in the presence of 5mM DTT. Protein was then alkylated by incubating in the dark at 37 °C for 20 min in the presence of 25mM iodoacetamide before digestion overnight with LysC at an enzyme-to-protein ratio of 1:50 followed by 3 hr digestion with trypsin at an enzyme-to-protein ratio of 1:50. Digestion was stopped by acidification to 1% trifluoroacetic acid (TFA) and placed on ice for 10min to promote precipitation of SDC. The SDC was then pelleted and removed by centrifugation at 21000g for 10min. The supernatant containing acidified peptides were then de-salted on in-house made Stagetips¹²⁴ packed with polystyrene divinyl benzene reverse phase sulphonate solid phase extraction material (CDS Empore, Fisher Scientific) as previously published¹²⁴. Stagetips were prepared by activating with 100% methanol, conditioning with 80% acetonitrile containing 0.1% TFA, equilibrated with 0.2% TFA, followed by sample loading, washing twice with 99% isopropanol containing 0.1% TFA, washing twice with 0.2% TFA and once with 0.1% FA. Peptides were eluted with 60% acetonitrile (ACN) containing 0.5% ammonium hydroxide. The desalted peptides were then flash frozen and dried by centrifugal evaporation.

Lysosome-specific proteomics sample preparation

pLBR09 (gfaABC1D: LAMP1-XTEN80-mEGFP-3XHA) used for lysosome immunoprecipitation was generated by subcloning pLBR08 (EF1 α : LAMP1-XTEN80-mEGFP-3XHA). Briefly, pLBR08 was generated via Gibson assembly of PCR-amplified LAMP1 cDNA (from mTagRFP-T-Lysosomes-20 acquired from Nikon Imaging Center at UCSF, Addgene plasmid #58022) and PCR-amplified XTEN80-mEGFP-3xHA immunoprecipitation tag with a linearized backbone generated from ClaI and BspDI (New England BioLabs cat. no. R0557) digestion of pKL017 (pHIV EF1a:Clover:WPRE). pLBR09 was then generated by linearizing

pKL020 (pHIV gfaABC1D:mRuby:WPRE) and excising the LAMP1-XTEN80-mEGFP-3XHA cassette of pLBR08 via restriction digest with XbaI (New England Biolabs cat. no. R0145) and ClaI. The resulting fragments were run on a 1% agarose gel and gel extracted (Zymoclean Gel DNA Recovery Kit, cat. no. D4007). These fragments were ligated together with T4 DNA Ligase per manufacturer protocol. iAstrocytes were plated at 20,000 cells/cm² per experimental replicate and transduced with pLBR09 lentivirus during plating. We used three replicates each for vehicle and ITC conditions.

Lysosome immunoprecipitation was performed as previously described¹¹². Briefly, iAstrocytes were washed and collected (detached gently using a cell scraper) in ice-cold DPBS, spun down at 300 x g for 5 mins at 4 °C. We then resuspended the cell pellet in homogenization buffer (25 mM Tris HCl pH 7.5, 50 mM sucrose, 0.5 mM MgCl₂, 0.2 mM EGTA with protease inhibitors). The iAstrocyte cell suspension was mechanically lysed with a 23G syringe, immediately transferred to isotonic buffer (2.5M sucrose, 0.2 mM EGTA, 0.5 mM MgCl₂) and spun at 3000 x g for 10 mins at 4 °C. The supernatant was transferred to anti-HA magnetic beads (Thermo Scientific cat. no. PI88836) for the pulldown of intact lysosomes, with the final resuspension in 1X urea buffer (2M Urea, 1 mM DTT, 12.5 mM Tris). On-bead digest was performed by sequentially incubating the resulting protein samples with 5 mM (final concentration) IAA at 22°C and 225 rpm for 30 mins, 0.5 ug LysC at 22°C and 225 rpm overnight, 1 ug of trypsin at 22°C and 225 rpm for 4 hours, and 1% (final concentration) TFA. Acidified peptides were then de-salted according to the same protocol as whole-cell proteome samples. For western blotting (Fig. S4.1c), NuPAGE LDS Sample Buffer (4X) was added to samples collected prior to the on-bead digestion. See Western blots section for further details.

LC-MS Analysis

Peptides were resuspended in 2% ACN with 0.1% TFA before loading onto a 25 cm x 75 µm ID, 1.6 µm C18 column (IonOpticks) maintained at 40°C. Peptides were separated with an

EASY-nLC 1200 system (Thermo Fisher Scientific, San Jose, CA) at a flow rate of 300 nl min⁻¹ using a binary buffer system of 0.1% FA (buffer A) and 80% acetonitrile with 0.1% FA (buffer B) in a two-step gradient. The following was performed for whole cell proteome samples, 3% to 27% B in 105 min and from 27% to 40% B in 15min. For lysosome-specific samples, 3% to 27% B in 52.5 min and from 27% to 40% B in 14.5 min. All samples were analyzed on a Fusion Lumos mass spectrometer (Thermo Fisher Scientific, San Jose, CA) equipped with a nanoFlex ESI source operated at 1550 volts, RF lens set to 30%, operated in data dependent acquisition mode with a duty cycle time of 1 sec. Full MS scans were acquired with a m/z scan range of 375-1500 m/z in the Orbitrap mass analyzer (FTMS) with a resolution of 240k for whole cell proteome and 120k for lysosome-specific samples. Selected precursor ions were subjected to fragmentation using higher-energy collisional dissociation (HCD) with a quadrupole isolation window of 0.7 m/z, and normalized collision energy of 31%. HCD fragments were analyzed in the Ion Trap mass analyzer (ITMS) set to Turbo scan rate. Fragmented ions were dynamically excluded from further selection for a period of 45 sec for whole cell proteome and 60 sec for lysosome-specific samples. The AGC target was set to 1,000,000 and 10,000 for full FTMS and ITMS scans, respectively. The maximum injection time was set to Auto for both full FTMS and ITMS scans.

Drug treatments

Vacuolin-1 (Milipore Sigma, cat. no. 673000), bafilomycin A1 (Milipore Sigma, cat. no. B1793), rapamycin (Milipore Sigma, cat. no. 553210), and PP242 (Milipore Sigma, cat. no. 475988) were resuspended per manufacturer's instructions, aliquoted, and stored at -80°C. All compounds were added to iAstrocytes alongside vehicle or ITC treatments (i.e. 24 hour treatments) with the exception of bafilomycin, which was added to cultures for the 2-4 hours preceding experiments for purposes of completely alkalinizing lysosomes.

Data analysis

Analysis of published RNA-seq datasets

We used BioJupies¹²⁵ to reanalyze bulk RNA-seq data and obtain differentially expressed genes from Perriot *et al.*¹⁰⁹ (GSE120411; hiPSC-derived astrocytes treated with IL1 β and TNF) and Barbar *et al.*¹⁰⁶ (syn21861229; CD49f+ astrocytes sorted from cerebral organoids treated with vehicle control or IL-1 α +TNF+C1q).

Proteomics

Raw files were searched against the human reference proteome (Swiss-Prot, downloaded on 20th of April 2020, refer to PRIDE upload for full sequence) along with the default common contaminants list with enzyme specificity set to trypsin within MaxQuant version 2.0.1.0 using standard settings with match between runs and the MaxLFQ algorithm activated. Whole cell proteome (raw data file names begin with 'Proteome') and lysosome-specific (raw data file names begin with 'LAMP1') raw files were set as separate parameter groups to ensure that the MaxLFQ algorithm was performed only within each sample set. The resulting proteinGroups text file was then uploaded to Perseus version 1.6.7.0 where all reverse sequences, potential contaminants and proteins only identified by site were filtered out of the dataset. All protein abundance values were normalized by Log 2 transformation. The lysosome-specific raw data files were evaluated separate from whole cell proteomic files. Search results from lysosomal raw data files were filtered to include proteins that were quantified in at least two out of three biological replicates within at least the ITC (raw data file names include ITC) or vehicle (raw data file names include WT) triplicate set. Missing values were then imputed within each replicate by replacing from the normal distribution using default settings. A two sample students t-test was performed between the ITC treated and vehicle triplicates, with permutation-based

FDR using default settings. The resulting T-test difference and significance were used to generate the lysosome-specific volcano plot.

Pathway enrichment analysis

We used Enrichr¹⁰⁰⁻¹⁰² to perform enrichment analysis of gene lists.

Flow cytometry

Data from flow cytometry experiments were analyzed using FlowJo (version 10.7.1). Live cells were gated by plotting SSC-A vs. FSC-A and then single cells were gated by plotting FSC-H vs. FSC-A. For experiments involving CRISPRi knockdown, analysis was restricted to sgRNA-transduced cells (gating on the histogram of BFP fluorescence values). For antibody staining experiments where median fluorescence intensity (MFI) values were reported, the average MFI of unstained control samples were subtracted from the MFI of stained samples. An example gating strategy from the resulting flow cytometry data is show in Supplemental Figure 1.

Fluorescence imaging analysis

We used CellProfiler (v3.15)¹⁰³ to quantify iAstrocyte immunostaining and neuron apoptosis (as measured by cleaved caspase 3/7 fluorescent dye) imaging data. For neuron viability, monochrome images of caspase 3/7 were thresholded (“Threshold” module, “Manual” setting) with respect to unstained (no caspase 3/7 dye) controls. The caspase 3/7 signal was then quantified as the total intensity for each image, using the thresholded image as a mask. Similarly, for iAstrocyte fluorescence microscopy images, the total image intensity of LAMP1, LAMP2, LC3, and LysoTracker signals were quantified after first thresholding images relative to either a no-primary antibody control (immunofluorescence—LAMP1, LAMP2, LC3) or no-dye control (LysoTracker). The total image intensity of LAMP1, LAMP2, and LC3 was then divided by the total intensity of Hoechst to correct for variation in cell number. All frames collected were

averaged to return a single quantification per well, which we considered as a single data point for statistical tests.

Statistics and reproducibility

Sample sizes were determined by referencing existing studies in the field. Major findings were validated using independent samples and orthogonal approaches. Numbers of replicates are listed in each figure. Randomization was not relevant to our study because no animals or human subjects were involved. Statistics were computed in RStudio (version 4.0.5). Correction for multiple testing was performed where appropriate.

REFERENCES

1. Phatnani, H. & Maniatis, T. Astrocytes in neurodegenerative disease. *Cold Spring Harb Perspect Biol* **7** (2015).
2. Escartin, C., *et al.* Reactive astrocyte nomenclature, definitions, and future directions. *Nature neuroscience* **24**, 312-325 (2021).
3. Liddelow, S.A., *et al.* Neurotoxic reactive astrocytes are induced by activated microglia. *Nature* **541**, 481-487 (2017).
4. Barbar, L., *et al.* CD49f Is a Novel Marker of Functional and Reactive Human iPSC-Derived Astrocytes. *Neuron* **107**, 436-453 e412 (2020).
5. Leng, K., *et al.* CRISPRi screens in human astrocytes elucidate regulators of distinct inflammatory reactive states. *bioRxiv* **2021.08.23.457400** (2021).
6. Zamanian, J.L., *et al.* Genomic analysis of reactive astrogliosis. *J Neurosci* **32**, 6391-6410 (2012).
7. Brambilla, R., *et al.* Inhibition of astroglial nuclear factor kappaB reduces inflammation and improves functional recovery after spinal cord injury. *J Exp Med* **202**, 145-156 (2005).
8. Perriot, S., *et al.* Human Induced Pluripotent Stem Cell-Derived Astrocytes Are Differentially Activated by Multiple Sclerosis-Associated Cytokines. *Stem cell reports* **11**, 1199-1210 (2018).
9. Chin, M.Y., *et al.* Genetically Encoded, pH-Sensitive mTFP1 Biosensor for Probing Lysosomal pH. *ACS Sens* **6**, 2168-2180 (2021).
10. Kaizuka, T., *et al.* An Autophagic Flux Probe that Releases an Internal Control. *Mol Cell* **64**, 835-849 (2016).
11. Abu-Remaileh, M., *et al.* Lysosomal metabolomics reveals V-ATPase- and mTOR-dependent regulation of amino acid efflux from lysosomes. *Science* **358**, 807-813 (2017).
12. Hasegawa, H., Thomas, H.J., Schooley, K. & Born, T.L. Native IL-32 is released from intestinal epithelial cells via a non-classical secretory pathway as a membrane-associated protein. *Cytokine* **53**, 74-83 (2011).
13. Andrews, N.W. Detection of Lysosomal Exocytosis by Surface Exposure of Lamp1 Luminal Epitopes. *Methods Mol Biol* **1594**, 205-211 (2017).
14. Rodriguez, A., Webster, P., Ortego, J. & Andrews, N.W. Lysosomes behave as Ca²⁺-regulated exocytic vesicles in fibroblasts and epithelial cells. *J Cell Biol* **137**, 93-104 (1997).
15. Wang, C., *et al.* Scalable Production of iPSC-Derived Human Neurons to Identify Tau-Lowering Compounds by High-Content Screening. *Stem cell reports* **9**, 1221-1233 (2017).

16. Sreetama, S.C., Takano, T., Nedergaard, M., Simon, S.M. & Jaiswal, J.K. Injured astrocytes are repaired by Synaptotagmin XI-regulated lysosome exocytosis. *Cell Death Differ* **23**, 596-607 (2016).
17. Verderio, C., *et al.* TI-VAMP/VAMP7 is the SNARE of secretory lysosomes contributing to ATP secretion from astrocytes. *Biol Cell* **104**, 213-228 (2012).
18. Horlbeck, M.A., *et al.* Compact and highly active next-generation libraries for CRISPR-mediated gene repression and activation. *Elife* **5** (2016).
19. Saxton, R.A. & Sabatini, D.M. mTOR Signaling in Growth, Metabolism, and Disease. *Cell* **169**, 361-371 (2017).
20. Sanmarco, L.M., *et al.* Gut-licensed IFN γ (+) NK cells drive LAMP1(+)TRAIL(+) anti-inflammatory astrocytes. *Nature* **590**, 473-479 (2021).
21. Granatiero, V., *et al.* Modulation of the IGF1R-MTOR pathway attenuates motor neuron toxicity of human ALS SOD1(G93A) astrocytes. *Autophagy*, 1-14 (2021).
22. Clark, I.C., *et al.* Barcoded viral tracing of single-cell interactions in central nervous system inflammation. *Science* **372** (2021).
23. Fan, Y. & He, J.J. HIV-1 Tat Promotes Lysosomal Exocytosis in Astrocytes and Contributes to Astrocyte-mediated Tat Neurotoxicity. *J Biol Chem* **291**, 22830-22840 (2016).
24. Miyaoka, Y., *et al.* Isolation of single-base genome-edited human iPS cells without antibiotic selection. *Nat Methods* **11**, 291-293 (2014).
25. Tian, R., *et al.* CRISPR Interference-Based Platform for Multimodal Genetic Screens in Human iPSC-Derived Neurons. *Neuron* **104**, 239-255 e212 (2019).
26. Gilbert, L.A., *et al.* Genome-Scale CRISPR-Mediated Control of Gene Repression and Activation. *Cell* **159**, 647-661 (2014).
27. Rappsilber, J., Mann, M. & Ishihama, Y. Protocol for micro-purification, enrichment, pre-fractionation and storage of peptides for proteomics using StageTips. *Nat Protoc* **2**, 1896-1906 (2007).
28. Torre, D., Lachmann, A. & Ma'ayan, A. BioJupies: Automated Generation of Interactive Notebooks for RNA-Seq Data Analysis in the Cloud. *Cell Syst* **7**, 556-561 e553 (2018).
29. Chen, E.Y., *et al.* Enrichr: interactive and collaborative HTML5 gene list enrichment analysis tool. *BMC Bioinformatics* **14**, 128 (2013).
30. Kuleshov, M.V., *et al.* Enrichr: a comprehensive gene set enrichment analysis web server 2016 update. *Nucleic Acids Res* **44**, W90-97 (2016).
31. Xie, Z., *et al.* Gene Set Knowledge Discovery with Enrichr. *Curr Protoc* **1**, e90 (2021).
32. McQuin, C., *et al.* CellProfiler 3.0: Next-generation image processing for biology. *PLoS Biol* **16**, e2005970 (2018).

33. Krencik, R. & Zhang, S.C. Directed differentiation of functional astroglial subtypes from human pluripotent stem cells. *Nat Protoc* **6**, 1710-1717 (2011).
34. Tyanova, S., Temu, T. & Cox, J. The MaxQuant computational platform for mass spectrometry-based shotgun proteomics. *Nat Protoc* **11**, 2301-2319 (2016).
35. Tyanova, S. & Cox, J. Perseus: A Bioinformatics Platform for Integrative Analysis of Proteomics Data in Cancer Research. *Methods Mol Biol* **1711**, 133-148 (2018).

Publishing Agreement

It is the policy of the University to encourage open access and broad distribution of all theses, dissertations, and manuscripts. The Graduate Division will facilitate the distribution of UCSF theses, dissertations, and manuscripts to the UCSF Library for open access and distribution. UCSF will make such theses, dissertations, and manuscripts accessible to the public and will take reasonable steps to preserve these works in perpetuity.

I hereby grant the non-exclusive, perpetual right to The Regents of the University of California to reproduce, publicly display, distribute, preserve, and publish copies of my thesis, dissertation, or manuscript in any form or media, now existing or later derived, including access online for teaching, research, and public service purposes.

DocuSigned by:

6C1694971C124DF... Author Signature

12/8/2021
Date